Probing Transition Metal Dichalcogenides via Strain-Tuned and Polarization-Resolved Optical Spectroscopy

Özgür Burak Aslan

Submitted in partial fulfillment of the
requirements for the degree of
Doctor of Philosophy
in the Graduate School of Arts and Sciences

COLUMBIA UNIVERSITY

2017

©2017
Özgür Burak Aslan
All rights reserved

ABSTRACT

Probing Transition Metal Dichalcogenides via Strain-Tuned and Polarization-Resolved Optical Spectroscopy

Özgür Burak Aslan

The strong light-matter interaction in the atomically thin transition metal dichalcogenides (TMDCs) has allowed the use of optical spectroscopy to investigate these materials in great depth. It has been shown that optoelectronic properties of ultrathin TMDCs are remarkably different from their bulk counterparts. Among them, this dissertation focuses on ultrathin $MoTe_2$ (molybdenum ditelluride) and ReS_2 (rhenium disulfide).

We first introduce the fundamental properties of the two material systems, $MoTe_2$ and ReS_2, investigated in this dissertation. Specific experimental methods for optical spectroscopy of 2D materials, 2D sample preparation, and related optics calculations are presented.

Absorption and photoluminescence measurements are applied to demonstrate that semiconducting $MoTe_2$, an indirect band gap bulk material, acquires a direct band gap in the monolayer limit. Furthermore, strain-tuned optical spectroscopy on $MoTe_2$ shows that tensile strain can significantly redshift its optical gap and partially suppress the intervalley exciton-phonon scattering. This suppression results in a narrowing of the near-band excitonic transitions. We also discuss the effect of strain on the transport properties of $MoTe_2$ due to this reduction in scattering.

We investigate monolayer ReS_2 as a TMDC system exhibiting strong in-plane anisotropy. These properties are explored by polarization-resolved spectroscopy. We show how the

accessible optical properties vary with optical polarization. We find that the near-band excitons in ultrathin ReS_2, absorb and emit light along specific polarizations. We also show that purely non-contact, optical techniques can determine the crystallographic orientation of ReS_2.

Table of Contents

List of Figures

Acknowledgements

First and foremost, I would like to thank my Creator, the Light of the heavens and the earth, for bringing me into existence and from darkness into the light. All the praise, knowledge, wisdom and copyrights belong to Him.

I am deeply grateful to my family for their continuous support and encouragement. They understood that I needed to be away from home. Their prayers have always kept me strong.

I would like to thank my advisor Tony F. Heinz for the opportunity to work in his lab, his mentorship, and for sharing his experience and knowledge with me. I worked with and learned from many people during my studies, and I want to acknowledge them. I would like to thank Claudia Ruppert, Alexey Chernikov, DeZheng Sun, Yilei Li, Albert Rigosi, Heather Hill, Suk Hyun Kim, James C. Hone, Marcos Pimenta, Arend van der Zande, Daniel Chenet, Young Duck Kim, Dongjea Seo, Pinshane Huang, Ali Dadgar, Geoffrey Iwata from Columbia University. Moreover, I would like to thank Eric Pop, Isha Datye, Eilam Yalon, Karen Lau, Elyse Barre whom I collaborated with after our labs moved to Stanford University. Special thanks go to Hiro Onodera, Dodd Gray, Chris Rogers, Leo Yu, Ouri Karni and Yasin Büyükalp for their optics support and many nice conversations we had around the kitchen table in the Spilker building.

A doctoral study is not just about research, and a good one takes the friendship of many. I am grateful to Fatih Kuşoğlu from İstanbul, and Erhan Acartürk, Cem Can Gümüş, Adeel Iqbal, Oybek Nazarov from New York for their support and warmth.

Dedicated to
my beautiful family who has always supported me
on my ongoing journey to
enlightenment

1. Atomically Thin $MoTe_2$ and ReS_2

1.1. From a Layered Bulk Material to Atomically Thin Layers

There is a crowded family of layered transition-metal dichalcogenides as shown in Figure 1-1. Ultrathin $MoTe_2$ (Molybdenum ditelluride) and ReS_2 (Rhenium disulfide), which are among the semiconducting ones, have recently attracted the interest of many researchers. Since this dissertation is going to build upon the foundations of the basic optical properties of TDMCs such as ultrathin $MoTe_2$, it will be essential to introduce their core properties and explain what makes them different from their relatively thicker counterparts.

Optical, electrical and structural properties of bulk $MoTe_2$ (thicker than ~10 nm) were extensively studied in the past.[1-12] Ultrathin crystals of graphene and other layered TMDCs materials were recently isolated and found to be stable.[13] However, the properties of ultrathin crystals of $MoTe_2$, having a relatively small band gap of 1 eV in the case of bulk as compared to similar TMDCs, remained unknown.[14] Its chemical stability under the ambient conditions, optical properties such as band gap, Raman spectra and how these would change with increasing thickness were not explored.

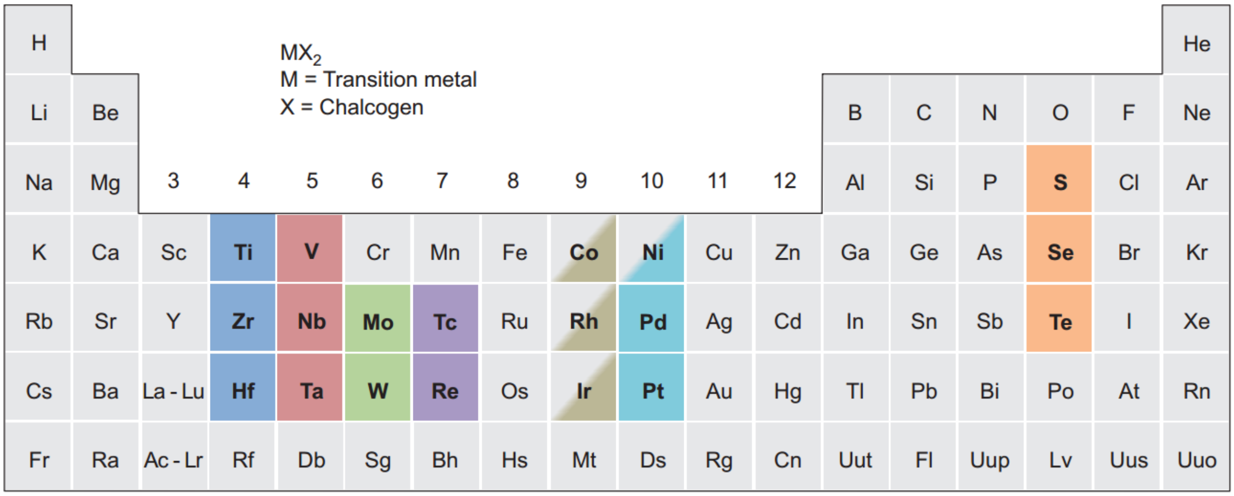

Figure 1-1: Periodic table highlighting the elements which form the TMDCs that predominantly crystallize in layered structures. Partial highlights for Co, Rh, Ir, and Ni indicate that only some of the dichalcogenides form layered structures.[15]

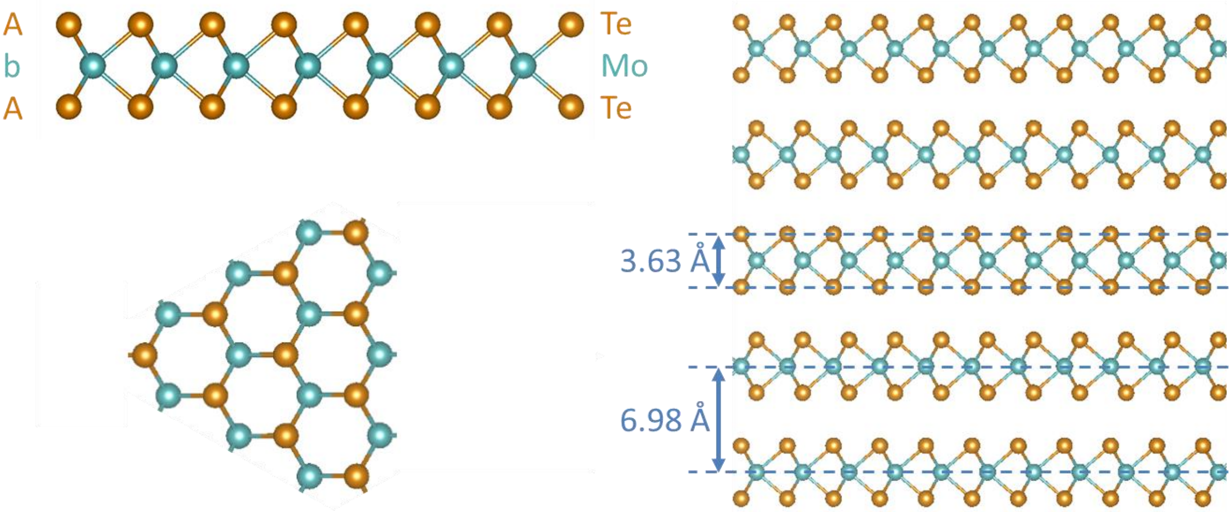

Figure 1-2: Crystal structure of $MoTe_2$. Diagrams at the top and bottom left correspond to section and c-axis views, respectively. Section view of the crystal structure of a five-layer $MoTe_2$ (Right). The letters “A b A” indicate the stacking sequence where the lower- and upper-case letters represent Mo and Te atoms, respectively. (Mo: cyan, Te: orange spheres). Left and right side of the figure have different scales.

Monolayer (1L) $MoTe_2$ is the building block of the bulk crystals. The representative crystal structure of a 1L is shown in Figure 1-2. A 1L is 6.98 Å thick and formed by only three atoms (Te-Mo-Te units). Crystals of odd, even layers and bulk $MoTe_2$ belong to the D_{3h}, D_{3d}, D_{6h} space groups, respectively. Despite the fact that a 1L is thinner than 1 nm, $MoTe_2$, as well as the other materials of the same family, has been predicted to have strong light-matter interaction due to the phenomenon called band nesting.[16-17] It has been proposed that the 1L crystals of $MoTe_2$ will have a direct gap as opposed to its bulk counterpart which has an indirect gap.[18] That direct gap has been expected to be at 1.1 eV which is very close to silicon's gap. Moreover, further studies predicted that tensile strain, W doping and electrical gating under ambient conditions could stabilize $MoTe_2$ in a metallic phase.[19-23] Because of the attractive properties mentioned above, $MoTe_2$ has attracted much attention, and there have been many studies on probing the band structure of 1L as well as the few-layer crystals (bilayer (2L), trilayer (3L) and so on) to confirm the predictions and to understand its properties further.

Figure 1-3a shows calculated band structures of bulk, 2L, and 1L $MoTe_2$. Multiple studies, including Chapter 4 of this dissertation, have demonstrated via absorption and photoluminescence (PL) spectroscopy that 1L $MoTe_2$ indeed acquires a direct band gap. Figure 1-3b shows that the PL peaks have a decrease in intensities and broadening in the spectral linewidths with increasing thickness from 1L to bulk. Those have been attributed to the emergence of an indirect transition at the 2L and have been supported by absorption measurements (Figure 1-3c and d, see also Chapters 2.1, 2.2 and 4). [24-27]

1.2. **Strain and Tungsten Alloying Effects on $MoTe_2$**

Due to the striking change in the nature of the band by only adding one more layer of the same material on top a 1L, researchers became interested in altering the band by other means such as in-plane tensile or compressive strain. Figure 1-4 plots the calculated band structure of 1L $MoTe_2$ under in-plane biaxial strain.[28] A strain of -2% (compressive) is expected to redshift the indirect valley (between K and Γ points) more than the direct valley (K-point) with respect to the maximum of the valence band (K-point) such that the 1L attains an indirect gap. On the contrary, a strain of +2% (tensile) makes the 1L “more direct” meaning the indirect valley goes even higher in energy with respect to the direct valley. Chapter 5 will show the optical signatures of such a modification by tensile strain, specifically on the spectral linewidths of the optical transitions. Chapter A.5 will present how to realize and quantify the strain.

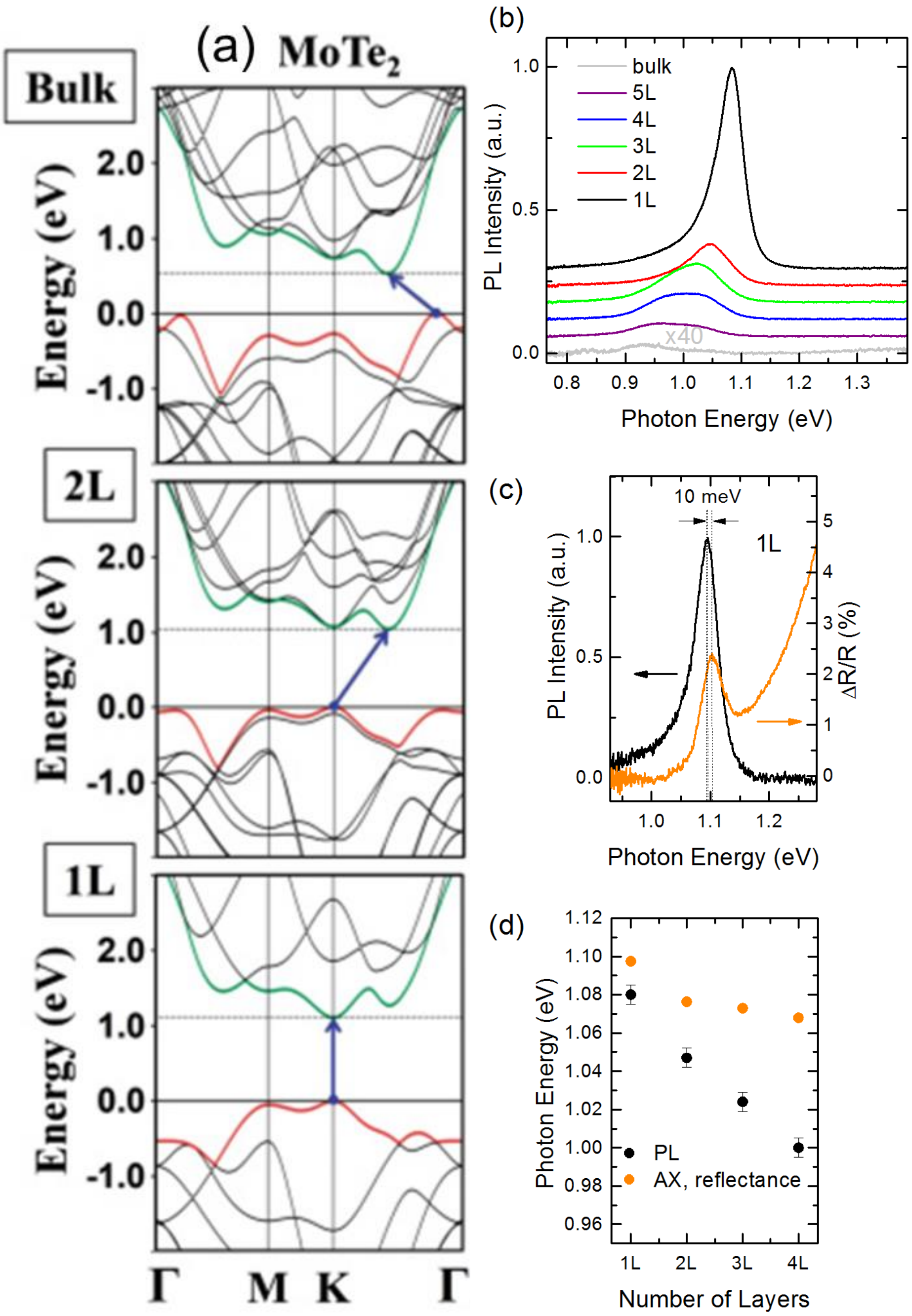

Figure 1-3: (a) Calculated band structure of MoTe$_2$ for bulk, 2L,1L crystals. The solid blue arrows indicate the lowest energy transitions. From the calculations, 1L was expected to acquire a direct gap at the K point of the Brillouin zone as opposed to bulk which has an indirect gap. (b) PL spectra of 1L-5L and bulk, (c) PL and reflection contrast spectra of 1L, (d) comparison of the peak positions of reflection contrast in 1L-4L (AX: A exciton) and PL.[18]

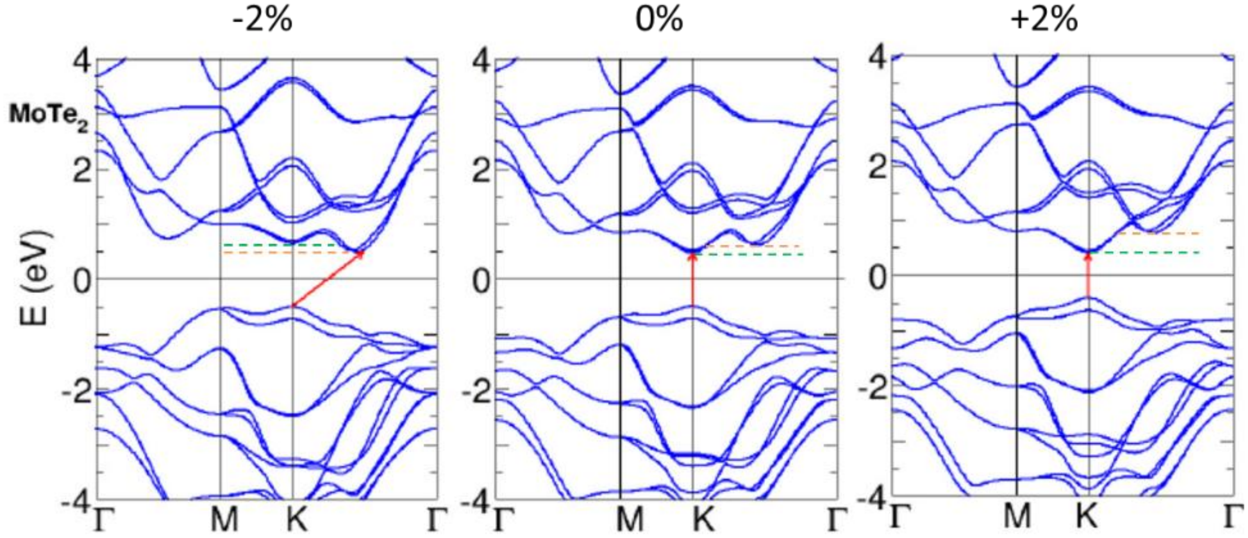

Figure 1-4: Calculated band structure of 1L $MoTe_2$ for different lattice strains: -2, 0, and +2% in-plane biaxial strain with respect to the experimental lattice constant. The red arrows indicate the lowest energy transitions. Green and orange dashed lines indicate the minimum point of the direct and indirect valleys in the valence band.[28]

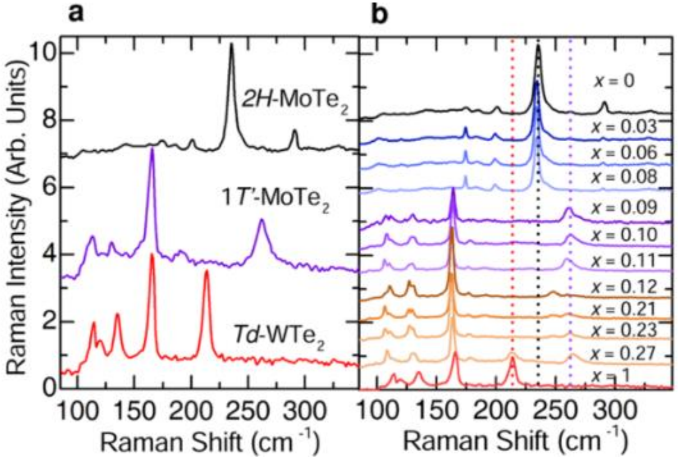

Figure 1-5: Raman spectra of bulk (a) 2H-$MoTe_2$, 1T′-$MoTe_2$, γ-WTe_2 (b) $Mo_{1-x}W_xTe_2$ for several values of x. Notice the change in the spectrum observed for x ≥ 0.09, indicating a structural phase transition as a function of doping. [22]

WTe_2 is another layered TMDC which stabilizes in a 1T′ (distorted octahedral) structure and is metallic, as opposed to the 2H (trigonal prismatic) and semiconducting phase of $MoTe_2$. Recent studies inspired by WTe_2 have shown via Raman spectroscopy (as well as by other means) that the alloyed compounds of $MoWTe_2$ can also be stabilized in a 1T′ phase with a certain proportion of W.[22,29] Figure 1-5 contains Raman spectra of alloyed crystals of $MoWTe_2$

with varying W/Mo content. The spectra show that the crystal does no longer remain in the semiconducting 2H phase if W content is higher than a certain amount. The spectrum abruptly changes since a different crystal structure will result in different vibrational modes and thus, different frequencies.

Chapter 5 will present the optical properties of a $MoWTe_2$ alloy with W: Mo ratio of about 1:9 which is still in the semiconducting 2H phase. We will compare the optical properties of $MoTe_2$ and $MoWTe_2$. Strain-tuned optical measurements will shed more light on their band structures. Along with W alloying, other studies have predicted that the $MoTe_2$'s phase can switch with high tensile strain. This dissertation will not cover the effects of such strain levels on $MoTe_2$.[19]

1.3. Anisotropy with Three Atoms: Monolayer ReS_2

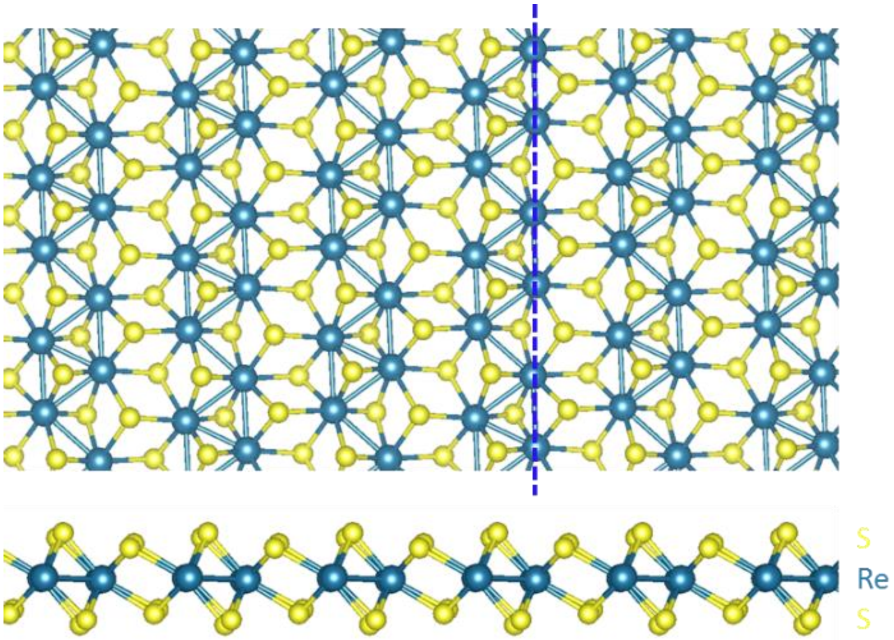

Figure 1-6: Diagram of the crystal structure of 1L ReS_2. Top view (top) and the view along the blue dashed line (bottom).

Anisotropic optical properties are present in bulk crystals of sufficiently low symmetry. In layered materials, in-plane anisotropy can be significant, as in the case of black phosphorus.[30-33] The group-VI transition metal dichalcogenides such as MoS_2, $MoSe_2$, WS_2, WSe_2, and $MoTe_2$ are also layered materials with distinctive optical properties.[15,34] Their 1Ls provide, for example, valley selective excitation of band-edge excitons using circularly polarized light as a consequence of their broken inversion symmetry.[35-38] However, because of the high symmetry of the crystal structure, their linear optical properties of absorption and emission are isotropic in the plane of the layer.

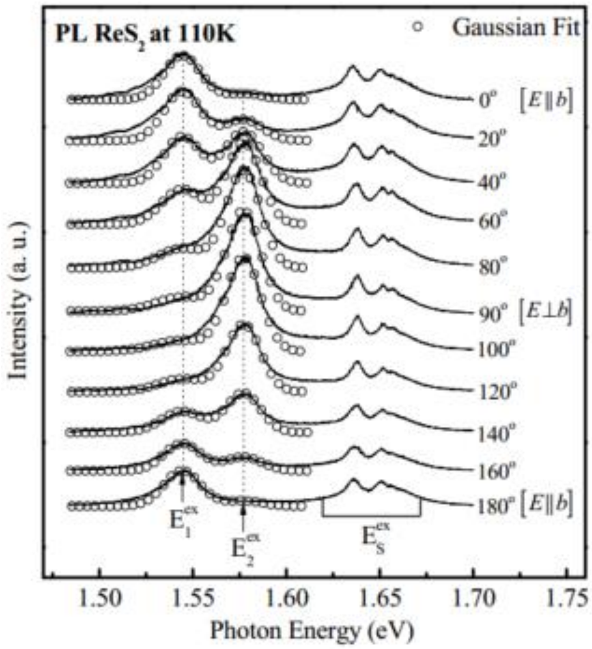

Figure 1-7: The polarization-resolved PL spectra of ReS$_2$ taken at 110 K in the angle range between 0° and 180° with respect to *b*-axis (represented by the blue dashed line in Figure 1-6).[39]

ReS$_2$, a layered group-VII transition metal dichalcogenide, possesses reduced crystal symmetry compared to the molybdenum and tungsten dichalcogenides. Figure 1-6 shows a diagram of the crystal structure of 1L ReS$_2$ (compare to Figure 1-2). This reduced symmetry gives rise to anisotropic in-plane optical properties. ReS$_2$, thus, merits special attention. Figure 1-7 plots polarization-resolved PL spectra of bulk ReS$_2$ which demonstrates the anisotropy of emission by near-band transitions. Intensities of the emission by the two transitions labeled as E^{ex}_1, E^{ex}_2 (excitons 1 and 2) seem to strongly depend on collection polarization. While the anisotropic optical and electric properties of bulk ReS$_2$ crystals and the basic optical properties of ultrathin layers were previously studied,[39-45] anisotropic optical effects in ultrathin layers of ReS$_2$ were unexplored. Theoretical predictions claimed that 1L ReS$_2$ would still demonstrate anisotropic absorption. Figure 1-8 contains calculated absorption spectra of 1L ReS$_2$ for the incident light polarized along different in-plane directions.[46] However, it was not experimentally verified whether ultrathin layers could still possess strong anisotropy in optical properties such as absorption and PL, which was proposed by the calculations.

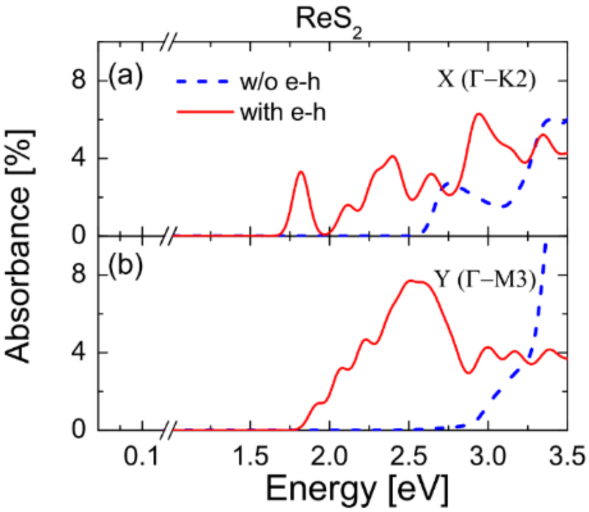

Figure 1-8: Calculated optical absorption spectra of 1L ReS_2 for the incident light polarized along different in-plane directions.[46]

Chapter 6 will demonstrate that the anisotropy is maintained in the ultrathin layers down to 1L. Specifically, Chapter 6.1 will present results on polarization-resolved absorption and PL, Chapter 0 on Raman scattering. Moreover, those results will be related to the crystallographic orientation of the ultrathin layers.

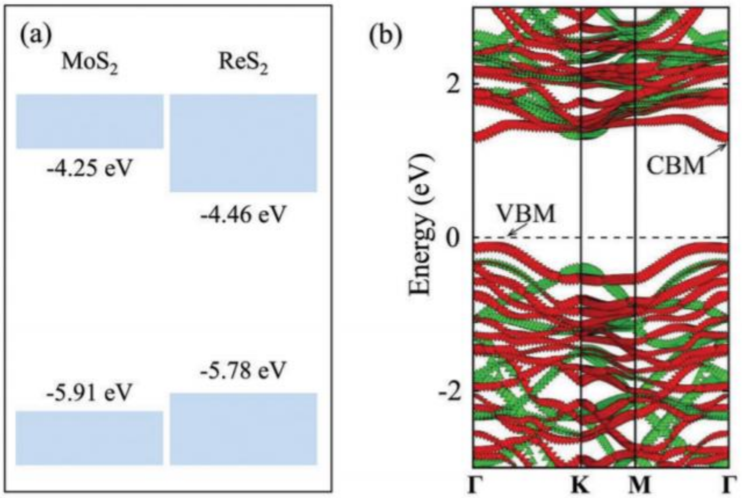

Figure 1-9: (a) Schematic of the band alignment between 1Ls of MoS_2 and ReS_2. (b) Calculated band structure for the MoS_2-ReS_2 heterostructure (MoS_2 and ReS_2 states are red and green, respectively).[47]

Findings of this work has sparked interest in ReS_2 research such as studies on electroluminescence, third harmonic generation, heterostructures with other TMDCs (see Figure 1-9), optical Stark effect (see Figure 1-10), strain engineering.[47-50]

Sim et al. have recently made a novel observation in ReS_2, which is energy-selective optical Stark effect in few-layer ReS_2.[51] They have measured differential transmission (ΔT/T) while varying pump-probe polarization configuration. By separately aligning the probe polarization parallel to the maximum absorption angle by the two lowest energy excitons (X1 and X2), they have performed pump-probe measurements with the pump co- and cross-polarized with the probe polarization. Interestingly, they have observed that the co-linearly polarized pump-probe pulses cause an absorption derivative-like ΔT/T response (middle panel of Figure 1-10) only at the spectral region dominated by the exciton along which the absorption is maximized (X1 or X2). The amplitude of the Stark signal becomes small when the pump is orthogonally polarized to the probe (bottom panel of Figure 1-10). As they have discussed, Chapter 6.1 will show that this energy and polarization selectivity can be explained by the anisotropic optical absorption of the excitons. They also note that this rare phenomenon is absent in other materials, such as semiconductor quantum wells, carbon nanotubes, and group VI TMDs.

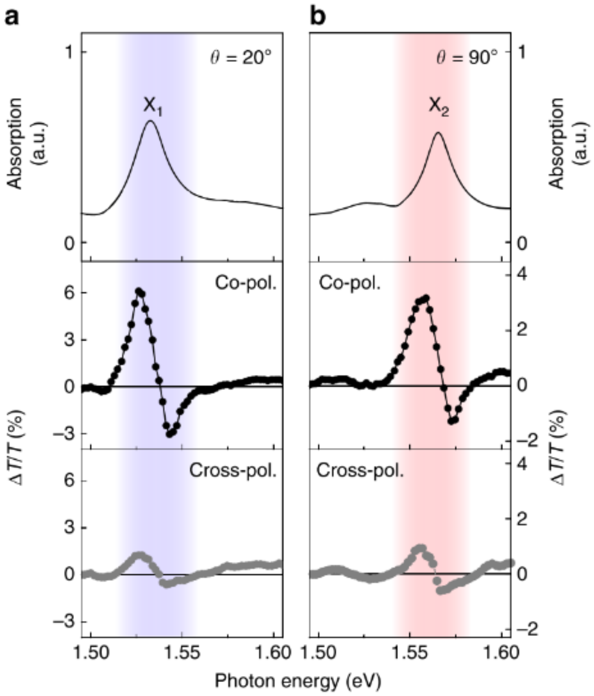

Figure 1-10: Exciton-selective optical Stark effect controlled by light polarization. (a,b) Equilibrium absorption spectra with the light polarization angle of 20° (top panel in a) and 90° (top panel in b). Black dots (middle panels) and gray dots (bottom panels) are transient ΔT/T spectra at t=0 fs with co-polarized and cross-polarized pump-probe configurations, respectively. Probe polarization angles are fixed at 20° (a) and 90° (b). Pump photon energy is 1.44 eV. The blue- (red-)shaded area represents the spectral region where ΔT/T signal is dominated by the shift of the X1 (X2) state. X1 and X2 are near-band-edge excitonic transitions.[51]

2. Experimental Methods

2.1. Reflection Contrast or Absorption Spectroscopy

Optical absorption (absorption, $\mathcal{A}$) spectroscopy tells a lot about the optical as well as electronic properties of transition metal dichalcogenides (TMDCs). The ideal way of obtaining the absorption of a material is to perform optical reflection and transmission measurements to make use of the following relation:

$$\mathcal{A}(\lambda) = 1 - Reflection(\lambda) - Transmission(\lambda) \tag{1}$$

where "(λ)" denotes the wavelength dependence. Regarding the ultrathin materials of interest, TMDCs, there is an easier way to obtain their absorption spectrum. That is to measure their reflection (or reflectance) contrast; meaning how much more (or less) do they reflect as compared to a known reflector.

In reflection contrast measurements, we record the differential reflectance of the sample normalized by the reflectance of a semi-infinite and transparent substrate, i.e.,

$$\frac{\Delta R}{R} = \frac{R_{\mathrm{sample}+substrate} - R_{substrate}}{R_{substrate} - R_{bg}} \tag{2}$$

where $R_{\mathrm{sample}+substrate}$, $R_{substrate}$, and R_{bg} represent, respectively, the reflectance of the thin sample on the substrate, of the bare substrate and without any substrate or sample. R_{bg} can be practically measured by focusing the objective significantly above the sample such that no light reflected by the sample will be collected (recall that the light incident on the back of the objective is a parallel beam). For sufficiently small values of the reflection contrast for a sample on a thick transparent substrate we can determine the absorbance $\mathcal{A}$ of an unsupported ultrathin TMDC crystal from $\Delta R/R$ as $\mathcal{A} = \frac{1}{4}(n_{substrate}^2 - 1)(\frac{\Delta R}{R})$, [52-54] where $n_{substrate}$ denotes the refractive index of the substrate. We can thus probe the absorption spectra of sufficiently thin samples through measurements of the reflection contrast. This and a more general, and better approximation of the relation between the reflection contrast and absorbance will be derived shortly.

Having the same focus on and off the sample is crucial. Reasons for an unstable focus may include airflow in the room, a sample or slide that is not fixed well by a piece of tape, a flexible substrate that is strained and is relaxing or stabilizing very slowly.

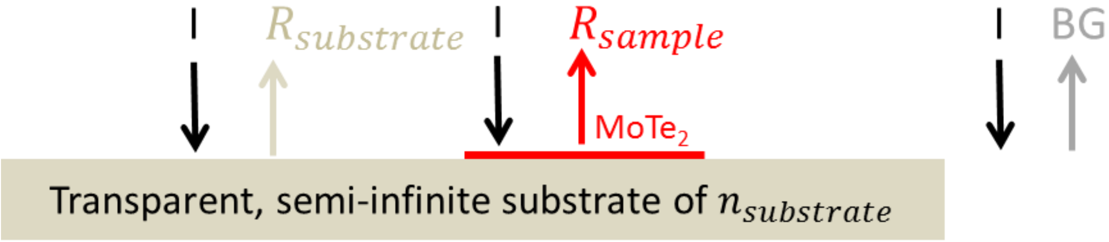

Figure 2-1: How the reflection contrast measurements work.

$$\frac{\Delta R}{R}(\lambda) = \frac{R_{sample} - R_{substrate}}{R_{substrate}}(\lambda) \cong \frac{4}{n(\lambda)^2 - 1} Abs(\lambda) \qquad (3)$$

We assume μ=1 (magnetic permeability) for all materials and non-absorbing (real refractive index) top and bottom media.

$$\sigma^S \stackrel{\text{def}}{=} \frac{\sigma_{sheet}}{\varepsilon_0 c}, \qquad \sigma_{sheet} = thickness \times \sigma_{conductivity}\ (sheet\ conductivity) \qquad (4)$$

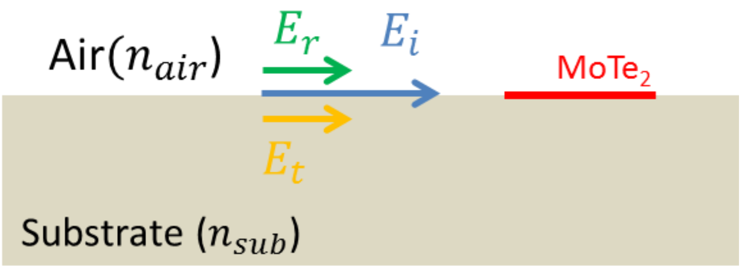

Figure 2-2: Diagram depicting the electric fields on an interface with/without ultrathin MoTe$_2$

At normal incidence without the 2D material (thickness of which is much smaller than the wavelength of the incident light), the incident, E_i, reflected, E_r, and transmitted, E_t, electric fields are related by

$$E_i + E_r = E_t \text{ with } E_r = r \times E_i \text{ and } r = \frac{n_{air} - n_{sub}}{n_{air} + n_{sub}} \tag{5}$$

n_{air} and n_{sub} are the refractive indices of the top and substrate medium, respectively. If the field is incident on 2D MoTe$_2$, there will be a surface current, $j_{surface}$, induced by the electric field on the surface and can be calculated by

$$j_{surface} = E_t \times \sigma^s = (E_i + E_r) \times \sigma^s \tag{6}$$

Therefore, the continuity equation for the magnetic fields on the surface becomes

$$H_i - H_r = H_t + j_{surface} \tag{7}$$

Where H_i, H_r, and H_t are the magnetic fields that are incident, reflected and transmitted on the interface, respectively.

Replacing H with $E \times \frac{n}{c}$ where n is the refractive index of the corresponding medium and substituting $j_{surface}$ into Eq. (7) yields

$$\begin{gathered} n_{air}E_i - n_{air}E_r = n_{sub}E_t + j_{surface} = n_{sub}E_i + n_{sub}E_r + E_i \times \sigma^s + E_r \times \sigma^s \\ E_i(n_{air} - n_{sub} - \sigma^s) = E_r(n_{air} + n_{sub} + \sigma^s) \end{gathered} \tag{8}$$

$$r = \frac{E_r}{E_i} = \frac{n_{air} - n_{sub} - \sigma^s}{n_{air} + n_{sub} + \sigma^s} \text{ and } t = \frac{E_t}{E_i} = \frac{2n_{air}}{n_{air} + n_{sub} + \sigma^s} \tag{9}$$

Therefore, the reflection, transmission and absorption coefficients become

$$\begin{aligned} R(n_{air}, \sigma^s, n_{sub}) &= \left|\frac{n_{air} - n_{sub} - \sigma^s}{n_{air} + n_{sub} + \sigma^s}\right|^2 \\ T(n_{air}, \sigma^s, n_{sub}) &= \frac{4n_{sub}}{|n_{air} + n_{sub} + \sigma^s|^2} \\ A(n_{air}, \sigma^s, n_{sub}) &= 1 - R - T = \frac{4n_{air}\mathrm{Re}[\sigma^s]}{|n_{air} + n_{sub} + \sigma^s|^2} \end{aligned} \tag{10}$$

If $|\sigma^s| \ll 1$, ignoring 2nd order terms in σ^s to approximate the reflection and transmission contrasts by

$$\begin{aligned} \frac{\Delta R}{R} &= \frac{R_{sample+substrate} - R_{substrate}}{R_{substrate}} = \frac{R(n_{air}, \sigma^s, n_{sub}) - R(n_{air}, 0, n_{sub})}{R(n_{air}, 0, n_{sub})} \\ &\cong \frac{4n_{air}\mathrm{Re}[\sigma^s]}{{n_{sub}}^2 - 1} \\ \frac{\Delta T}{T} &\cong -\frac{2\mathrm{Re}[\sigma^s]}{n_{air} + n_{sub}} \end{aligned} \tag{11}$$

From Eq. (10) the absorbance of a free-standing 2D sample (air on both sides) is

$$A_{free-standing} = A(1, \sigma^s, 1) = \frac{4\mathrm{Re}[\sigma^s]}{|2 + \sigma^s|^2} \cong \mathrm{Re}[\sigma^s] \tag{12}$$

Therefore, we obtain the following relations:

$$\begin{aligned} \frac{\Delta R}{R}(n_{air}, \sigma^s, n_{sub}) &\cong \frac{4n_{air}}{{n_{sub}}^2 - 1} A_{free-standing} \\ \frac{\Delta T}{T}(n_{air}, \sigma^s, n_{sub}) &\cong -\frac{2}{n_{air} + n_{sub}} A_{free-standing} \end{aligned} \tag{13}$$

If we further ignore Im$[\sigma^s]$ since it only contributes in 2nd and higher order in σ^s since n_{air}, n_{sub} are real, we obtain σ^s from Eq. (10) (for $n_{sub} + \sigma^s > n_{air}$)

$$\sigma^s \cong n_{air} \frac{1 + \sqrt{R(n_{air}, \sigma^s, n_{sub})}}{1 - \sqrt{R(n_{air}, \sigma^s, n_{sub})}} - n_{sub} \tag{14}$$

Finally, since the reflection contrast is a commonly measured experimental quantity, the reflection term can be expressed in the form of the reflection coefficient of two semi-infinite media and reflection contrast as

$$R(n_{air}, \sigma^s, n_{sub}) = R(n_{air}, 0, n_{sub}) \sqrt{1 + \frac{\Delta R}{R}} \tag{15}$$

We will see a basic use of the reflection contrast technique in Chapter 3 which presents temperature dependent absorption spectroscopy of 1L MoS_2.

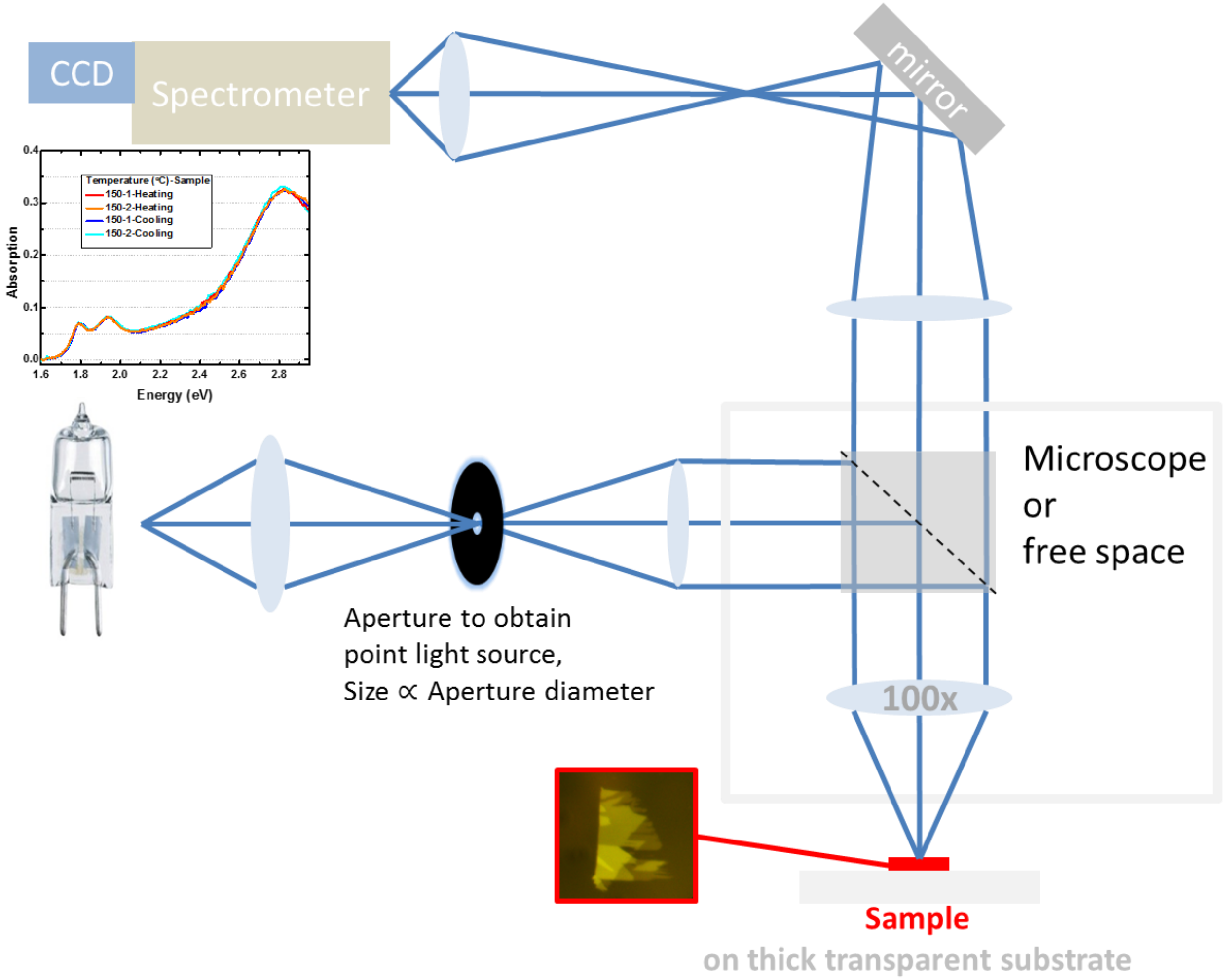

Figure 2-3: Diagram of a typical reflection contrast setup.

Figure 2-3 shows the diagram of a typical optical setup to perform reflection contrast spectroscopy. We focus a broadband light emitter such as a tungsten halogen source onto an aperture (diameter might vary from about 25 to 150 μm) to obtain a point light source. Converging lenses collimate and refocus the point light source onto a sample, and the reflected light can be separately collected with a beam splitter. A monochromator disperses the reflected light onto a detector.

2.1.1. Polarization-Resolved Reflection Contrast

Polarization-resolved reflection contrast technique should be used on ultrathin materials refractive indices of which are anisotropic with respect to the out-of-plane axis. Their effective refractive index will depend on the polarization of the incident light. For a given polarization, reflections from the sample and substrate are measured, and the absorption can be calculated as discussed in Chapter 2.1. Since the calculations involve a division by the substrate reflection, it eliminates any anisotropy in the collection efficiency (assuming that neither the sample nor the setup significantly rotates the polarization of the light). In polarization-resolved measurements, a strain-free objective should be used to ensure that we illuminate the sample with linearly polarized light and detect the reflected light of the same polarization.

2.2. Photoluminescence Spectroscopy

Photoluminescence (PL) is the emission of light by a material after the absorption of a photon (still light). An alternative process would be electroluminescence in which electricity (electric field) causes the emission of light. Semiconductors have a gap between the conduction and valence bands (CB and VB) and an electron excited to CB from VB by the absorption of light will scatter down to the bottom of the CB and will stay there for a while (see Figure 1-3). It is energetically favorable to go back down to VB which can be mediated by various processes. One such process is the emission of a photon with the energy that is equal to the difference between the initial and final points of the electron in the Brillouin Zone (note that this energy is not necessarily the same as that of the absorbed photon).

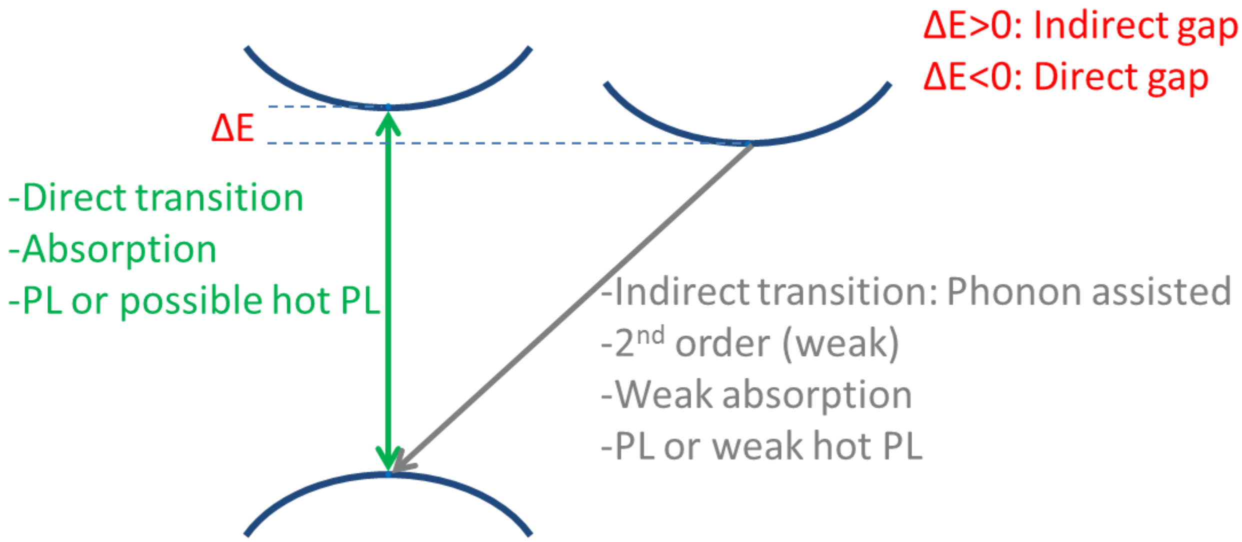

Figure 2-4: Diagram of the band structure of a typical semiconductor near its band gap. Possible smallest energy transitions of PL and absorption are indicated by arrows, the tip of which pinpoints to the final state of the transition. Absorption and PL measurements can distinguish direct and indirect transitions from each other.

A semiconductor may have a direct or indirect gap. Figure 2-4 shows a diagram of a typical band structure near the band gap of a semiconductor. Phonons do not assist direct transitions, and absorption and PL by such transitions can be strong. However, indirect transitions require phonon assistance and absorption and PL by such transitions become very weak. If the energy separation between the bottom of the direct and indirect valleys, ΔE, is positive (indirect gap) but not much larger than $k_b \times T$, where k_b is Boltzmann constant and T is the temperature of the system, hot PL from the direct transition can still be observed. Moreover, PL, but not absorption, by the indirect transition can still be detected. Indirect PL is still detectable because the electrons excited to the CB will quickly scatter down to the bottom indirect valley and will populate there. If ΔE is negative (direct gap), we expect to observe absorption and PL only from the direct transition. Therefore, absorption and PL measurements are great ways of distinguishing between direct and indirect transitions and telling whether the semiconductor has a direct or indirect band gap.

2.2.1. Polarization-Resolved Photoluminescence

If an ultrathin material has low symmetry such that it emits PL with varying intensity with respect to the rotations around the out-of-plane axis, the PL should be measured with more care to discern the properties of the material more accurately. One way is to rotate the material for a fixed collection and illumination geometry and record the PL. Maintaining the same collection geometry will make sure that the setup does not alter the emitted PL. The illumination may be a non-resonant and linearly polarized laser excitation (i.e. far from the PL peak) such that the varying absorption for different material orientations can be normalized (see 0Chapter 2.1.1). The excited electrons will scatter down non-resonantly to the minima of the CB and PL may occur from multiple initial states there.

2.2.2. Time-Resolved Photoluminescence

Time-Resolved PL (TRPL) measurements tell us how long it takes for the material to emit photons after they absorb the incident photons. TRPL experiments are very informative about the optical transitions as the time required to emit a photon is a characteristic feature of the specific transition. That way one can distinguish the type of the transitions even if they are close in energy and probe many fundamentals properties of matter.

2.3. Strain-Optics Experiments

Magnetic and electric fields are very common to employ for tuning the optoelectronic properties of semiconductors. Strain can also tune the band structure of materials, and that change can be optically measured. An ultrathin flake on a few hundred microns thick flexible substrate can be strained using 2-, 3-, or 4-point bending methods. There will be a tensile strain on one surface and compressive strain on the other. Strain-dependent reflection contrast, PL, and other optical measurements can be very informative, and Chapter 5 will illustrate an example on the atomically thin $MoTe_2$.

3. Optical Absorption of 1L MoS_2 at Elevated Temperatures for Raman Thermometry

This chapter will give an example use of the reflection contrast (or absorption) spectroscopy to study 1L MoS_2.

The ability to measure the temperature and study the thermal properties of ultrathin microscopic devices, such as TMDCs, is highly desirable to engineer their heat dissipation to the environment.[55-57] Many optical properties change with temperature; thus, optical spectroscopy can help estimate the temperatures of such devices. Raman thermometry is one of the methods; it is non-contact and can measure the temperature with a lateral resolution of ~500 nm (limited by laser spot size). A device/material of interest can be elevated to known temperatures, and the frequencies of the Raman-active modes can be noted (Raman spectroscopy needs to be performed with low power to avoid heating further).[57] These frequencies give us a calibration of Raman-active modes and temperature. This calibration can then be used to calculate the temperature via Raman spectroscopy during electrical or optical heating. Furthermore, if heating with a laser, Raman can be simultaneously performed. Thus, temperature and the power absorbed can be extracted to characterize the thermal properties of the sample. However, to accurately define the optical input power, we need to know the optical absorption by the sample. Since the sample is (optically) heated, we must account for its temperature dependent absorption. To this end, we have measured the temperature-dependent absorption of CVD-grown 1L MoS_2 as reported below.

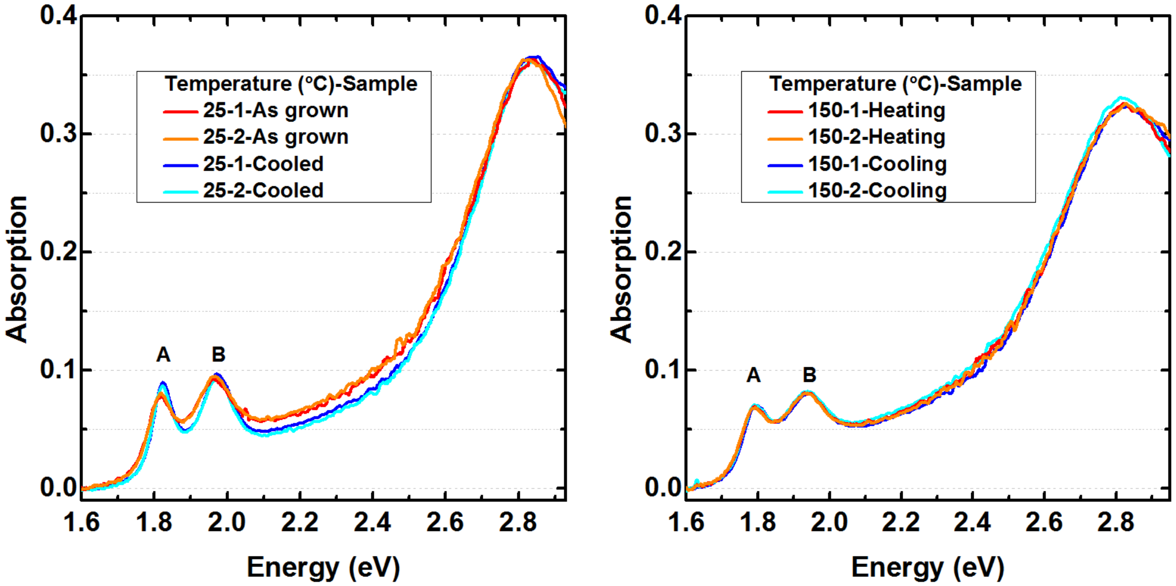

Figure 3-1: Absorption measurements on 1L MoS_2 for Raman thermometry. Before and after heating at room temperature (Left) and 150 °C (Right). We have measured the absorption of CVD grown 1L MoS_2 on quartz substrates at temperatures from 25 °C up to 300 °C and down to 25 °C in a Linkam stage THMS600. We have studied two specific flakes for all temperatures. We have observed that, due to the release of the well-known built-in strain on the as-grown samples, the A and B excitons have slightly blue-shifted after the heating-cooling procedure as shown in Figure 3-1. We also note that the A and B excitons become slightly narrower after cooling. We attribute this narrowing to the removal of surface adsorbates which cause inhomogeneity and act as scattering channels for the excitons.[58] This hysteresis (blue-shift) has not appeared at the temperatures of 150 °C and above suggesting the release of the strain. We show measurements performed at 150 °C during the heating and cooling cycles in Figure 3-1.

We select and plot four strain-free spectra in Figure 3-2. It is clearly seen that the absorption changes significantly nearby the A and B excitons. We extract how much the 1L

MoS_2 absorbs by averaging over the two samples measured at commonly used laser wavelengths of 488, 515, 532, 633 nm and fit them to the lines as shown in Figure 3-2. It is evident that in green lasers, for instance, the absorption at 250°C is increased by ~30% compared with its room temperature value. Overlooking this ~30% increase in the absorbed power can result in underestimation of the thermal boundary conductance and thermal conductivity of a 2D material in Raman thermometry experiment by a factor of ~2. The values of temperature-dependent absorption should be useful for calculating how much laser power the 1L MoS_2 will absorb for Raman thermometry and for other optoelectronic applications where the samples need to perform at elevated temperatures.

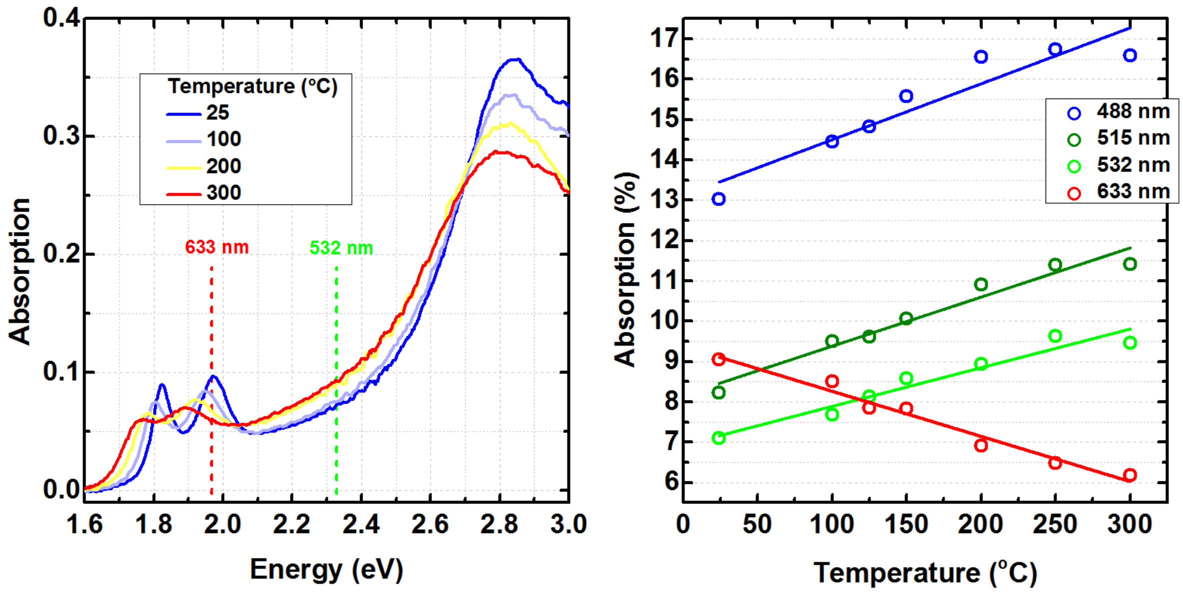

Figure 3-2: Temperature dependent absorption on 1L MoS_2 from 25 to 300 °C (Left) and absorption values and linear fits at commonly used laser wavelengths (Right).

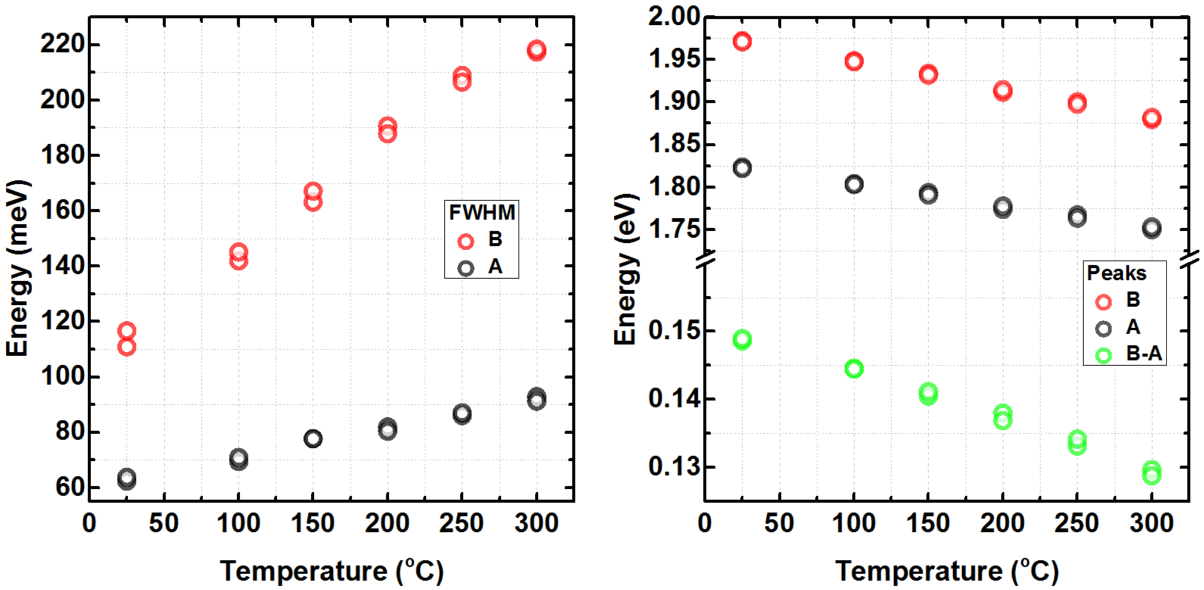

Figure 3-3: Peak positions and FWHM of A and B excitons at elevated temperatures.

We also fit the (strain-free) spectra to Lorentzian line shapes and extract the peak and FWHM of the A and B excitons, as shown in Figure 3-3. Note that there is one data point for each of the two samples at each temperature. We observe that the FWHM increases with temperature for both A and B excitons mainly due to the growing number of phonons which increase the exciton-phonon scattering rate. A and B excitons both redshift from about 1.82 and 1.97 eV to about 1.75 and 1.88 eV, respectively. Such redshifts, as the temperature increases, are common in solid state physics and because orbitals that form the bands will usually overlap less in an expanded crystal. Another interesting observation is that the B-A exciton separation decreases from about 150 to 130 meV. Spin-orbit coupling and any difference in their excitonic binding energy will contribute to this separation. We hope that our results will shed more light on the 1L MoS_2 band structure and future studies can build upon the findings here.

4. Optical Properties and Band Gap of Single- and Few-Layer $MoTe_2$ Crystals

Single- and few-layer crystals of exfoliated $MoTe_2$ have been characterized spectroscopically by PL, Raman scattering, and optical absorption measurements. We find that $MoTe_2$ in the 1L limit displays strong PL. Based on complementary optical absorption results, we conclude that 1L $MoTe_2$ is a direct-gap semiconductor, with an optical band gap of 1.10 eV. This new 1L material extends the spectral range of atomically thin direct-gap materials from the visible to the near-infrared.

4.1. Introduction

Atomically thin two-dimensional crystals have attracted much recent attention due to their distinctive properties.[13,15,34] 1Ls of group-VI transition metal dichalcogenides (TMDCs) are of particular interest as a family of ultrathin semiconductors. Crystals of MoS_2, $MoSe_2$, and their tungsten analogs have been shown to transform from indirect to direct-gap semiconductors in the 1L limit.[59-61] These materials have, moreover, shown their suitability for access to the valley degree of freedom through excitation by circularly polarized light.[62]

The availability of a wide range of band gaps is important both for fundamental research and applications. For the TMDC family, the direct gap varies with the choice of chalcogen atom, with 1Llayer MoS_2 and $MoSe_2$ having, for example, gaps of 1.85eV[59-60] and 1.55eV[63-64], respectively. The optical gap can be tuned continuously between the limits of the stoichiometric crystals using alloys with different chalcogen concentrations.[65-68] Modification of the band gap of 1L TMDCs is also possible by applying strain and has yielded shifts around 60 meV.[69-71]. The design of heterostructures of different TMDCs allows for further tailoring the band structure[72-73] and may reveal fundamentally new effects related to interlayer coupling. Nevertheless, a material with a band gap close to 1 eV has not yet been identified and would be valuable both as a new 2D system and as a building block for more complex structures.

4.2. Results and Discussion

Bulk $MoTe_2$ (α-$MoTe_2$) is a semiconductor with an indirect band gap of about 1.0 eV.[74-75] It is composed of hexagonal sheets of Mo atoms that are sandwiched between two hexagonal planes of Te atoms, with trigonal prismatic coordination [Figure 4-1(a)]. These Te-Mo-Te units, which we refer to as 1Ls, are held together by weak van der Waals forces and are stacked with 2H symmetry (Figure 4-1a). 1L and few-layers of $MoTe_2$ are promising candidate systems to exhibit narrow band gaps. They have a characteristic thickness-dependent Raman spectrum[76] and have been predicted to exhibit a phonon-limited room-temperature mobility greater than that of MoS_2.[77] Transistor devices employing few-layer $MoTe_2$ crystals have recently been demonstrated.[78-79] In this article, we present experimental results on the optical properties of mechanically exfoliated mono- and few-layer $MoTe_2$. Using Raman scattering, atomic force microscopy, and optical contrast, we identify crystals of 1-5 monolayer thickness. PL and optical absorption measurements are applied to locate the optical gap and to analyze the spectral signatures related to the direct or indirect character of the transition. In the 1L limit, we find that the material becomes a direct gap semiconductor, with an optical gap of 1.10 eV. $MoTe_2$ thus constitutes a new direct-gap 1L material with a significantly lower gap than available heretofore.

We prepared our ultrathin layers by mechanical exfoliation of synthetic semiconducting $MoTe_2$ crystals. The layers were deposited on either bulk *z*-cut quartz substrates (SiO_2) or silicon wafers with a 300-nm thick overlayer of thermal oxide (SiO_2/Si). We cleaned some of the substrates with oxygen plasma before exfoliation. This cleaning allowed us to exfoliate larger samples, as required for the reflection contrast measurements.

The Raman spectroscopy measurements were performed in a commercial micro-Raman setup (Renishaw In-Via) in a back-scattering geometry. A 100x objective (NA = 0.85) was used to collect the scattered photons, which were analyzed in a spectrometer equipped with a grating of 2400 l/mm. The laser power on the sample was about 5 μW (for 532-nm excitation) and 20 μW (for 633-nm excitation). The measurements of reflectance contrast were performed on $MoTe_2$ flakes exfoliated on the transparent SiO_2 substrates. The experimental setup consisted of a quartz tungsten halogen source in combination with a microscope using a 50x objective (NA = 0.85). A monochromator dispersed the reflected light from the sample onto a liquid nitrogen cooled Si or InGaAs CCD array. We extracted the peak positions and linewidths of the reflectance contrast measurements by fitting multiple Lorentzian line shapes to the experimental data. PL measurements were performed in the same setup with a 100x objective (NA = 0.95) to collect the backscattered emission. For excitation, we used a HeNe laser or a 647-nm solid-state laser. The excitation power level was kept below 10 µW. Reflected and elastically scattered laser radiation was suppressed by a long-pass filter in front of the monochromator. All experiments were performed at room temperature.

Before discussing the experimental results, we comment briefly on the long-term stability of the $MoTe_2$ samples used in this study. For exfoliated 1Ls held under ambient conditions, a decrease in the PL yield was consistently seen within one or two months. The degradation of $MoTe_2$ layers, as judged by the optical contrast and PL yield, was found to depend strongly on the treatment of the substrate. For substrates cleaned by the oxygen plasma before exfoliation, the lifetime of 1Ls decreased further, even down to the range of a day. Therefore, the samples were stored in a vacuum environment, and the data presented in this study were obtained from fresh samples. While we cannot exclude the possibility that the magnitude of the reflectance contrast spectra was affected by sample aging, the energy and line width of the resonances did not change even for heavily degraded 1Ls. Encapsulation with h-BN layers improved the stability of the $MoTe_2$ 1Ls.

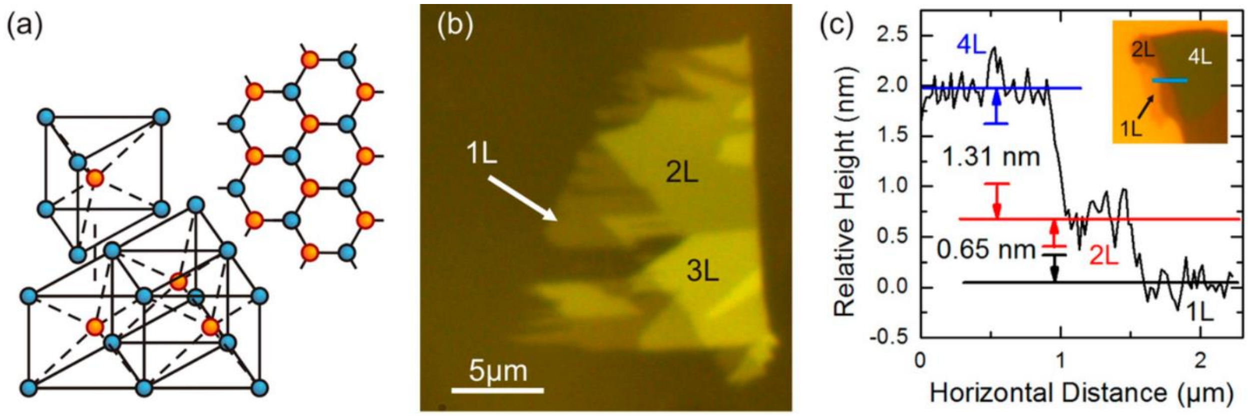

Figure 4-1: (a) Crystal structure of α-$MoTe_2$. (b) Optical image of few-layer $MoTe_2$ exfoliated on SiO_2, showing regions with thicknesses from a 1L to 3L. The image contrast has been enhanced to improve the visibility. (c) Representative AFM profile showing the relative heights of a $MoTe_2$ sample exfoliated on SiO_2/Si, with the corresponding trace indicated by the blue line in the optical image in the inset.

We exfoliated micron-sized few-layer flakes of $MoTe_2$ on both SiO_2 and SiO_2/Si. An example of $MoTe_2$ layers on a SiO_2 substrate is shown in Figure 4-1(b). We can identify layer thicknesses varying from the 1L through 3L in different regions. Measurements with an atomic force microscope (AFM) were performed on the samples to determine the layer thickness; a representative height profile for a flake on SiO_2/Si is presented in Figure 4-1(c). The measured interlayer separation lies in the range of 0.6 - 0.65 nm, which is consistent, within experimental uncertainty, with the bulk layer spacing of 6.982±0.002 Å reported in the literature.[1] The spacing between the 1L and the substrate determined by AFM (not shown) varies significantly in different measurements and presumably reflects changes in the tip-surface interaction between the substrate and the sample[80] and possibly the presence of adsorbates under the sample.[81] To identify the samples of 1L thickness, we, therefore, made use of Raman spectroscopy. In particular, the inactivity of the Raman B^1_{2g} mode at 289 cm^{-1} permits unambiguous identification of 1Ls, as discussed below. After calibration, we could also simply use the green channel of the optical images, together with Raman measurements, for rapid and reliable identification of layer thickness.

Figure 4-2(a) displays the optical spectra from the visible to the near-infrared for samples with thicknesses of one to three layers. The data are presented as reflection contrast spectra, *i.e.*, $\Delta R/R = (R_{MoTe+S} - R_S)/R_S$, where R_{MoTe+S} and R_S denote, respectively, the reflectance of $MoTe_2$ on the substrate and of the bare substrate. All of the presented spectra were measured on samples for a thick, transparent SiO_2 substrate. For a sample on such a transparent substrate with sufficiently small reflection contrast, the reflection contrast spectrum is proportional to the absorption spectrum of the corresponding film. In particular, we can obtain the absorbance $\mathcal{A}$ of the free-standing layer from the optical contrast as $\mathcal{A} = \frac{1}{4}(n_S^2 - 1)(\frac{\Delta R}{R})$,[52-54] where n_S denotes the refractive index of the substrate.[82]

Several peaks are clearly observable in the spectra of Figure 4-2a, which we have labeled according to the bulk assignments of Wilson and Yoffe.[83] These spectroscopic features are associated with transitions in different parts of the Brillouin zone of $MoTe_2$. The A, B and A', B′ pairs have been identified as excitonic transitions, with the A-B splitting arising from spin-orbit interactions.[83-84] As for other TMDC 1Ls, the A and B peaks are assigned to excitonic peaks associated with the lowest direct optical transition at the K point.[18,63,85] The splitting between A, B and A′, B′ has been related to interlayer interactions.[84,86] The additional A′, B′ pair exists in other TMDC materials but has recently also been observed in WSe_2 at the 1L thickness,[61] where interlayer interactions are obviously absent. For the bulk $MoTe_2$ crystal, the C and D features have been attributed to regions of parallel bands near the Γ point of the Brillouin zone of bulk $MoTe_2$[86] and similar parallel bands in 1Ls of other TMDC materials.[17,87]

The infrared part of the 1L spectrum is presented in greater detail in Figure 4-2 (b). In this Figure, we also indicate the corresponding absorbance $\mathcal{A}$ for a free-standing 1L, determined according to the relation given above. To analyze our data further, we fit the resonances in the absorption spectrum to Lorentzian components. The red line in Figure 4-2(b) displays the contributions of the A and B features to the fit. The line shape of the A peak in our experimental data reveals the excitonic character of the transitions, being well described by a single Lorentzian feature, with no signature of free-carrier contributions to an interband transition.

The energy difference between the A and B features of the other TMDC systems is known to arise from the spin-orbit-splitting of the similar bands, mostly governed by the valence-band splitting.[63,88] Theory predicts the same behavior for $MoTe_2$.[89] The center positions of the two excitonic transitions are found to be 1.095 ± 0.005 eV and 1.345 ± 0.005 eV. Repeated measurements on other 1L $MoTe_2$ flakes on transparent substrates yield very similar positions of the A and B peaks, with deviations of only a few meV. The spectral width of the A exciton absorption is about 50 meV (full width at half maximum, FWHM). The B exciton width is several times greater, in accordance with the trend for the features in bulk $MoTe_2$ crystals.[83] Based on the positions of the A and B features, we infer a spin-orbit splitting of 250 meV for 1L $MoTe_2$. This splitting is significantly greater than the corresponding value of 150 meV for MoS_2.[59]

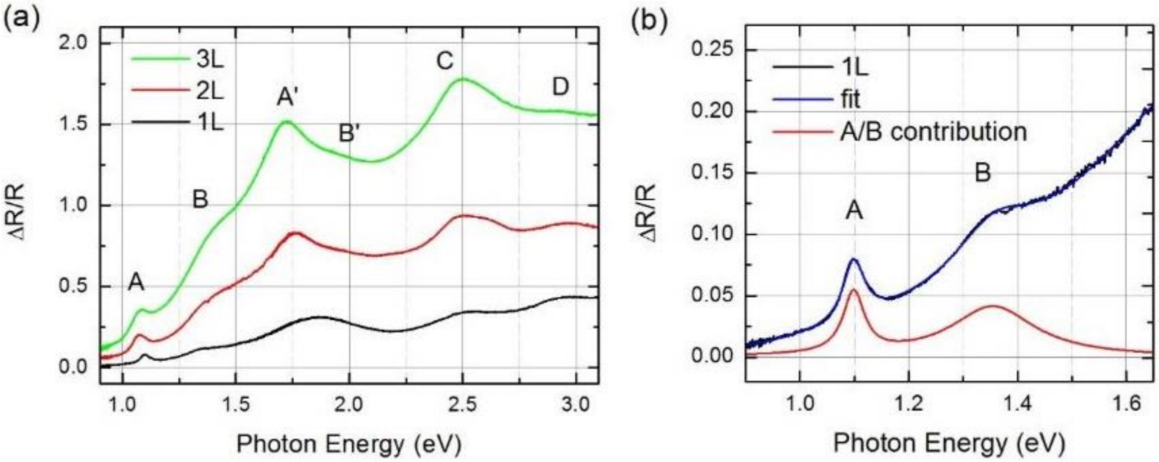

Figure 4-2: $MoTe_2$ reflectance contrast spectra (a) for 1L, 2L and 3L crystals on SiO_2 substrates. (b) Detail of the spectrum for the 1L in the infrared (black curve). The right vertical scale displays the corresponding absorbance $\mathcal{A}$ for the free-standing 1L. We fit the spectrum with multiple Lorentzian peaks (blue curve), with the A and B contributions shown separately (red curve).

Comparison of the 1L spectrum with the 2L and 3L spectra shows that most of the peaks shift only slightly in energy, with the overall reflectance contrast increasing approximately linearly with thickness. Like other TMDC materials, the A exciton resonance shifts by about 20 meV to lower energy from 1L to 2L, with even smaller redshifts for further increases in layer thickness. The line width of the A exciton also increases with layer thickness. The A exciton width of the 2L is 20 meV larger than that of the 1L. A more noticeable change is seen for the A'/ B' peak area, with the A' feature shifting strongly towards higher energy with decreasing thickness.

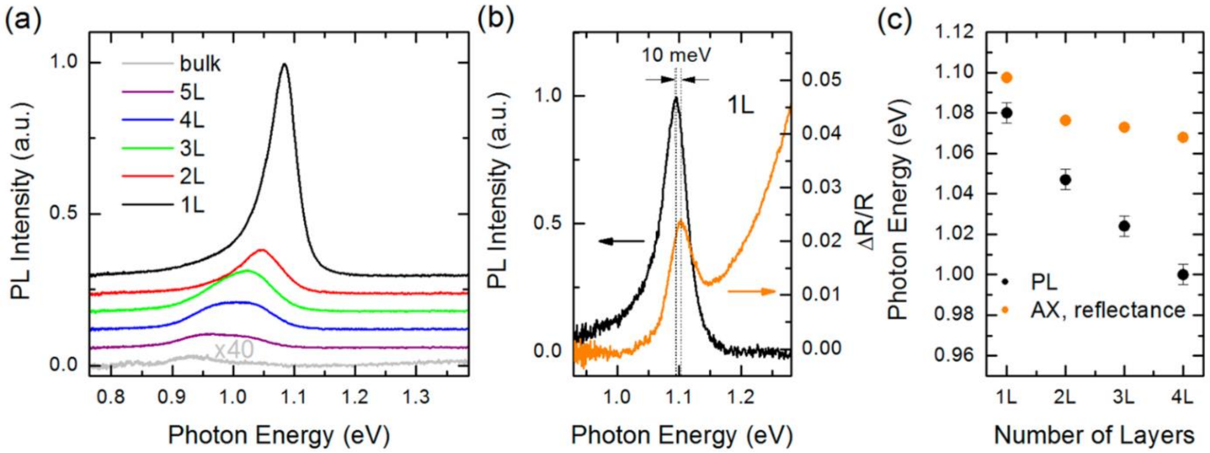

Figure 4-3: Comparison of PL and Reflection Contrast of $MoTe_2$ (a) Thickness-dependent PL spectra on SiO_2/Si. The spectra are shifted vertically for clarity. The bulk data were measured with higher excitation power but normalized in the figure assuming linear response. (b) Comparison of PL and reflectance contrast spectra for a 1L $MoTe_2$ on a SiO_2 substrate. (c) Photon energy of the peak in the PL spectra in (a) and of the A exciton resonance (AX) extracted from reflectance contrast measurements for samples of 1-4 layers.

To gain insight into the nature of the optical transition of the lowest excitonic state, we measured PL spectra for different layer thicknesses of $MoTe_2$ crystals. Figure 4-3(a) shows the thickness-dependent PL for a flake exfoliated on a SiO_2/Si substrate. The 1L PL spectrum exhibits a single emission peak, with a maximum at a photon energy of 1.08 eV and a width of 55 meV (FWHM). With increasing layer thickness, the maximum of the PL shifts to significantly lower energies. For the bulk, we find a maximum in the PL intensity around 0.93 eV. The 1L PL is far stronger than that of the bulk. For the sample studied here, the PL is enhanced approximately by three orders of magnitude.

For the 1L, the position of the PL peak lies very close to the A exciton resonance seen in the absorption spectrum. Figure 4-3(b) shows a direct comparison of the absorption and emission spectra for the same sample on a SiO_2 substrate. The energy shift between the two peaks is about 10 meV. For different 1Ls on SiO_2/Si substrates, the position of the emission peak varies on the order of ~10 meV and is mostly lower in energy. The best samples show both narrow PL spectra and very slight spectral shifts between the absorption and emission peaks.

For thicker layers, the A exciton resonance in the reflectance contrast spectra and the PL maxima both shift towards lower energies. However, the rate of the red shift of these two features with increasing thickness is quite different. Figure 4-3c compares the positions of absorption maxima from Figure 4-2 with those of the emission maxima in Figure 4-3. Note that the measurements were performed on different samples, whence the somewhat larger shift for the 1L. The A exciton absorption seen in $\Delta R/R$ measurements displays much smaller shifts and remains almost constant for thicker layers, while the PL maximum continues to shift to lower energies with increasing thickness. We attribute this shift between features in the absorption ($\Delta R/R$) and emission (PL) spectra to the emergence of an indirect transition at lower energies, as occurs, for example, in MoS_2 and WS_2.[59,61,90] Although we do not expect the lower-lying indirect transition to yield measurable absorption, it will still contribute to the emission spectrum, as is the case for the other TMDC 1Ls. We do not observe an additional emission peak in the PL spectra of thicker layers (2L-5L) near the PL and absorption maximum of the 1L. This behavior contrasts to reported spectra in other TMDC materials in which the direct transition from the A exciton remains visible in the PL spectra of thicker layers. [59,61,90] However, the relative strength of the PL peaks from the A exciton and the indirect transition depends strongly on the material and the excitation conditions. The PL from the A exciton in few-layer WSe_2 is, for example, usually rather weak.[61] In $MoTe_2$ the width of the features and the relatively small shifts further hinder identification of two emission peaks. The red shift for the A exciton peak in the reflectance contrast spectra in the 2L sample compared to the 1L sample is

21 meV. In comparison, the maximum of the PL peak seen in Figure 4-3a shifts by 33 meV. We therefore conclude that the 2L PL is governed primarily by the emerging indirect transition. For a sample probed at low temperature (70 K), we do, in fact, observe two distinct emission peaks for PL from the 2L crystal as shown in Figure 4-4

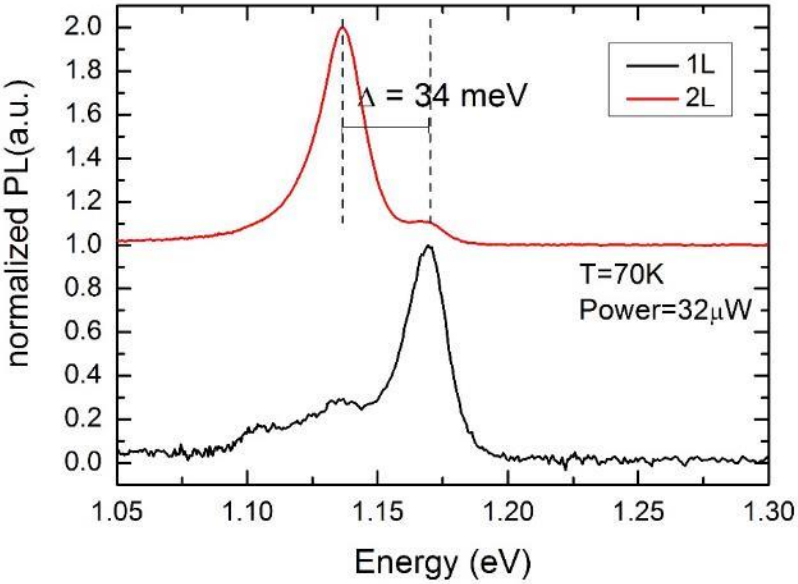

Figure 4-4: PL emission from 1L and 2L $MoTe_2$ measured at a temperature of 70 K. The PL spectra are each normalized to the maximum value. The 2L spectrum has been shifted up for clarity.

The low-temperature PL spectra for 1L and 2L $MoTe_2$ are presented in Figure 4-4. In addition to an expected shift of the features to higher energy compared to the room-temperature spectra, the low-temperature emission spectrum for the 2L shows two distinct peaks. The weak, higher-energy peak, which is absent in the room-temperature PL spectra, is nearly coincident with PL peak of the 1L. It is therefore attributed to hot luminescence from the direct transition at the K point of the Brillouin zone, as is also seen, for example, in MoS_2 2Ls. The energy difference Δ between the two emission features in the 2L is 34 meV, a value that we take as a measure of the energy difference between the direct and indirect transitions in the 2L. At room temperature, the increased line width of the PL hinders the identification of a separate hot luminescence feature from the direct transition in the 2L.

Also, the low-temperature spectra of the 1L exhibit several weaker features in the lower-energy tail of PL. Similar features have been seen in the PL of other transition metal dichalcogenide 1Ls at low temperature and have been attributed to the trap states associated with defects.

The redshift of the PL maximum of ~100 meV from 1L to 5L is relatively small compared to that for MoS_2 and WS_2 crystals. The observed trend is, however, consistent with theoretical predictions of a decreased redshift as the chalcogen is changed from S to Se to Te in Mo- and W-based TMDCs.[91] The result is also compatible with the fact that the redshift of the indirect transition is smaller in WSe_2 than in WS_2.

The strength of the PL from 1L $MoTe_2$ depends strongly on the choice of substrate. The PL yield is relatively low for tested transparent substrates (crystalline SiO_2, as well as crystalline Al_2O_3), but can be as much as two orders of magnitude greater for SiO_2/Si wafers. Although interference effects are present that enhance the yield for the SiO_2/Si substrate,[92] this can account only for a small part of the observed increase in PL yield. We note that changes of PL yield in our samples are typically also accompanied by shifts of about 10 meV in the position of the emission maxima. This suggests that the difference in PL yield may be linked to the charge transfer effects from the substrate, which can shift the ratio of emission from charged and neutral excitons and also alter the total strength of the PL emission.[93-94]

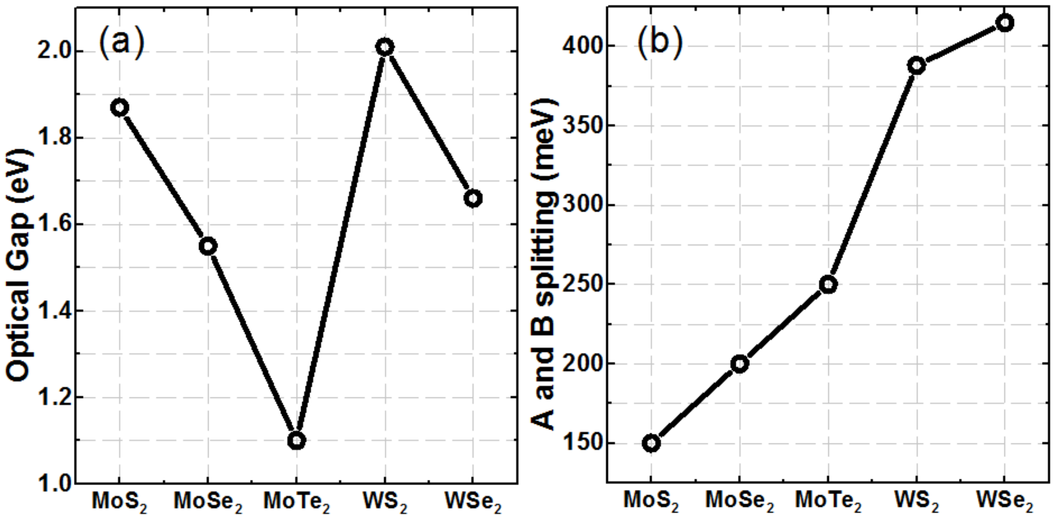

Figure 4-5: Comparison of 1L semiconducting group VI TMDCs. (a) Optical gap and (b) energy difference between the A and B excitons.

We plot the optical gap and the energy difference between the A and B excitons of the 1Ls of semiconducting MoS_2, $MoSe_2$, $MoTe_2$, WS_2 and WSe_2 in Figure 4-5.[14] We note that $MoTe_2$ has the lowest band gap and changing the chalcogen atom modifies the optical gap more than the metal atom. The situation is opposite for the A and B splitting. We hope that this quick comparison can inspire band structure engineering of TMDC alloys.

Finally, we wish to comment briefly on the capability of Raman measurements for identifying the thickness of different layers. Figure 4-6 shows Raman spectra for the few-layer flake in Figure 4-1c and a bulk $MoTe_2$ sample with excitation at wavelengths of 532 nm and 633 nm. The characteristic phonon modes of $MoTe_2$,[5,9] A_{1g} at 170 cm^{-1}, E^1_{2g} at 234 cm^{-1} and B^1_{2g} at 289 cm^{-1}, have recently been observed and characterized for 1L and few-layer samples.[76] The B^1_{2g} mode, inactive in bulk, is allowed for few-layer $MoTe_2$ due to the breaking of translational symmetry.[95] Since it is also absent for the 1L, it is observed to have maximum intensity for the 2L and then to decrease with increasing thickness.

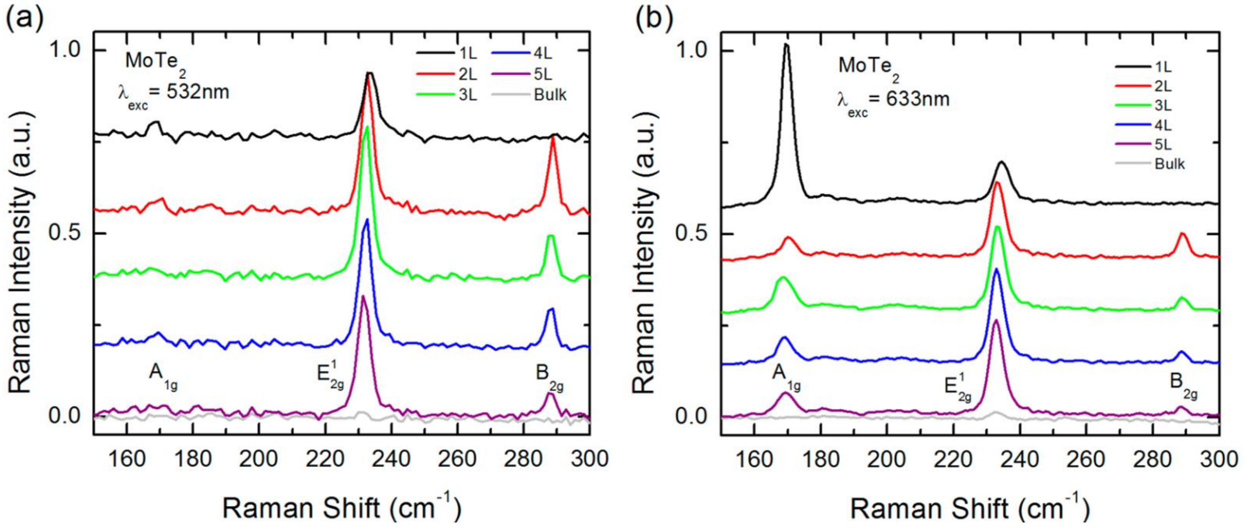

Figure 4-6: Raman spectra of 1L – 5L and bulk $MoTe_2$ for the excitation wavelengths of (a) 532 nm and (b) 633 nm. The spectra are offset for clarity. For simplicity, the Raman modes are labeled according to bulk notation.

The 1L and few-layer Raman responses differ strikingly for excitation at 633 nm compared to that for 532-nm excitation. In the former case (Figure 4-6b), the A_{1g} mode is unusually strong. For the 1L the A_{1g} mode has by far the strongest Raman response; for few-layer samples (except the 2L) this mode is stronger than B^1_{2g}. For 532-nm excitation, on the other hand, the A_{1g} mode is consistently weak. As is common for other few-layer systems, analyzing the relative shift and amplitudes of the E^1_{2g} and B^1_{2g} Raman modes aids in the identification of sample thickness, but is not always sufficiently precise. However, for 633-nm excitation, the Raman spectra of 1L and 2L samples exhibit such different A_{1g} and B^1_{2g} mode intensities compared with thicker layers that they can be readily identified. Since the intensities of E^1_{2g} and B^1_{2g} modes scale in a similar way with layer thickness for both excitation wavelengths, the peak at 170 cm^{-1}, which we have heretofore attributed to A_{1g} vibration, may, in fact, correspond to a different type of Raman response. A candidate for the strong response at 170 cm^{-1} is a resonant two-phonon Raman process involving acoustic phonons. In other

TMDCs,[96-98] resonant enhancement of such a second-order Raman process has given rise to a peak near the Raman shift of the A_{1g} optical mode. A deeper analysis of this phenomenon would require detailed studies of the Raman response as a function of the laser excitation wavelength.

4.3. Conclusion

In summary, we have successfully exfoliated 1L and few-layer $MoTe_2$ crystals on various substrates and have applied absorption and emission (PL) spectroscopy to characterize these materials' optical properties. For the 1L, the optical gap is located at 1.10 eV, and the intense PL at the peak of the optical absorption feature provides strong evidence that 1L $MoTe_2$ is a direct gap material. The shift of the PL to lower energies with little change in the position of the absorption feature indicates that thicker layers are indirect-gap semiconductors, showing a behavior analogous to that exhibited by MoS_2. For the 1L, we observe a spin-orbit splitting of the A and B excitons of 250 meV. We present Raman scattering data showing that, in contrast to the case of excitation with 532-nm radiation, the spectra for 633-nm excitation permit unambiguous identification of 1L and 2L $MoTe_2$ crystals.

5. Probing the Band Structure of Monolayer $MoTe_2$ and $Mo_{0.9}W_{0.1}Te_2$ via Strain

We study the optical properties of ultrathin $Mo_{0.9}W_{0.1}Te_2$ via Raman scattering, PL, and optical absorption measurements. We observe that the material transitions from indirect to direct band gap in the 1L limit at 1.1 eV, very close to its $MoTe_2$ counterpart. We also apply tensile strain to 1L $MoTe_2$ and $Mo_{0.9}W_{0.1}Te_2$ to tune their band structures, and we observe that their band gaps decrease by about 70 meV at ~2.3% strain. The PL peaks show a decline in the spectral widths with increasing strain. We attribute the decline in the spectral widths to weaker exciton-phonon intervalley scattering. These observations show that ultrathin $MoTe_2$ and $Mo_{0.9}W_{0.1}Te_2$ extend the range of transition metal dichalcogenides further into the near infrared and demonstrate their potential for applications in flexible electronics and optoelectronics. Moreover, strain proves to be an effective external field to explore the fundamental properties of ultrathin transition metal dichalcogenides.

5.1. Introduction

Atomically thin layers of transition metal dichalcogenides (TMDCs), such as $MoTe_2$, have been extensively studied for fundamental physics and applications.[13,15] Tuning their optical properties, which can be achieved through doping, alloying, strain, and heating is crucial for understanding the light-matter interaction and for various applications in flexible electronics and optoelectronics. Optical properties of atomically thin $MoTe_2$ has recently been characterized, [24-26,99-100] and theoretical studies have proposed that the factors above can significantly alter its band structure.[19-20,101-103] However, to date, few studies have experimentally studied the effects of strain or alloying on $MoTe_2$.[22,29,104]

Here we study the optical properties of atomically thin crystals of the $Mo_{0.9}W_{0.1}Te_2$ alloy via Raman scattering, PL, and absorption measurements, and compare them with those of $MoTe_2$. We also measure PL while applying tensile strain to the 1L crystals of both compounds to alter their band structures. We observe that the optical band gap (to be called "band gap" throughout the chapter) redshifts with increasing strain, as expected. The 1Ls of the two materials acquire a band gap of ~1.01-1.02 eV at the highest strain applied. We have thus extended the optical range of 1L TMDCs further into near infrared. This finding shows that atomically thin TMDCs can potentially be used for applications that require strain-sensitive optical absorption in the near infrared.

5.2. **Growth and Raman Spectroscopy of $MoWTe_2$**

We grow $Mo_{1-x}W_xTe_2$ and $MoTe_2$ crystals using the chemical vapor transport (CVT) method. The W content in the $Mo_{1-x}W_xTe_2$ determined from the energy dispersive spectroscopy (EDS) spectra is x = 0.1±0.01. Crystal phases of the $Mo_{0..9}W_{0.1}Te_2$ alloys are determined by powder X-ray diffraction (XRD) and aberration-corrected high angle annular dark field scanning transmission electron microscopy (Cs – corrected HAADF-STEM), as shown in Figure 5-1. The HAADF-STEM image in Figure 5-1b demonstrates that the crystal is in the 2H phase.

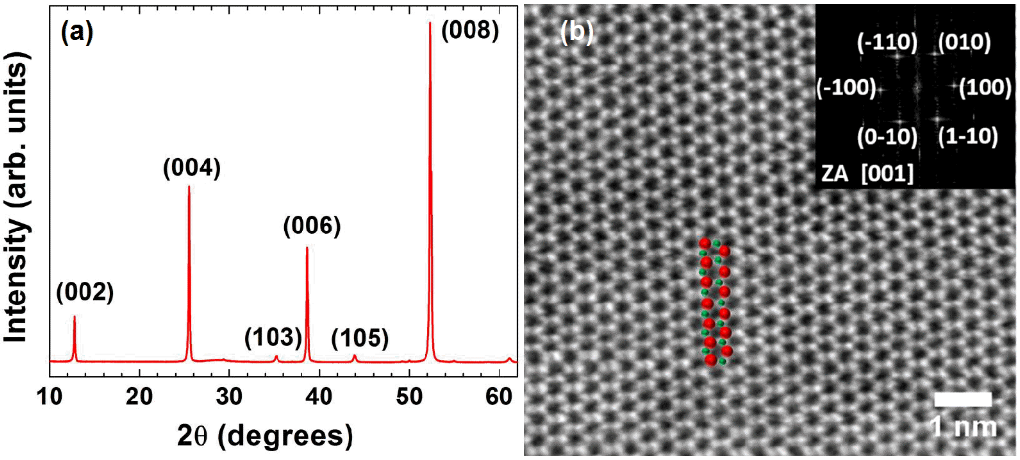

Figure 5-1: (a) Powder XRD pattern (b) HAADF-STEM image of a 2H $Mo_{0.9}W_{0.1}Te_2$ sample together with the overlapped structural model; red spheres: Mo/W atoms; green spheres: Te atoms. Inset: FFT emphasizing the [001] zone axis.

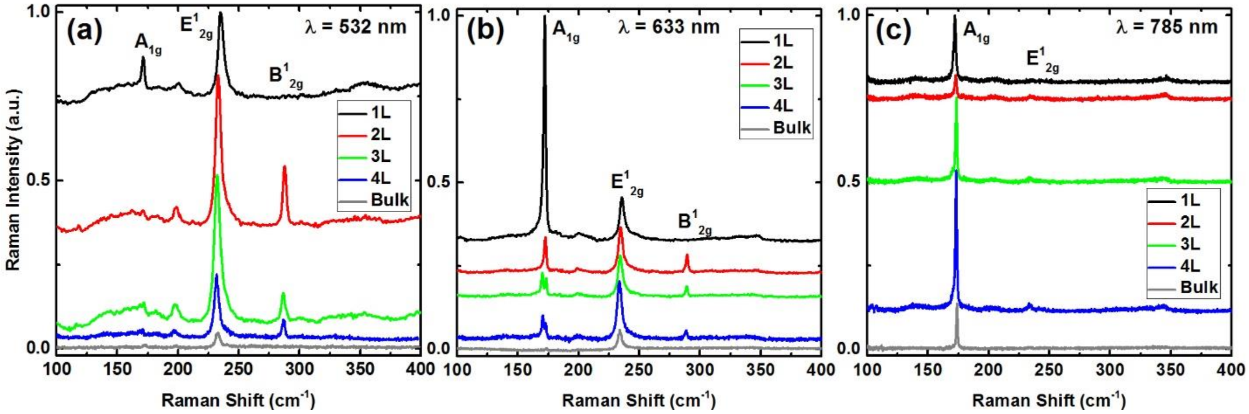

Figure 5-2: Raman spectra of 1L-4L and bulk $Mo_{0.9}W_{0.1}Te_2$ (modes labeled with bulk notation) with excitation wavelengths of (a) 532 nm, (b) 633 nm, and (c) 785 nm. 1L-4L spectra are vertically offset for clarity.

We transfer atomically thin crystals from bulk $MoTe_2$ and $Mo_{0.9}W_{0.1}Te_2$ crystals by mechanical exfoliation onto a thick polydimethylsiloxane (PDMS) substrate (base: curing agent ratios of 10.5: 1). The PDMS substrate has negligible optical absorption over the spectral range of interest.[105] The thicknesses of the ultrathin crystals are determined by Raman spectroscopy[24] and optical contrast. For the optical measurements with strain, we transfer 1L crystals to polyethylene naphthalate (PEN) flexible plastic substrates due to their high Young's modulus of ~5 GPa .[106-107]

The Raman spectroscopy measurements are performed in a commercial micro-Raman setup in a backscattering geometry. A 100× objective (NA = 0.9) is used to collect the scattered photons, which are analyzed in a spectrometer equipped with a grating of 1800 lines/mm. The laser power on the samples is about 200 µW (for 532 nm excitation), 140 µW (for 633 nm excitation), and 200 µW (for 785 nm excitation), which is sufficient for obtaining a good signal-to-noise ratio without damaging the samples. The reflectance contrast setup consists of a quartz tungsten halogen source combined with a microscope using 100× objectives (NA = 0.95 and 0.9). A monochromator disperses the reflected light from the sample onto an electronically cooled Si or liquid-nitrogen cooled InGaAs CCD array. The peak positions and spectral widths (full width at half maximum; FWHM) of the reflectance contrast measurements are extracted by fitting multiple Lorentzian lineshapes to the experimental data. PL measurements are performed in the same setup with a 100× objective (NA = 0.95) to collect the backscattered emission. For excitation, we use a HeNe or a 671 nm solid-state laser. The excitation power level is around 10 µW. Backscattered laser radiation is suppressed by a long-pass filter in front of the monochromator. All experiments are performed at room temperature.

Figure 5-2 shows the Raman spectra of 1L-4L and bulk $Mo_{0.9}W_{0.1}Te_2$ with excitation wavelengths of 532 nm, 633 nm, and 785 nm. We note that the relatively low band gap of $MoTe_2$ and $Mo_{0.9}W_{0.1}Te_2$ compared to other TMDCs enables the use of higher excitation wavelengths for resonant Raman spectroscopy. We observe the following first-order Raman modes (due to transitions at the Γ point in the Brillouin zone) : Out-of-plane A_{1g} (A'_1 for odd, A_{1g} for even layers), in-plane E^1_{2g} (E' for odd, E_g for even layers), and out-of-plane B^1_{2g} (A''_2 for 1L, A'_1 for odd, A_{1g} for even layers), which is Raman inactive in 1L and bulk crystals.[24,76,95,108-112] For

1L $Mo_{0.9}W_{0.1}Te_2$, the A_{1g} mode is at ~171-172 cm^{-1}, and the E^1_{2g} mode is at ~235 cm^{-1}. The weaker peaks at ~200 cm^{-1} and ~345 cm^{-1} have recently been attributed to second-order Raman processes[109] and appear to be stronger in $Mo_{0.9}W_{0.1}Te_2$ than in $MoTe_2$.

The Raman modes of $Mo_{0.9}W_{0.1}Te_2$ match those of $MoTe_2$, with the A_{1g} and E^1_{2g} modes slightly blueshifted and the B^1_{2g} mode slightly redshifted from those of $MoTe_2$. As the W content increases in alloys of Mo and W dichalcogenides (e.g. $Mo_{1-x}W_xS_2$ and $Mo_{1-x}W_xSe_2$), a redshift in the E^1_{2g} and B^1_{2g} modes and a blueshift in the A_{1g} mode occurs.[98,113-116] Using a simplified linear triatomic molecule model for 1L and 2L where interlayer interactions of the vibrations are insignificant, we expect the increased W content in $Mo_{0.9}W_{0.1}Te_2$, and therefore an increase in the effective mass of the transition metal, to result in a redshift of modes as compared to $MoTe_2$.[117] We observe this redshift in the B^1_{2g} mode. However, the frequency of the A_{1g} mode depends more on bond strength than on mass of the transition metal since it does not vibrate in this mode.[95] Since W-Te bonds are stronger than Mo-Te bonds,[118] adding W to $MoTe_2$ leads to stiffening of the bonds which accounts for the observed blueshift of the A_{1g} mode. As opposed to other TMDC alloys, we observe a blueshift in the E^1_{2g} mode for 1L and 2L from $MoTe_2$ to $Mo_{0.9}W_{0.1}Te_2$ and conclude that this blueshift also results from increased bond strength, which seems to have a stronger effect on the frequency of the mode than increased mass.

Next, we examine the relative intensities of the Raman modes. For both $MoTe_2$ and $Mo_{0.9}W_{0.1}Te_2$, the E^1_{2g} mode is strongest for all thicknesses when measured with the 532 nm laser. The A_{1g} mode is strongest for 1L and becomes much weaker with increasing thickness, as shown in Figure 5-2a. The 633 nm laser can be used to distinguish between 1L, 2L, and 3L crystals in both $Mo_{0.9}W_{0.1}Te_2$ and $MoTe_2$.[24] The A_{1g} mode is strongly enhanced compared to the E^1_{2g} mode for 1L crystals which is attributed to a resonance effect as the energy of the laser is close to that of the A' or B' excitons (see Figure 5-3b).[110] For 2L crystals, the A_{1g} and B^1_{2g} modes are comparable in intensity but weaker than the E^1_{2g} mode, and for 3L and 4L crystals, the A_{1g} mode splits into 2 peaks (A_{1g}(R1) and A_{1g}(R2)), known as Davydov splitting,[110,119] and is stronger than the B^1_{2g} mode (see Figure 5-2b). The ratio of the B^1_{2g} to E^1_{2g} mode can also be used to identify thickness in few-layer crystals using both 532 and 633 nm lasers.[26,76] Using the 785 nm laser, we observe that the E^1_{2g} mode is much weaker than the A_{1g} mode for all crystal thicknesses. For the thicknesses we have measured, the A_{1g} mode is weakest for 2L and strongest for 4L crystals in both $Mo_{0.9}W_{0.1}Te_2$ and $MoTe_2$ (see Figure 5-2c). The reason for this non-monotonic change of the intensity of the A_{1g} mode with increasing thickness is unclear and can be the focus of a future study. The B_{2g} mode does not appear in the 785 nm Raman spectra for any crystal thickness, similar to the case in MoS_2 and $MoSe_2$ for laser excitation energies far from the C exciton.[108,120] Calculations have shown that the A and B excitons have wave functions that are mainly confined to the individual layers, and it has been predicted that for excitation energies near the A and B excitons the active B_{2g} mode of the few-layered crystals is seen as the inactive B_{2g} mode of 1Ls. Therefore the B_{2g} is not observed in few-layered crystals with the excitation energy of 785 nm.[108,120] However, the C exciton has been calculated to have a wave function that is not confined to the individual layers,[16,87] so lasers with excitation energies closer to the C exciton yield Raman spectra with stronger B_{2g} modes.

5.3. **Absorption and PL on Ultrathin MoWTe$_2$**

To understand the band structure of Mo$_{0.9}$W$_{0.1}$Te$_2$, we perform PL measurements. Figure 5-3a displays the PL spectra of 1L-4L and bulk Mo$_{0.9}$W$_{0.1}$Te$_2$. The 1L spectrum exhibits a single emission peak, with the maximum located at 1.10 eV and an FWHM of ~50 meV. The FWHM of the 2L is about 20 meV larger than that of the 1L. We clearly see that the PL intensity decreases and the peak position redshifts with increasing layer thickness. The FWHM of the peaks appears to increase significantly from 1L to bulk. For the bulk, we find a maximum in the PL intensity at around 0.98 eV. The PL intensity of 1L is about three orders of magnitude larger than that of the bulk.

In a view to comment on the nature of the peaks observed in the PL spectra and understand why the changes discussed above occur with increasing material thickness, we measure the optical spectra of 1L-3L Mo$_{0.9}$W$_{0.1}$Te$_2$, as displayed in Figure 5-3b. The data is presented as the reflection contrast, that is $\Delta R/R = (R_{MoWTe+PDMS} - R_{PDMS})/R_{PDMS}$, where $R_{\mathrm{MoWTe}+PDMS}$ and R_{PDMS} represent the reflectance of the thin Mo$_{0.9}$W$_{0.1}$Te$_2$ sample on the PDMS substrate and of the bare PDMS substrate, respectively. For a sample with sufficiently small absorbance on a thick transparent substrate, as in our case, we can determine the absorbance $\mathcal{A}$ of the unsupported thin Mo$_{0.9}$W$_{0.1}$Te$_2$ from $\Delta R/R$ as $\mathcal{A} = \frac{1}{4}(n_{PDMS}^2 - 1)(\frac{\Delta R}{R})$,[52-54] where n_{PDMS} denotes the refractive index of PDMS.[121] We can thus probe the absorption spectra of sufficiently thin samples through measurements of their reflection contrast.

We expect to observe only the direct optical transitions in the reflection contrast spectrum since the indirect transitions give rise to a very weak contribution to the absorbance.

Several features are seen in the spectra of Figure 5-3b, and we expect them to arise from mechanisms similar to $MoTe_2$. Thus, we have labeled them according to the bulk assignments of Wilson and Yoffe[83] as previously done for the case of $MoTe_2$.[24] These spectroscopic features are associated with transitions in different parts of the Brillouin zone of $Mo_{0.9}W_{0.1}Te_2$. The A, B and A', B' pairs have been identified as excitonic transitions with the A-B splitting arising from spin−orbit interactions.[84] As for other TMDC 1Ls, the A and B peaks are assigned to excitonic peaks associated with the lowest direct optical transition at the K-point.[18,63,85] The C and D features have been attributed to regions of parallel bands near the Γ point of the Brillouin zone of bulk $MoTe_2$[86] and similar parallel bands in 1Ls of other TMDCs.[17,87]

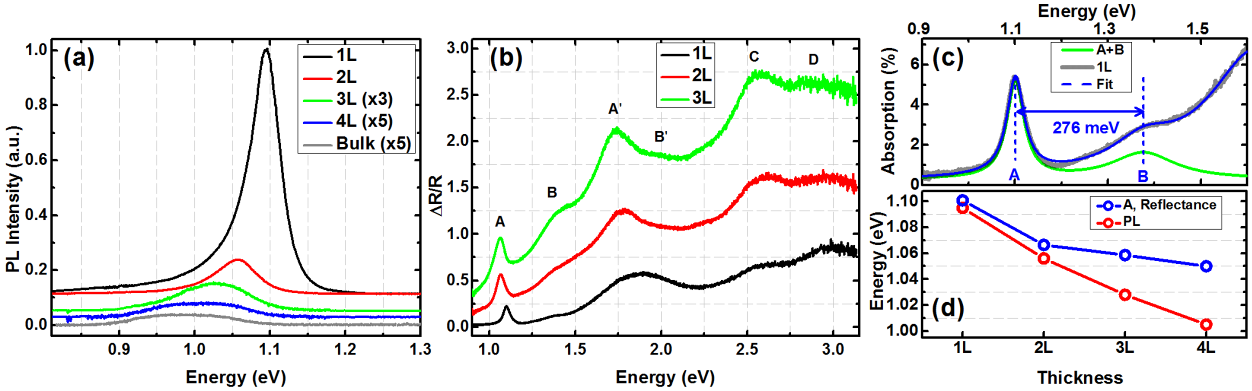

Figure 5-3: (a) PL spectra of 1L-4L and bulk, (b) ΔR/R spectra for 1L- 3L $Mo_{0.9}W_{0.1}Te_2$ crystals. (c) The absorption spectrum for the 1L in the infrared. We fit the spectrum to multiple Lorentzian peaks to extract the peak positions of the A and B excitons. (d) Comparison of the A exciton and PL peak positions as a function of crystal thickness. 1L-4L spectra are vertically offset for clarity in (a).

We now compare the PL and reflection contrast response of $Mo_{0.9}W_{0.1}Te_2$ for different thicknesses. Figure 5-3b shows that the reflection contrast increases and the A exciton redshifts with increasing thickness. The PL spectra in Figure 5-3a indicate that the peak position also redshifts; however, the rate of the redshift of the PL peak is faster than that of the A exciton, and the PL intensity decreases as opposed to that of the A exciton. We report the position of the A exciton and the PL peak position as a function of thickness in Figure 5-3Figure 5-3c. The A exciton redshifts by ~33 meV to ~1.067 meV for 2L and continues shifting gradually with increasing thickness. However, the PL peaks redshift more than the A exciton peaks such that the two are separated by ~5 meV for 1L, but ~45 meV for 4L.

We attribute this large difference to the emergence of an indirect transition at lower energies than the A exciton with increasing thickness as observed in other TMDCs.[59,61] We expect the indirect band gap to contribute to PL but not to absorption. We thus conclude that the 1L $Mo_{0.9}W_{0.1}Te_2$ acquires a direct band gap unlike the few-layer crystals thicker than 2L, in accordance with the $MoTe_2$ counterpart. Even though the PL intensity is significantly smaller for 2L than it is for 1L, we find it hard to label 2L as an indirect gap material since the PL peak and the A exciton are separated by only ~10 meV. However, the 20 meV increase in the FWHM of the PL and A exciton peaks of 2L as compared to 1L strongly indicates the presence of a scattering channel for the A exciton in the 2L. We also would like to mention that there have been different opinions on the nature of the 2L $MoTe_2$ band gap, both at room[24-25] and low temperatures.[26]

To compare the features observed in $Mo_{0.9}W_{0.1}Te_2$ to those in $MoTe_2$, we fit the reflectance contrast spectrum with Lorentzian lineshapes. The infrared part of the 1L spectrum with the resultant fit is given in greater detail in Figure 5-3c. The vertical axis is the absorbance of the unsupported film calculated by the formula mentioned above. We find that the A and B features are located at about 1.10 and 1.38 eV, respectively. The same features are located at about 1.10 and 1.35 eV, respectively, for 1L $MoTe_2$. We note that the direct band gap, or A exciton, position in $Mo_{0.9}W_{0.1}Te_2$ is not very different from that of $MoTe_2$, which can be understood by the fact that for a given chalcogen (S, Se), the band gaps of Mo and W dichalcogenides are comparable.[14] The A-B splitting is found to be ~276 meV which is higher than the $MoTe_2$ value of 250 meV.[24] We attribute this increase to the presence of W since dichalcogenides of W have significantly higher A-B splitting than those of Mo.[14,122-123]

5.4. Strain-Tuned PL on 1L $Mo_{0.9}W_{0.1}Te_2$ and $MoTe_2$

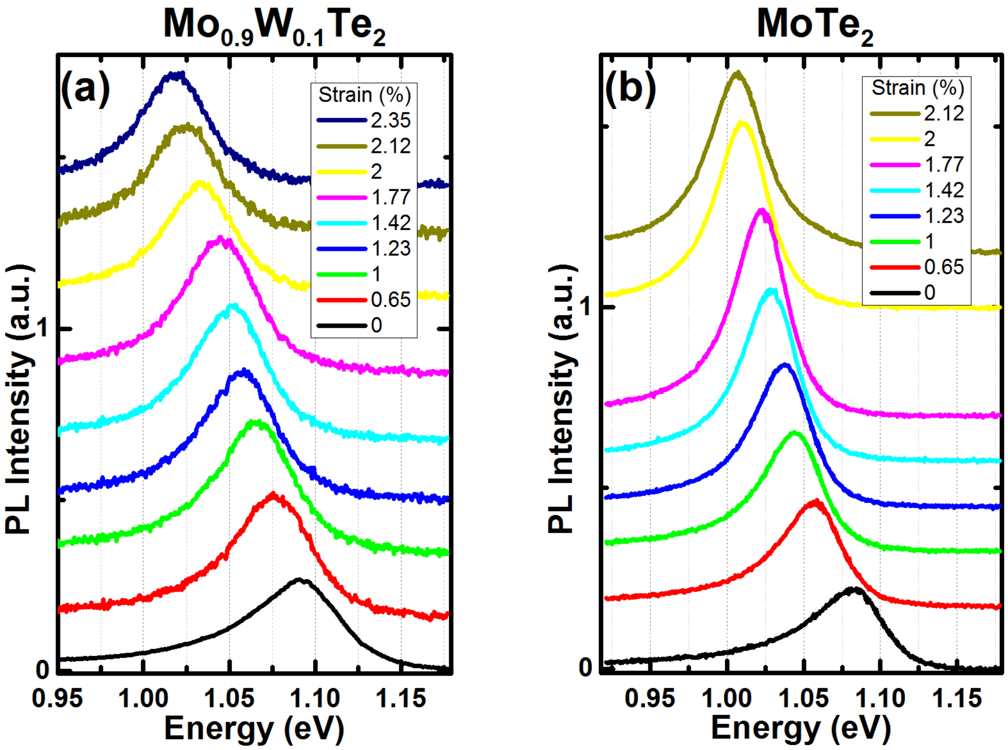

Figure 5-4: Strain-dependent PL spectra of 1L (a) $Mo_{0.9}W_{0.1}Te_2$ and (b) $MoTe_2$ with strain . Laser excitation of 633 nm laser was used. All spectra are vertically offset for clarity.

To gain further insight on the band structures of 1L $MoTe_2$ and $Mo_{0.9}W_{0.1}Te_2$, we perform strain-dependent PL measurements. We first transfer 1L $MoTe_2$ and $Mo_{0.9}W_{0.1}Te_2$ crystals to polyethylene naphthalate (PEN) and clamp them to the substrate using metal strips. We also spin-coat ~100 nm PMMA onto the samples as an additional clamping film. We apply strain to the PEN substrate using a two-point bending apparatus (see Figure A-5). Figure 5-4 shows the PL measurements of 1L $Mo_{0.9}W_{0.1}Te_2$ and $MoTe_2$ as a function of strain. As the applied strain increases, the PL peak redshifts, corresponding to a decrease in the band gap. For $Mo_{0.9}W_{0.1}Te_2$ the PL peak shifts from ~1.09 eV at 0% strain to ~1.02 eV at ~2.35% strain, corresponding to an overall peak shift of about -31 meV/% strain. For $MoTe_2$, the PL peak shifts from ~1.08 eV at 0% strain to ~1.01 eV at ~2.12% strain, which is an overall peak shift of about -33 meV/% strain. The FWHM of the $Mo_{0.9}W_{0.1}Te_2$ and $MoTe_2$ PL peaks decreases from ~63 meV and ~59 meV, respectively, at 0% strain to minimum values of ~49 meV and ~42 meV, respectively. At higher strain, we observe either a PL peak shift to higher energy or a broadening of the peak, which is consistent with slipping of the crystal along the substrate.

To account for the surprising decrease of the FWHM of the PL spectra with strain for both materials, we propose three candidates: 1) the contribution to PL from trions becomes suppressed, 2) the flakes conform better to the flexible substrate (after being transferred), eliminating inhomogeneities, or 3) exciton-phonon scattering is partially suppressed.

We first consider the suppression of trionic PL due to strain. Despite their lowered energy, trions are not expected to contribute much to absorption at room temperature unless the sample is heavily doped.[93,124] This is because the density of states is much higher for excitons than trions and the formation of a trion requires the additional step of binding one quasi-free electron or hole. Thus, the absorption process is mainly governed by excitons. However, trions can still contribute to PL since the relatively long exciton lifetime at the conduction band minimum will allow the formation of trions, which are more stable even at room temperature due to their high binding energy of ~25 meV.[99-100] Therefore, if this effect caused the reduction in the FWHM, we would not see a parallel narrowing in the absorption spectra with strain. However, our measurements showed a similar decrease in the FWHM of the absorption spectra which rules out this candidate (see section 5.5).

Next, we consider the effect 2): We observe that the FWHM of strained 1Ls can go below that of any as-exfoliated ones (Note that Koirala et al. use a different approach to extract the FWHM of 1L $MoTe_2$).[99] Besides, similar measurements on 1L WSe_2 have demonstrated that the strain-induced narrowing of the spectral widths is reversible upon the release of strain.[125] Such an observation shows that the inhomogeneities have not been eliminated with strain as they are not expected to recover. Hence we can conclude that this candidate cannot explain our observations.

Thirdly, we would like to discuss the effect of strain on the exciton-phonon coupling. As we know from the current study and earlier ones, 1Ls of both materials have direct optical gaps. However, we know that the 1L has an indirect transition at a slightly higher energy than the A exciton from band structure calculations and from extrapolating the energy of the indirect gap as compared to that of 2L and thicker crystals.[24-27] Moreover, the energy separation between the minima of indirect (Λ (or another)) and direct (K) valleys, $\Delta E_{\Lambda K}$, at the conduction band will increase with uniaxial as well as biaxial strain in similar material systems.[28,102-103,126-127] However, scattering from the K to Λ requires the absorption of a phonon, which becomes less likely with increasing $\Delta E_{\Lambda K}$. Therefore, we infer from our results that a weakening in the exciton-phonon intervalley scattering is mainly responsible for the decrease in the spectral linewidths.

Here we note an advantage of a strain-dependent study over a temperature-dependent one. Strain affects the lattice which thus affects the band structure without significantly affecting the population of phonons. However, at low temperatures, the phonon population is greatly suppressed, but the lattice is also affected which makes the interpretation of the fundamental properties of the materials difficult. In many cases, it is assumed that the relative energies of different valleys are not affected, which is not always accurate as lowering the temperature has a similar effect to biaxial compressive strain. Therefore, tuning the bands of nearly direct or indirect gap semiconductors via strain will be helpful to gain more insight about their bands and can help interpret the temperature-dependent studies on the spectral linewidths of TMDCs. [99,125,128-129]

Finally, we would like to consider the implications of weaker exciton-phonon scattering for electron transport. There have been calculations on the enhancement of transport properties due to the effect above. [102,130] We propose that this effect should be even larger for $MoTe_2$ as $\Delta E_{\Lambda K}$ is smaller than its sister materials. The same phenomenon was also predicted and has been exploited for high mobility silicon transistors.[131-132]

5.5. Strain-Tuned Absorption and PL on 1L $Mo_{0.9}W_{0.1}Te_2$

We perform strain-dependent absorption and PL measurements on 1L $Mo_{0.9}W_{0.1}Te_2$ to verify that the decrease in the spectral linewidth with strain is visible in the absorption as well as the PL spectra.

We exfoliate the 1L on a PDMS substrate and transfer it onto a PETG substrate at ~40 °C, as described earlier. Next, we perform the aforementioned strain measurements. We have also performed measurements immediately before and after the transfer to ensure that the FWHM of the optical transitions of interest has not been significantly altered during sample preparation. Our sample preparation includes no chemicals to keep the sample intact. All the fabrication and measurements listed above have been completed within 24 hours.

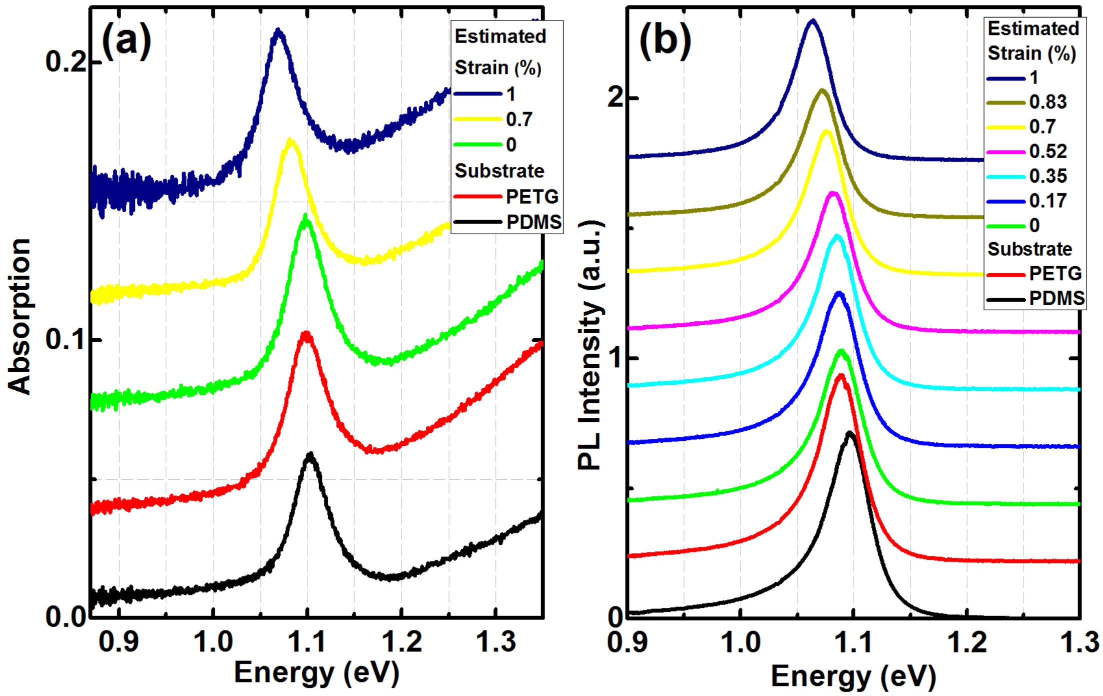

Figure 5-5: Strain-dependent absorption & PL measurements of 1L Mo$_{0.9}$W$_{0.1}$Te$_2$ on PDMS (as-exfoliated, before transferring onto PETG), PETG (after transferred) and with increasing strain.

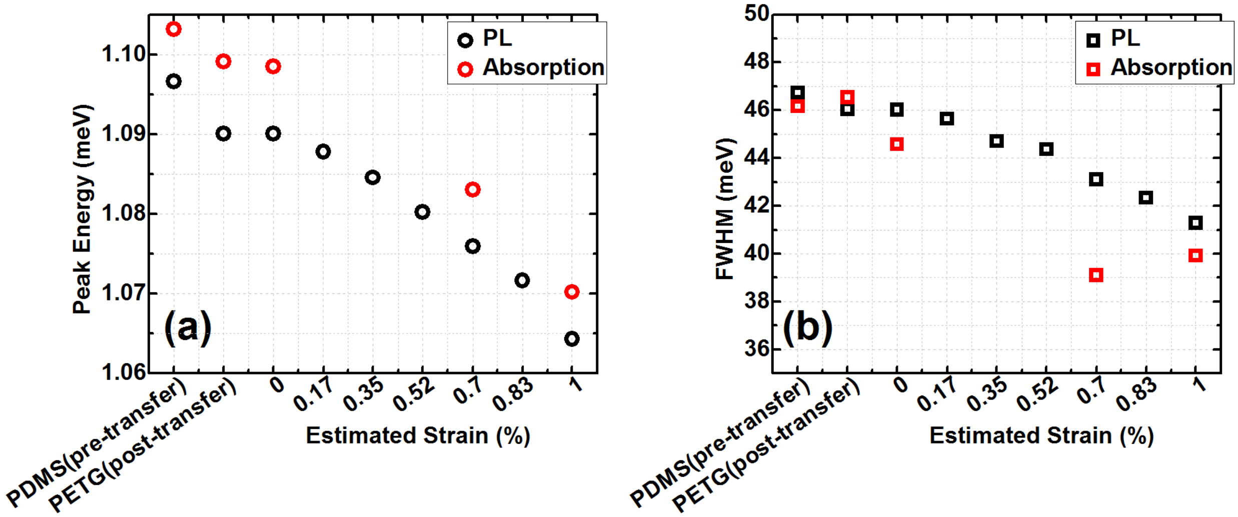

Figure 5-6: Peak energy & FWHM values of absorption and PL spectra shown in Figure 5-5.

Figure 5-5 contains the spectra we obtained. We analyze the spectra and extract the peak positions and the FWHM in the following way: We fit the absorption spectra in the vicinity of the A exciton to two Lorentzians, one for the A exciton and one accounting for the higher energy transitions. For the PL spectra, we look for the energy at which the spectrum is maximized and then obtain the FWHM accordingly. The spectra in Figure 5-5 are vertically offset. Intensities of the measurements on PDMS were adjusted to match the PETG due to their different refractive indices which result in different electric field enhancement on their surfaces.

We present the extracted results in Figure 5-6. We observe that the peak positions in both types of spectra shift to lower values with strain. More importantly, the FWHM decreases in both spectra from ~47 meV down to about 39-40 meV (absorption) and ~41 meV (PL) at the highest strain achieved. As discussed earlier, we infer that the narrowing of the spectral widths is not expected to stem from quenching of the trions.

The strain levels in the measurements shown in Figure 5-5 are estimated after obtaining the shift in peak positions and comparing them to typical shifts with the calculated strain of several other measurements. The accuracy of the estimates does not alter the claims made in this chapter.

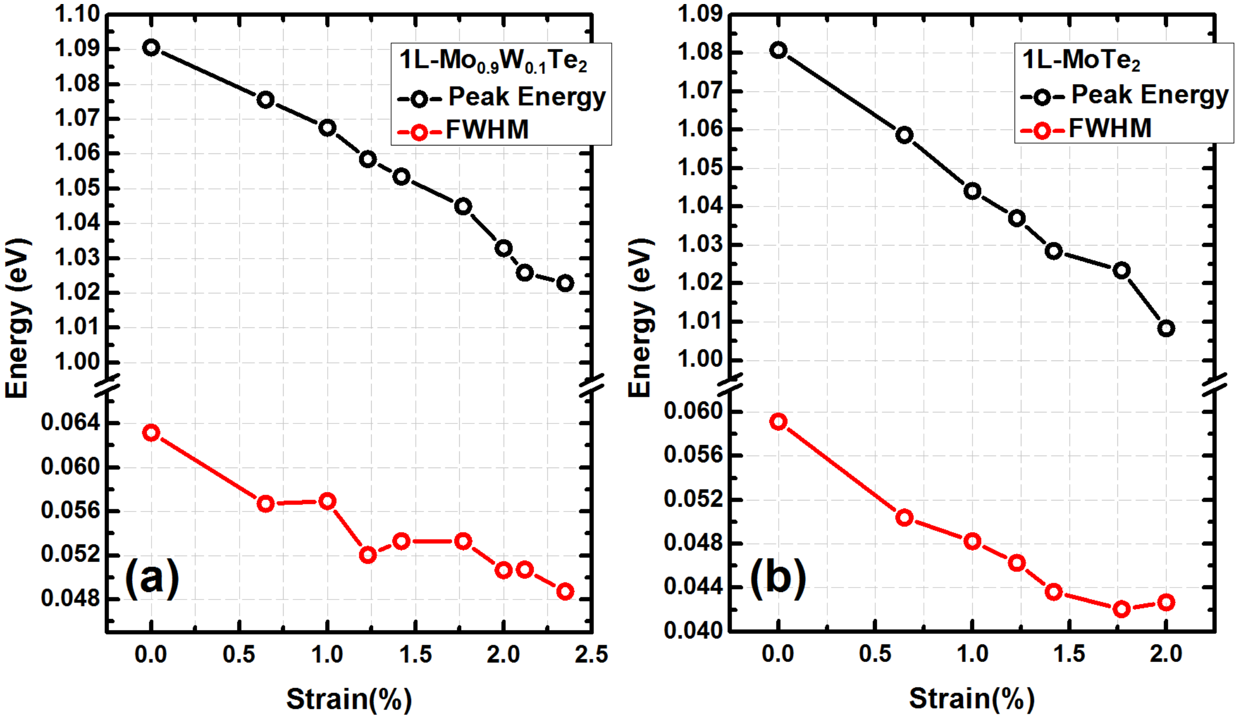

Figure 5-7: Peak energy & FWHM values of the strain-dependent PL spectra of Figure 5-4.

Figure 5-7 shows the peak energy and FWHM values of the strain-dependent PL spectra illustrated in Figure 5-4 which belong to 1L $Mo_{0.9}W_{0.1}Te_2$ and 1L $MoTe_2$.

5.6. **Conclusion**

In conclusion, we have characterized single crystalline ultra-thin $Mo_{0.9}W_{0.1}Te_2$ with PL, absorption and Raman spectroscopy. We have compared its optical properties to those of $MoTe_2$ and have observed that 1L $Mo_{0.9}W_{0.1}Te_2$ possesses a direct band gap at 1.10 eV and the thicker layers become indirect. The additional W changes the band structure, observed via absorption, and can be studied further via Raman spectroscopy using a broader resonant excitation energy range.[133] We have manipulated the band structure of 1L $MoTe_2$ and $Mo_{0.9}W_{0.1}Te_2$ via tensile strain and have thus lowered their band gaps close to 1 eV. We have also observed that the relative energy separation between valleys change and exciton-phonon intervalley scattering can be manipulated. The decrease in the exciton-phonon scattering with strain reduces the spectral linewidth of the A exciton and could also lead to an improvement in transport properties of these materials as well as other TMDCs, encouraging further studies in flexible electronics and optoelectronics.

6. Probing the Anisotropic Light-Matter Interaction in Ultrathin ReS_2

Rhenium disulfide (ReS_2) is a semiconducting and layered group-VII transition metal dichalcogenide with an optical bandgap ~1.4 eV in bulk crystals synthesized by the vapor transport method.[45,134] The layered TMDCs, including MoS_2, $MoSe_2$, WS_2, and WSe_2, have generated significant interest in the research community as stable direct gap semiconductors in the 1L limit with properties tunable by interlayer coupling,[59,81,135] as well as potential for electronic, piezotronic, and optoelectronic applications.[35,70,136-140] Ultrathin ReS_2 has only recently attracted attention with reports of the PL, Raman scattering response, and transconductive properties of ReS_2 which have been measured in the few-layer limit.[45,141]

While these previous investigations were crucial first steps in the thin-film characterization of this material, a critical aspect remains unaddressed: the role of in-plane anisotropy in 1L and few-layer crystals. Strong anisotropy of the optical and electrical properties of ReS_2 has been established for bulk crystals,[39,43-44] and is also expected in thin layers.[46] In fact, a recent report that has demonstrated anisotropy in the electrical properties of few-layer samples.[44] Additionally, the Raman scattering response, while not yet directly characterized, is also expected to be anisotropic based upon studies performed previously on structurally similar $ReSe_2$ and thus to provide a simple optical means of establishing the crystallographic orientation of 1L and few-layer samples.[142]

6.1. Linearly Polarized Excitons in Single- and Few-Layer ReS$_2$ Crystals

ReS$_2$, transition metal dichalcogenide, has been studied by optical spectroscopy. We demonstrate that the reduced crystal symmetry, as compared to the Mo and W dichalcogenides, leads to anisotropic optical properties that persist from the bulk down to the 1L limit. We find that the direct optical gap blueshifts from 1.47 eV in bulk to 1.61 eV in the 1L limit. In the ultrathin limit, we observe polarization-dependent absorption and polarized emission from the band-edge optical transitions. We thus establish ultrathin ReS$_2$ as a birefringent material with strongly polarized direct optical transitions that vary in energy and orientation with sample thickness.

6.1.1. Results and Discussion

In this chapter, we demonstrate the anisotropic optical properties of 1L and few-layer ReS$_2$ crystals through polarization-resolved reflectance and PL spectroscopy. We find that the near-band-edge excitons in ultrathin crystals absorb and emit light with preferred linear polarizations. We also observe that the transition energies of the excitons can be tuned with layer thickness. We thus establish that ultrathin ReS$_2$ has optical transitions with strengths and transition energies that depend on the material thickness and polarization of the optical radiation.

Figure 6-1a is a schematic of the crystal structure of 1L ReS$_2$ from the top and the side view along the *b*-axis.[143,144] Each layer consists of Re atoms sandwiched between two S sheets, with distorted trigonal antiprismatic coordination and strong covalent bonding between the Re and S atoms;[45,144-145] bulk ReS_2 is composed of stacks of such layers held together by weak van der Waals forces. The dashed arrow in Figure 6-1a depicts the location of the inversion center present in 1Ls.[41] Rhenium atoms (red) form a chain due to the Re-Re bonds, which is parallel to the *b*-axis (blue line), as denoted in the literature.[43] Due to that strong metal-metal bond, ReS_2 is expected to break preferentially along the *b*-axis.[146,147] When an ultrathin flake is found to be attached to a thick flake, its *b*-axis can often be identified by its cleavage axis. Figure 6-1b shows a few-layer sample connected to a bulk-like region (indicated by the white arrow) with just such a sharp cleaved edge. This sample was mechanically exfoliated onto a PDMS substrate. The inset in Figure 6-1b presents a profile of the green channel signal (G) of an optical image of the sample. Such data provide a simple means for determining the layer thickness,[148] since each layer increases G by 12-13%. This result was confirmed with the aid of Raman spectroscopy measurements.[147]

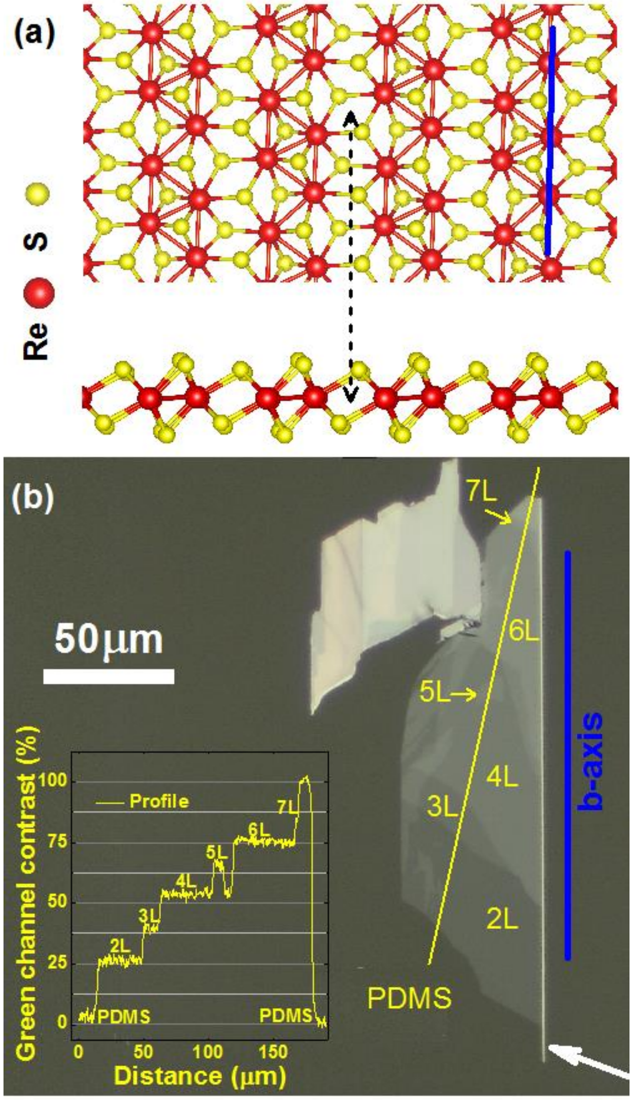

Figure 6-1: Crystal structure of 1L ReS_2 (a) shown from the top (top) and the side (bottom), as viewed along the *b*-axis (blue line). (b) Optical image of a few-layer ReS_2 flake. The inset shows the green channel contrast profile along the yellow line.

We have probed the anisotropic optical response of ReS_2 layers using a combination of unpolarized and polarization-resolved reflection, reflection contrast, and PL measurements. In reflection contrast measurements, we record the differential reflectance of the sample normalized by the reflectance of the substrate, *i.e.*, $\Delta R/R = (R_{ReS_2+PDMS} - R_{PDMS})/R_{PDMS}$, where R_{ReS_2+PDMS} and R_{PDMS} represent, respectively, the reflectance of the thin ReS_2 sample on the PDMS substrate and of the bare PDMS substrate. In the polarization-resolved measurements, a strain-free objective was used to ensure that we illuminated the sample with linearly polarized light and detected the reflected light of the same polarization. For sufficiently small values of the reflection contrast for a sample on a thick transparent substrate, as in our case, we can determine the absorbance $\mathcal{A}$ of the unsupported thin ReS_2 from $\Delta R/R$ as $\mathcal{A} = \frac{1}{4}(n_{PDMS}^2 - 1)(\frac{\Delta R}{R})$,[52-54] where n_{PDMS} denotes the refractive index of PDMS.[105,121] We can thus probe the absorption spectra of sufficiently thin samples through measurements of the reflection contrast. In this fashion, we study the energies and strengths of the direct optical transitions. Indirect transitions are not expected to be observable, since they give rise to a very weak contribution to the absorbance. The lowest-lying transition can generally be identified in the PL spectra, even when it is indirect in character. In polarization-resolved PL measurements, only emitted photons with polarization parallel or perpendicular to the incident laser were collected, and spectra were recorded as the sample was rotated about its surface normal while keeping the collection geometry fixed (see section 6.2.3 for details).

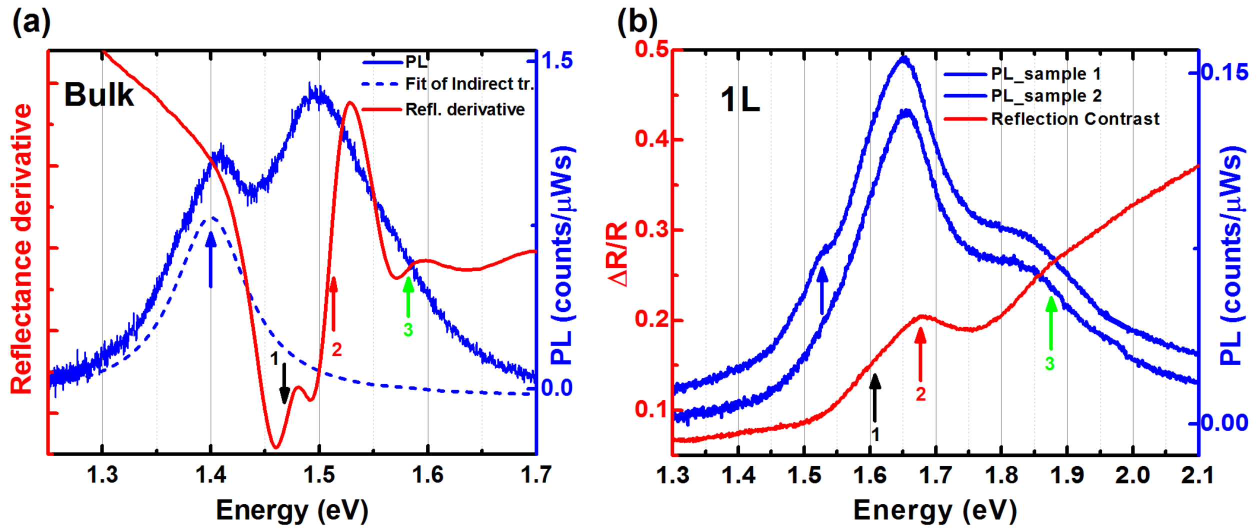

Figure 6-2: Optical spectra of a bulk and 1L ReS_2 crystal (a) Bulk ReS_2 crystal: PL (blue) and reflectance spectra (red), the latter differentiated with respect to photon energy. The dashed blue curve is the contribution to the PL from a transition at 1.40 eV. (b) 1L ReS_2 crystal: PL (blue, upper spectrum offset) and reflection contrast spectrum (red). The arrows indicate the peak positions of the optical transitions.

We first give an overview of the optical response of the 1L and bulk material using measurements with unpolarized radiation. Figure 6-2 displays the unpolarized PL and reflectance spectra for a bulk sample (a) and a 1L (b). In this Figure, the reflectance spectrum of the bulk differentiated with respect to photon energy is plotted to emphasize the optical transitions. For the 1L, we show the reflection contrast spectrum, which, as discussed above, is proportional to the absorption spectrum of the sample. In these spectra (plotted in red in Figure 6-2), we identify three optical transitions. These transitions were previously observed in bulk ReS_2 and exhibited excitonic line shapes. [146,149] We correspondingly refer to them as excitons 1, 2, and 3 and also fit the spectra using Lorentzian contributions. Because exciton 3 is weak, we cannot directly exclude the possibility that this feature arises, for thin layers, from the onset of a band-edge free-carrier transition. However, the increasing strength of excitonic interactions with decreasing layer thickness renders this possibility unlikely, since oscillator strength would be transferred from free-carrier to excitonic transitions. A more probable scenario would be that exciton 3 is an excited (Rydberg) excitonic state of the lower-lying excitons. This result would be compatible with the increasing separation in the energy of exciton 3 from excitons 1 and 2 with decreasing layer thickness. The thinner samples would exhibit increased exciton binding energy and, hence, increased energy separation between the transitions.

In the bulk crystal, these transitions appear at photon energies of 1.47, 1.51 and 1.58 eV, respectively, as identified in the reflectance derivative spectrum by points of inflection. These inferred transition energies agree well with an earlier report[150] of values of 1.48 and 1.52 eV for excitons 1 and 2. In the 1L sample, the features in the reflectance contrast spectra shift to energies of 1.61, 1.68, and 1.88 eV (polarization-resolved measurements discussed below will further clarify these assignments). Figure 6-2 also presents PL data for the bulk sample and the 1L. For the bulk crystal, the PL spectrum exhibits an additional lower-energy peak at 1.40 eV that is not observed in reflectivity spectrum. We highlight this transition, plotted as a dashed blue line, by subtracting the contributions of the optical transitions seen in the reflectivity spectra.

In agreement with the previous studies[42,151] and contrast to a recent report,[45] these data thus suggest that bulk ReS_2 possesses an indirect optical gap at 1.40 eV, lying slightly below the direct optical gap at 1.47 eV identified in the reflectance spectrum. The energy for the indirect-gap transition in this study agrees well with earlier literature values of 1.37±0.02 eV[42] and 1.40 eV[151] for the indirect optical transition. In the 1L, we also observe a similar feature in the PL spectrum (blue arrow in Figure 6-2b) at a lower energy than the direct transitions identified in the reflection contrast spectrum. We have not, however, seen this feature consistently in other 1L samples, *e.g.*, in the second PL spectrum in Figure 6-2b, or spectra for few-layer samples. We are consequently currently unable to identify definitively whether this weak feature arises from an indirect transition or defect states.

Figure 6-2 also shows higher-energy (hot) PL for both bulk and 1L ReS_2 samples. Similar behavior (not shown) is observed in the few-layer samples. Interestingly, PL from exciton 2 (red arrow) is stronger than the PL from lower-energy exciton 1 (black arrow) for all sample thicknesses. This indicates that the emission time from exciton 1 is very short and comparable to the relaxation time of the higher-lying exciton. This behavior, we note, differs from the more typical case seen in the Mo and, W dichalcogenide 1Ls where emission from the lower-energy peak is much stronger than from the higher-energy peak.[59,61,152] For the case of ReS_2, the short emission time for exciton 1 presumably reflects the presence either of a still lower-lying indirect transition or rapid non-radiative relaxation associated with defects. The relative weakness of emission from exciton 1 is also expected based on the lower oscillator strength compared with exciton 2 revealed in the reflection contrast spectrum. Unlike the situation for the Mo and W dichalcogenides,[45] we do not observe increased PL efficiency for 1L samples. There is thus no signature of a transition from an indirect-gap bulk material to a direct-gap semiconductor at 1L thickness. Unfortunately, we do not see a well-defined emission peak below the direct transition identified in the absorption spectra of the 1L and few-layer samples, which would allow us to determine the indirect gap energy. This situation would be expected if the difference between the direct and the indirect transition energies did not greatly exceed the thermal energy, in which case the modestly higher equilibrium population associated with the indirect transition would not compensate for its lower radiative rate. The role of defects in reducing exciton lifetimes may further impede identification of emission from the indirect gap.

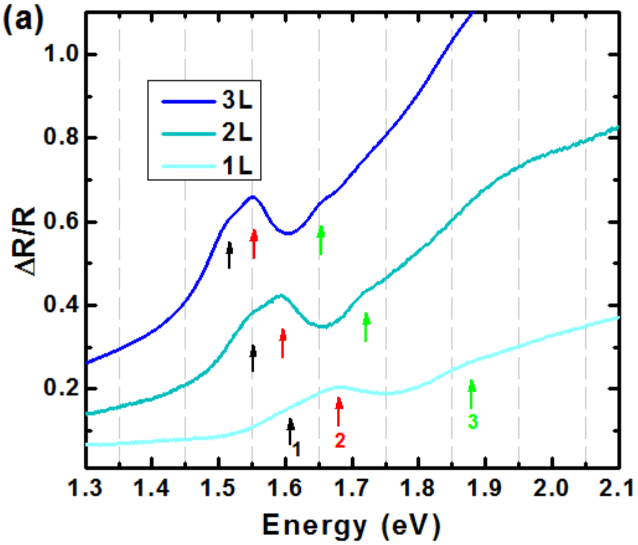

Figure 6-3: ReS_2 reflection contrast spectra for (a) 1L, 2L, 3L ReS_2 crystals based on measurements with unpolarized light. The arrows indicate the peak positions of the optical transitions. (b) Energies of different excitonic transitions extracted from reflection contrast measurements. The energies shift significantly with thickness up to approximately 5L.

To determine the positions of the optical transitions in few-layer ReS_2 crystals, we extend these measurements to thicker samples. Figure 6-3 presents unpolarized reflection contrast spectra for 1L, 2L, and 3L crystals, with transition energies of the excitons 1, 2, and 3 indicated by arrows. Figure 6-3b displays the transition energies for 1L-7L samples and the bulk crystal. To extract the peak positions for 1L-5L samples, we fit each spectrum by one Lorentzian line per peak in the region of interest and one additional Lorentzian feature to represent the contributions of the higher-energy transitions. Because of distortions arising from substrate interference effects, the 6L and 7L samples were analyzed using the energy derivative of the reflection contrast spectra. The data show blueshifts of these three transitions of 140, 160, 300 meV for excitons 1, 2, and 3, respectively, from the bulk to the 1L limit.

The blue shifts in the ReS_2 transition energies with decreasing layer thickness are much greater than those observed for the *direct* transitions (A exciton) in MoS_2 ,[14] $MoSe_2$,[14] $MoTe_2$,[24] WS_2 ,[153] and WSe_2 ,[14] which are, respectively, approximately 30, 15, 20, 50, 60 meV; the blue shifts are, however, smaller than those seen for the *indirect* transitions in the same material systems. Two factors might influence the larger shift observed in ReS_2 compared with the direct transitions in the group-VI transition metal dichalcogenides. The first is stronger electronic coupling in the former than is found at the K-point of the Brillouin zone of the latter, where the direct optical transitions occur. This is consistent with the recent DFT calculations indicating that the direct gap of ReS_2 occurs at the Γ-point of the Brillouin zone.[45-46] A second possible factor would be the influence of a smaller exciton binding energy in ReS_2. The reduced screening of the electron-hole interaction and concomitant increase in binding energy for thinner layers would thus provide less compensation for the expected increase in transition energy from quantum confinement in ReS_2 than for the reference case of the group-VI transition metal dichalcogenides.[153]

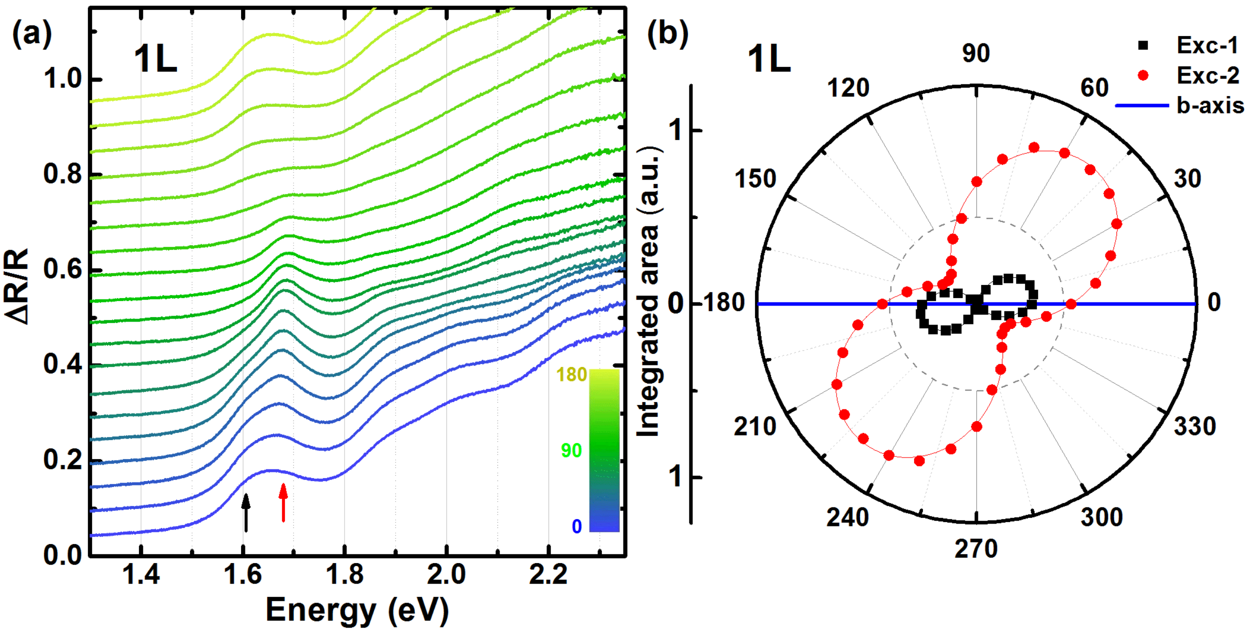

Figure 6-4: Anisotropic optical response of 1L ReS_2. (a) Polarization-resolved reflection contrast spectra, measured at 10° intervals from 0° to 180° and offset for clarity. The arrows indicate the peak positions of the optical transitions. (b) Integrated areas (arbitrary units) of the Lorentzian fits of excitons 1 and 2. The solid lines are fits to the data as discussed in the chapter. The data are presented in a polar plot over a 360° range for clarity.

We now examine the role of anisotropy in the optical response of the ReS_2 layers by measurement of polarization-resolved spectra. Figure 6-4 and Figure 6-7 present such spectra for 1L and 3L samples, respectively. In Figure 6-4a, we see the dependence of the reflection contrast spectra on polarization (or, equivalently, sample) rotation. The data can be described in terms of a variation of the spectral weights of the near-gap excitons with the angle, without any change in their position or width.

Figure 6-4b quantifies this effect by the spectral weight of the first two excitons as a function of light polarization. Both transitions show a double-lobed structure. However, the two excitons do not exhibit the same polarization. The exciton orientation is determined by fitting the weight of the relevant exciton in the polarized reflection contrast data to the form $I_0 + I_1 cos^2(\theta - \theta_{max})$, where I_0, I_1 are constants, θ is the angle of measurement relative to angle at which *b*-axis is parallel to the incident electric field, and θ_{max} is the angle at which the weight is maximized. In the 1L, the absorption from excitons 1 and 2 exhibits a maximum for light polarized, respectively, at ~15° and ~50° from the orientation of the cleaved edge. These measurements have been repeated on other mono- and few-layer ReS_2 crystals. For the few-layer samples similar results have been obtained, but with the polarization of excitons 1 and 2 shifted compared to the 1L. Figure 6-5 displays the angle between the *b*-axis and the electric-field polarization that maximizes the strength of transitions for exciton 1 and 2 as a function of the thickness of the ReS_2 crystal. The bulk data are taken from the literature.[39] For the bulk crystal at a temperature of 110 K, a previous study[39] has shown that excitons 1 and 2 are polarized, respectively, at ~17° and ~86° from the *b*-axis.

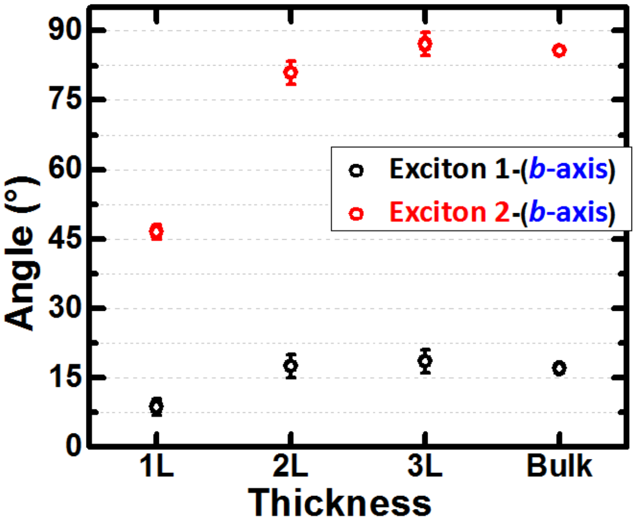

Figure 6-5: Angle between the *b*-axis and excitons 1 and 2 in 1L-3L and bulk ReS_2 (the angle at which the electric field polarization that maximizes the intensities).

The observed polarization dependence of the optical spectra provides a purely non-contact method of determining the crystallographic orientation of the sample. This is of considerable importance given the strong anisotropy in the transport properties of the material, with the *b*-axis exhibiting the highest dc conductivity both in bulk[44] and in 1L samples.[147] We note that the optical anisotropy near the excitonic resonances implies that the absorption of these layers varies strongly as a function of the light polarization. This provides a possible means for near-field control of radiation.

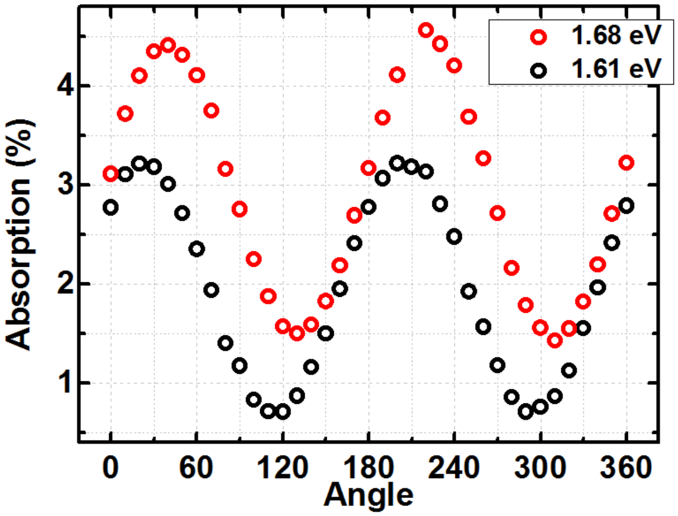

Figure 6-6: Absorption by unsupported 1L ReS_2 of linearly polarized light at photon energies of 1.61 and 1.68 eV as a function of sample orientation with respect to the *b*-axis. The absorption varies from about 0.6% to 3.2%.

Figure 6-6 plots the absorption by 1L ReS_2 of photon energies of 1.61 and 1.68 eV as a function of sample orientation with respect to the *b*-axis. To see how strongly the absorption can be modulated, we chose the photon energies near excitons 1 and 2. To calculate the absorption, we corrected for the effect of the real part of the dielectric function in producing a weak reflection contrast signal. We accordingly subtracted $\Delta R/R(1.40\ eV)$ from $\Delta R/R(1.61\ eV)$ since we expect that there is negligible absorption at 1.40 eV. We then applied the formula mentioned above to determine the absorption of the corresponding free-standing 1L ReS_2. We find that the absorption of 1L ReS_2 at 1.61 eV shows significant contrast with orientation, varying from about 0.6% to 3.2%. This effect could potentially be employed for control of light fields on the nanoscale.

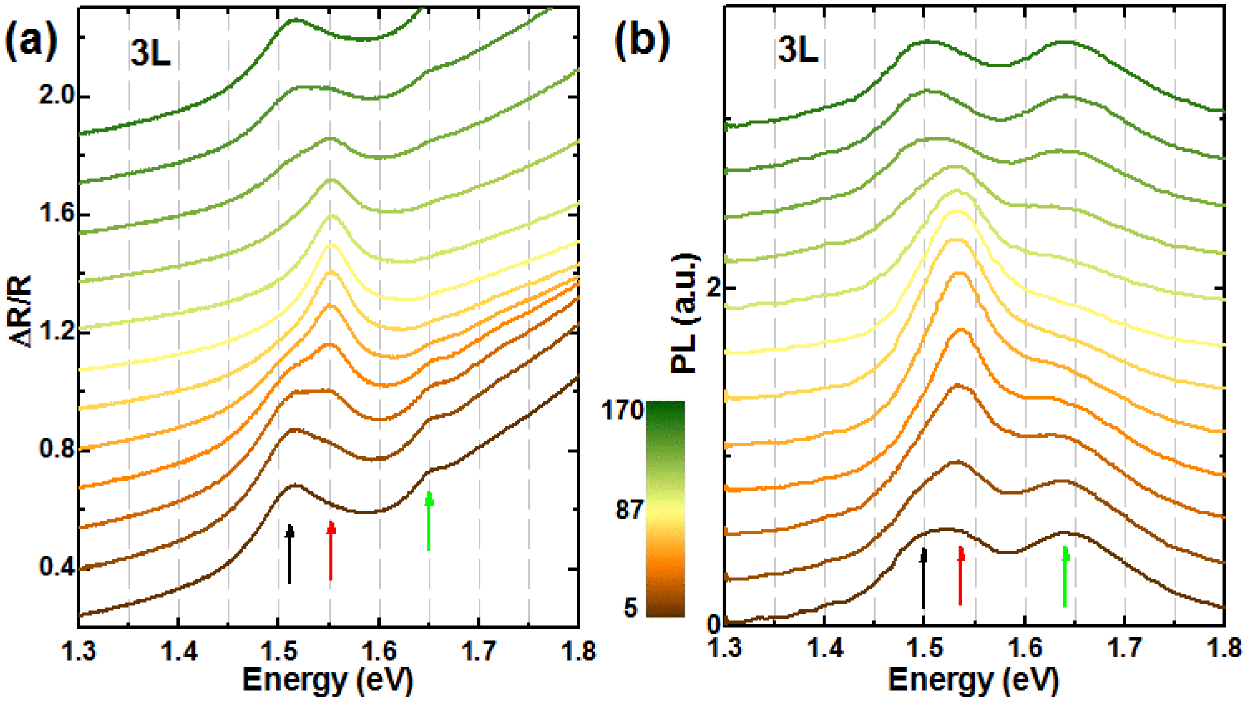

Figure 6-7: Anisotropic optical response of 3L ReS_2. (a) Polarization-resolved reflection contrast spectra measured at 15° intervals from 5° to 170°. (b) Corresponding PL spectra, normalized and, smoothed. The PL is normalized by the maximum intensity in all of the spectra and is smoothed by averaging the data spectrally over a window of ~10 meV. The peaks of the absorption and emission spectra are indicated by black, red, and green arrows. All spectra are offset for clarity.

The general behavior of a sample of 3L thickness is similar to that seen for the 1L. Figure 6-7a shows reflection contrast spectra of 3L samples, which are quite analogous to the spectra for the 1L case in Figure 6-4a. For the 3L sample, we have also measured polarization-resolved PL spectra (Figure 6-7b). The emission spectra further confirm the strongly anisotropic character of the excitonic transitions. A Stokes shift of ~15 meV between the absorption and emission peak energies is inferred from fitting the spectra. The existence of two distinct absorption and emission features with different strengths depending on sample orientation and polarization gives rise to variable optical properties. This might explain the different interpretation of interlayer interactions extracted from the PL peak positions for few-layer and bulk ReS_2 in the recent work by Tongay et al. [45]

6.1.2. Conclusion

In conclusion, we have characterized the optical properties and anisotropy of 1L, few-layer, and bulk ReS_2 crystals. Through PL and reflectance spectroscopy, we confirm the earlier studies on the indirect nature of the bulk material. The direct excitonic transitions are found to shift significantly with decreasing thickness from the bulk to the 1L, unlike those of Mo and W dichalcogenides. Furthermore, the excitons exhibit linearly polarized absorption and emission features, which can be correlated to the sample's crystallographic orientation. From the perspective of optical materials, the robust and highly anisotropic response of ReS_2 could be used for the control of optical fields on the nanoscale. ReS_2 thus provides a new building block for the family of atomically thin 2D semiconductors, stable down to 1L thickness, with strongly anisotropic optical properties.

6.2. In-Plane Anisotropy in Mono- and Few-Layer ReS_2 Probed by Raman Spectroscopy and Scanning Transmission Electron Microscopy

We demonstrate the strong anisotropy in the Raman scattering response by ultrathin ReS_2 for linearly polarized excitation. Polarized Raman scattering is shown to permit a determination of the crystallographic orientation of ReS_2 through comparison with direct structural analysis by scanning transmission electron microscopy (STEM). Analysis of the frequency difference of appropriate Raman modes is also shown to provide a means of precisely determining layer thickness up to four layers.

6.2.1. Results and Discussion

We present a detailed investigation of the Raman scattering in 1L to few-layer ReS_2. Our study demonstrates that, like the previously measured bulk optical and electrical properties, the Raman scattering response is also anisotropic. We show that the anisotropic angle- and polarization-resolved Raman spectra of ReS_2 provide a method for the determination of crystallographic orientation by a purely optical technique, as we confirm using scanning transmission electron microscopy (STEM) to image the crystal lattice. Analysis of the difference in frequency between appropriate Raman modes is also found to provide a means for determining the thickness of a given sample.

In contrast to the more studied group VI metal dichalcogenides like MoS_2 and WSe_2, ReS_2 1Ls exhibit a distorted 1T (1T') structure as the stable phase (see Figure 6-1). Previous studies of bulk ReS_2 have noted that, due to the extra valence electron on the group VII Re atoms, ReS_2 exhibits both metal-chalcogen and metal-metal bonds. The metal-metal bonds are responsible for creating a superlattice structure of Re chains, indicated by a blue line in Figure 6-1. These chains distort the 1L crystal from the more symmetric 1T structure.[41,134,154] Experimentally, crystals synthesized by vapor transport cleave with well-defined edges parallel to the Re chains, typically denoted as the *b*-axis, providing a rapid method of crystal orientation identification convenient for studying the anisotropic optical and electrical properties.[44] While we find exfoliated 1L to few-layer samples that are attached to bulk crystals with well-defined edges, there is often ambiguity as to whether thinner samples also cleave along the *b*-axis, as well as which of the cleaved edges follows the *b*-axis. Moreover, recent progress and the technological demand for producing large-scale samples of TMDC thin films by chemical vapor deposition[155-156] necessitate the development of non-destructive techniques for determining crystal orientation in thin film materials that are independent of the preparation technique.[30,142,157]

We study the anisotropic behavior of thin ReS_2 using angle-resolved polarized Raman spectroscopy, which has been previously utilized in a wide variety of applications including studying strain-induced changes in the electronic structure of graphene,[158] as well as determining the orientation of $ReSe_2$,[142] and black phosphorus crystals.[30,159]

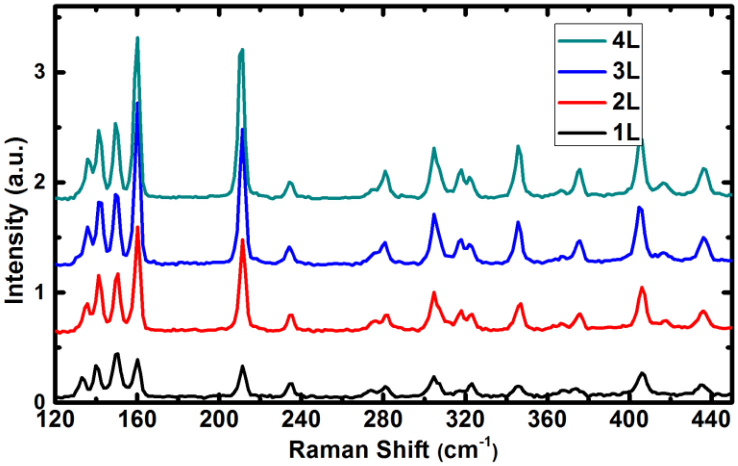

Figure 6-8: Raman spectra of 1L-4L ReS_2

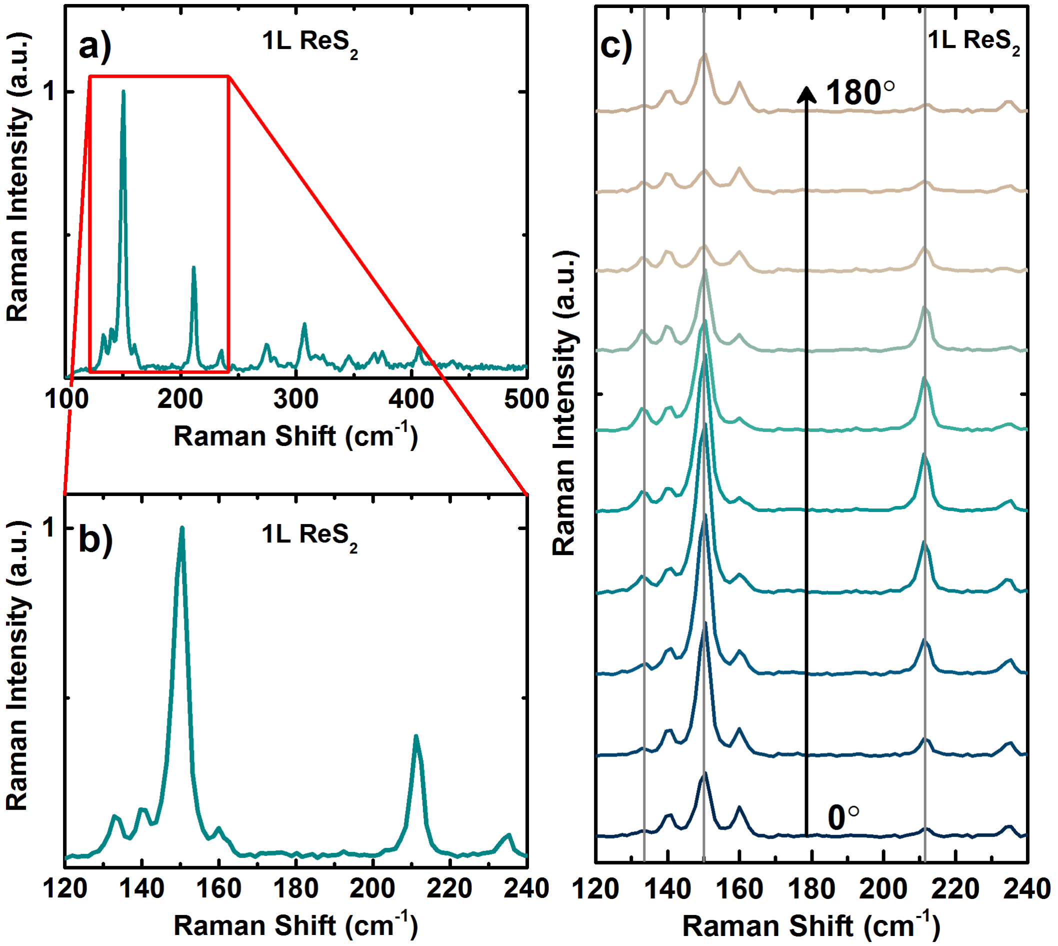

Figure 6-9: Polarization-resolved Raman spectra for 1L ReS_2. Full (a) and detailed (b) view of the spectrum. (c) Unpolarized spectra (offset) as a function of sample orientation angle (taken every 20° by rotating sample about its surface normal).

A previous report on the $ReSe_2$ system, which possesses the same crystal structure, predicted 18 Raman-active vibrational modes.[154] Figure 6-8 plots the unpolarized Raman spectra of 1L-4L ReS_2. We can identify 18 Raman-active vibrational modes.

For the present study, we restrict our attention to the range of Raman shifts between 120 cm^{-1} and 240 cm^{-1}, since the strongest modes occur in this frequency range. Figure 6-9a shows the unpolarized Raman spectrum for a 1L. Figure 6-9c depicts the transformation of the Raman spectrum as the sample is rotated about the surface normal. The intensity of each peak varies strongly with the angle, while the peak positions are unchanged.

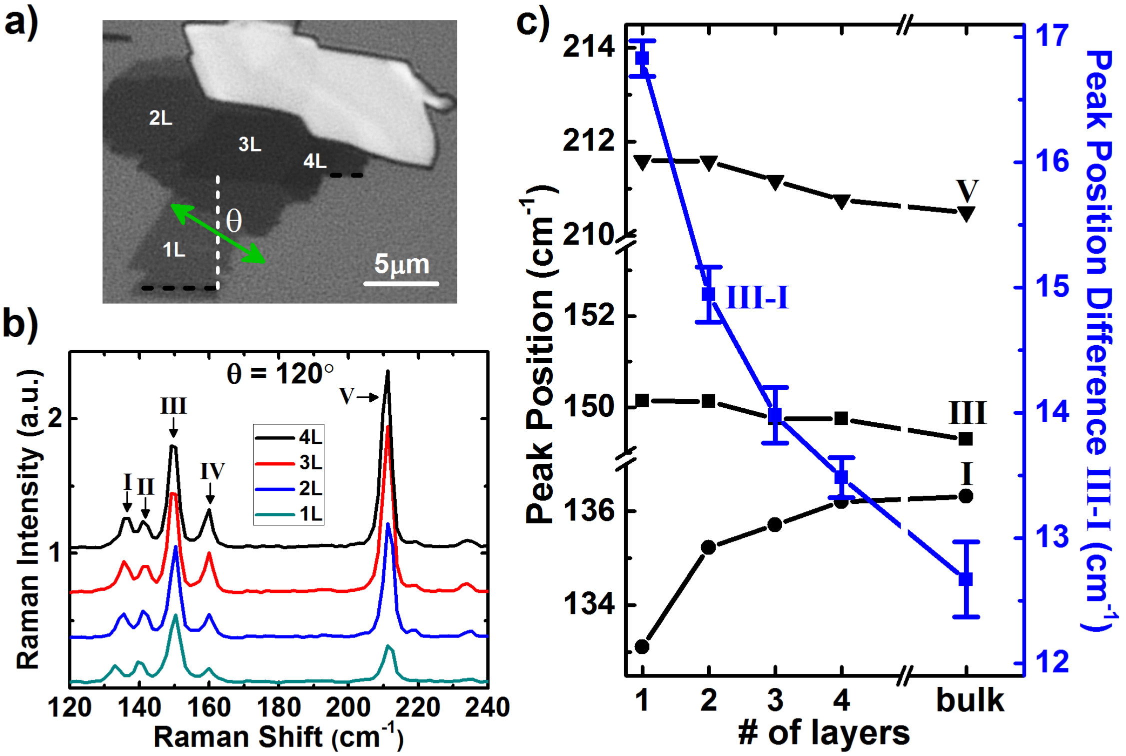

Figure 6-10: Raman spectra of 1L-4L ReS_2 in the range of 120-240 cm^{-1} (a) Optical micrograph of 1L-4L samples. The green double arrow represents the polarization of the 532 nm incident laser. (b) Stacked spectra (θ = 120°). (c) Frequencies for modes I, III, and V and the frequency difference between III and I as a function of thickness.

Before examining the orientation dependence more closely, we study the layer dependence of the unpolarized Raman spectra. Figure 6-10a is a micrograph of a sample containing regions that are 1L-4L thick. A few of the layers cleaved with well-defined edges, as highlighted with black dashed lines. Figure 6-10b shows the Raman spectra for each region at a fixed orientation (θ = 120 degrees). We choose this orientation because all modes of interest are sufficiently strong for further analysis. For simplicity, we label the modes from lowest to highest wavenumber with Roman numerals I through V, with approximate peak positions of 135 cm^{-1}, 141 cm^{-1}, 150 cm^{-1}, 160 cm^{-1}, and 211 cm^{-1}.

This study reveals that it is, in fact, possible to quantify the number of ReS_2 layers by examining the Raman peak positions, as has been shown for other 2D materials.[81] Figure 6-10c displays the peak positions of Raman modes I, III, and V as a function of thickness. The positions of the modes III and V change only marginally from 1L to 4L, as does mode IV (not shown). The position of mode I, on the other hand, varies from 133.1 ± 0.1 cm^{-1} in the 1L to 136.2 ± 0.2 cm^{-1} in the 4L. The weaker mode II shows a similar thickness-dependent tuning. The III-I frequency difference is 16.8 ± 0.2 cm^{-1}, 14.9 ± 0.3 cm^{-1}, 14.0 ± 0.3 cm^{-1}, and 13.5 ± 0.2 cm^{-1} for 1L, 2L, 3L, and 4L, respectively and converges to 12.7 ± 0.3 cm^{-1} in the bulk. (Note: The error bars derive from the difficulty of fitting overlapping Lorentzians.) This result provides a method for identifying the thickness of samples in the few-layer regime like the technique used for MoS_2.[81] Since the peak positions do not shift significantly with polarization angle, these results are robust enough to allow comparison between different samples. Crucially, this analysis requires using an orientation where all of the relevant peaks are sufficiently strong. This can be achieved simply by rotating the sample. We have performed this experiment on numerous samples on different substrates, and the behavior is consistent.

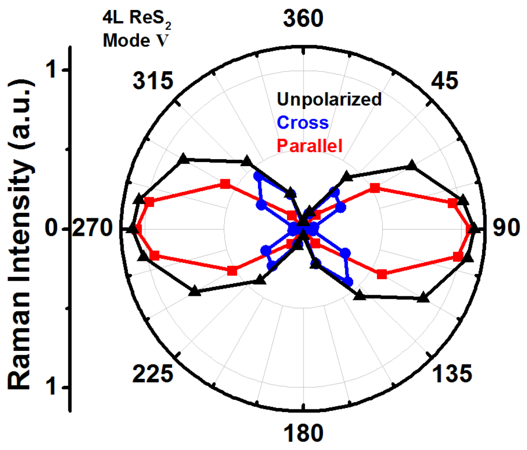

Figure 6-11: Raman intensity of mode V in the 4L region with unpolarized (black), cross-polarized (blue), and parallel-polarized (red) collection.

Figure 6-11 depicts the orientation-dependent polarization response of mode V in the 4L region with cross-polarized (blue) and parallel-polarized (red) collection, as well as an unpolarized (black) collection (with respect to the polarization of the incident laser). The cross- and parallel-polarized spectra yield 4-lobed and 2-lobed shapes, respectively. With this data, it is possible to gain insight into the character of the Raman tensor.[142] For our present purposes of developing a convenient optical method to determine crystallographic orientation; we will concentrate on the parallel polarization data for which the Raman response is significantly stronger.

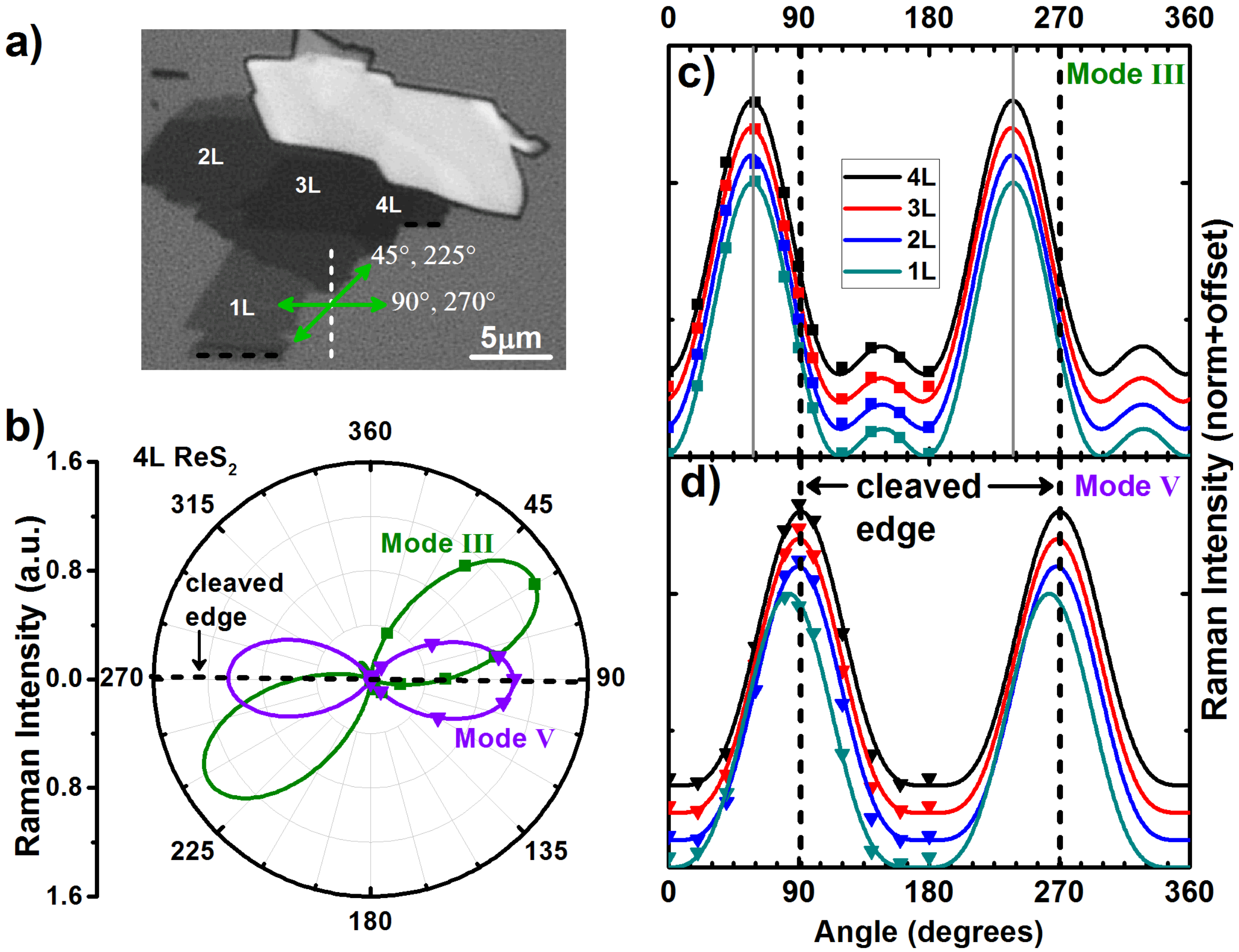

Figure 6-12: Angle-resolved Raman response with parallel collection for modes III, V centered at ~150 cm^{-1} and 211 cm^{-1}, respectively. (a) Optical image of an exfoliated ReS_2 sample. The white dashed line represents the reference sample orientation. (b) Angle-resolved Raman intensities of modes III and V in a 4L ReS_2 presented in a polar plot. Variation with sample orientation of the intensity of mode III (c) and V (d) for 1L-4L thickness. The spectra are normalized and offset. The solid gray lines represent the angle of maximum intensity.

In Figure 6-12, we present the parallel polarization Raman response of modes III (green) and V (violet). Figure 6-12b is a polar plot of the intensity of modes III and V for the 4L region. Mode III exhibits a maximum intensity at an angle of ~58°. Mode V exhibits a maximum intensity at an angle of ~91°, which also happens to be parallel to one of the edges of the exfoliated flake. These two modes were previously calculated in the literature by DFT simulations. Mode III was shown to consist of mostly in-plane vibrations, and mode V was shown to contain out-of-plane vibrations of the sulfur atoms along with in-plane vibrations of the Re atoms in the direction of the *b*-axis.[45] We hypothesize that the angle of maximum intensity for mode V should be in the direction of the *b*-axis.

We examine the consistency of the Raman polarization dependence of each mode as a function of layer thickness. Figure 6-12b depicts the polarization dependence of mode III in the 1L-4L regions. This mode polarization behavior is unchanged for all four different thicknesses, with maximum intensity located at ~58°. Figure 6-12c and d show the thickness dependence of modes III and V. In contrast to mode III, the polarization of mode V varies slightly with thickness, with maximum intensity for this mode at 83° for 1L, 90° for 2L, and 91° for 3L and 4L. This variation may be due to interlayer coupling, substrate interactions or strain induced by the mechanical exfoliation process, the effects of which are expected to diminish in each subsequent layer. The variation in mode V with layer thickness is not reflected in the behavior of mode III, suggesting that mode III is less sensitive to the cause of this variation. Nonetheless, it is clear that mode V displays a maximum intensity when the excitation is roughly parallel to one of the edges of the cleaved crystal. We have observed consistent behavior on more than 20 samples on different substrates including at least four of 1L-3L thickness.

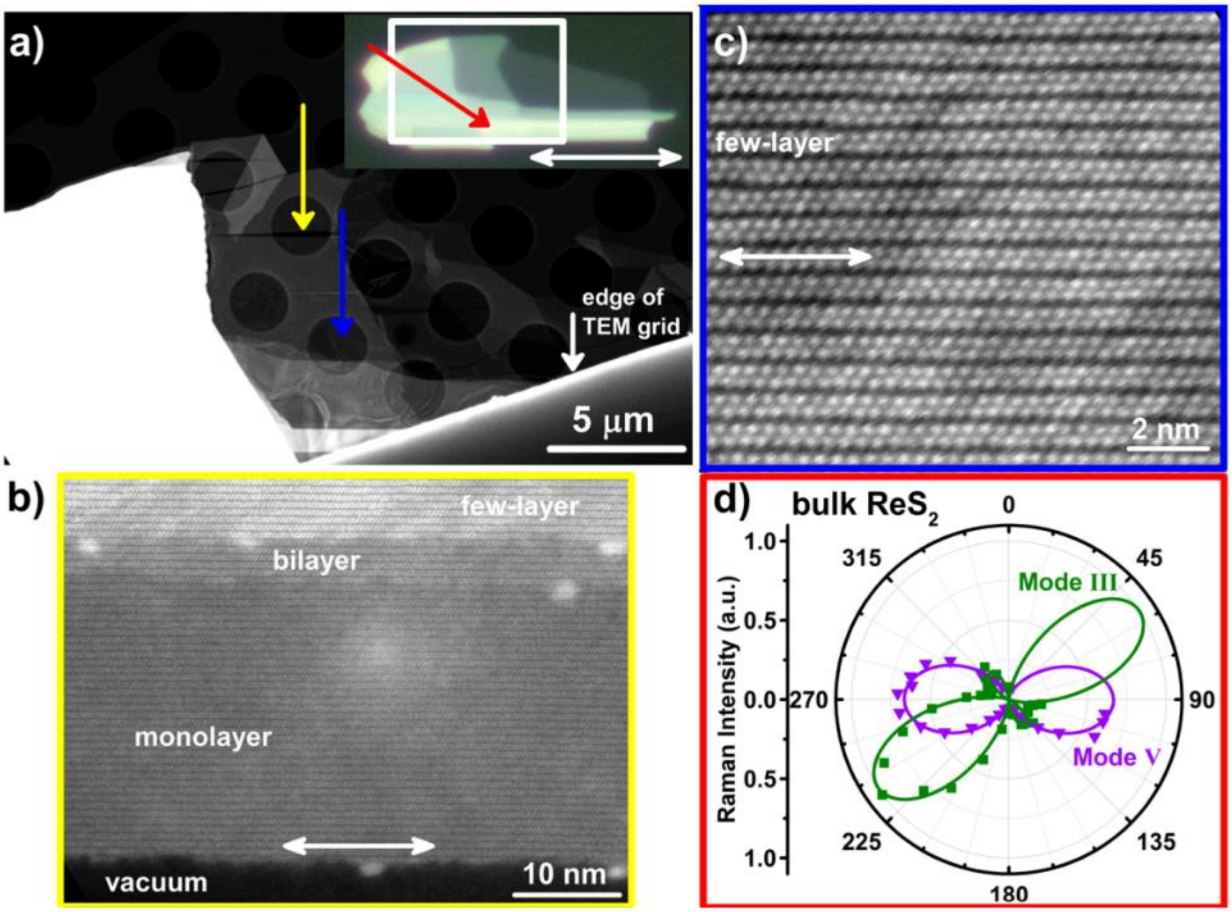

Figure 6-13: Annular dark-field (ADF) STEM of bulk to 1L ReS_2. (a) Low magnification ADF-STEM image of ReS_2 sample on a Quantifoil TEM grid. Inset: optical micrograph of the sample on PDMS before transfer. (b) Medium magnification ADF-STEM image of suspended ReS_2 where the sample tore during the transfer process. (c) High magnification ADF-STEM image of a few-layer region. (d) Polarization- and orientation-resolved Raman spectra of bulk region. White double arrows depict the direction of Re chains in (a)-(c).

In Figure 6-13, we use annular dark-field scanning transmission electron microscopy (ADF-STEM) to image the crystal lattice and confirm that the Raman spectra can be used to determine the crystal orientation. Figure 6-13a shows the low-magnification ADF-STEM image of a ReS_2 sample that was transferred onto a Quantifoil TEM grid. The sample contains regions ranging from bulk to 1L, with some areas that are completely suspended. During the transfer process, some areas tore with well-defined edges, such as the one marked by the yellow arrow. Figure 6-13b shows a higher magnification image of this region and confirms that the *b*-axis (the

Re-Re chain) runs parallel to the cleaved edge. In Figure 6-13c, we present a higher magnification ADF-STEM image taken from the few-layer region marked by the blue arrow. The bright spots represent the Re atoms and the Re chains, which run in a direction ~90° measured clockwise from the vertical, are easily visible. Figure 6-13d depicts the parallel polarization response of the Raman spectra for modes III (green) and V (violet) taken on the bulk region of the sample, as denoted by the red arrow in Figure 6-13a. Mode III is a maximum at an angle of ~55° measured clockwise from the vertical and is denoted by the green line in Figure 6-13c. Mode V is a maximum at an angle of ~91° degrees, which corresponds to the direction parallel to the Re chains.

6.2.2. Conclusion

In conclusion, these results confirm the utility of angle-resolved polarized Raman spectroscopy in determining the crystal orientation in layered TMDCs possessing the distorted 1T structure. These observations and conclusions are supported by atomic-scale imaging with ADF-STEM and will prove invaluable in the future study of the anisotropic optical and electrical properties in thin film ReS_2. ReS_2, however, is only just one of the TMDCs exhibiting the distorted 1T phase to be explored in the few-layer limit, and lessons learned here should serve to inform future experiments in similar material systems.

6.2.3. Methods

Sample Preparation

Large flakes of ReS_2 were deposited from bulk ReS_2 crystals by mechanical exfoliation. The substrate was a thick PDMS film (base: curing agent ratios of 10: 1). The PDMS substrate has negligible optical absorption over the spectral range of interest.[105] The layer thicknesses of the ultrathin ReS_2 crystals were determined by Raman spectroscopy[147] and optical contrast measurements, as discussed above.

Reflection Contrast and PL Measurements

The reflection contrast spectra were obtained with radiation from a tungsten halogen source, in conjunction with a beam splitter and a 50× objective (NA = 0.42). A monochromator dispersed the reflected light from the sample onto a liquid nitrogen cooled Si CCD array.

The equation used for extracting the absorption spectra remains valid while the reflection contrast is less than unity, which is the case even for three layers of ReS_2 because of the comparatively weak optical transitions. The peak positions of those optical transitions are less affected than their magnitude as the absorption spectra slightly deviate from the equation used. Therefore, reflection contrast measurements provide an appropriate approach to finding the peak positions of the optical transitions of few-layer ReS_2 without the need for determining the full complex dielectric function.

The PL measurements were performed using a commercial micro-Raman instrument (Renishaw In-Via) in a backscattering geometry. A linearly polarized laser provided excitation at a wavelength of 532 nm, which was focused by a 100× objective (NA = 0.85) onto the sample. The emitted photons were analyzed in a spectrometer equipped with a grating with 600 lines/mm. The laser power for the PL measurements was approximately 25 µW for the bulk crystal and 300 µW for the ultrathin films. For polarization-resolved PL measurements, we collected emitted photons with a polarization perpendicular to that of the incident laser radiation.

We note that for nominally *unpolarized* measurements, the optical setup might lead to slightly different weightings of the response, but not to a degree to change any conclusions of this chapter.

Raman Measurements

We measure the Raman spectra in a backscattering geometry using a 532 nm laser with a fixed linear polarization. The sample is rotated to an angle θ between the incident polarization and the direction normal to the cleavage plane (depicted by a white dashed line in all subsequent figures). A Silicon CCD measures the scattered light, that a spectrometer disperses with a 2400 l/mm grating onto, using a linear polarizer to independently measure components parallel and perpendicular (cross) to the incident laser polarization. We also study the spectra for unpolarized detection by summing the parallel and perpendicular intensities after correcting for the relative collection efficiency. This provides Raman spectra equivalent to those that would be measured with an ideal, polarization-independent detection system.

All experiments were performed at room temperature.

7. Concluding Remarks

7.1. Conclusion

In conclusion, this dissertation has probed the ultrathin layers of $MoTe_2$ and ReS_2 via strain-tuned and polarization-resolved optical spectroscopy. We have introduced their fundamental optical properties and the experimental tools to study them.

We have seen that their electronic structures transform significantly from bulk down to monolayer limit. Furthermore, we have found the monolayer $MoTe_2$ to be a direct band gap semiconductor with intense PL. We have presented Raman spectra of $MoTe_2$ which vary significantly with crystal thickness due to the changes in the electronic structures and the fact that the ultrathin and bulk crystals belong to different space groups. We have established Raman spectroscopy as a way of determining the thickness of the ultrathin $MoTe_2$. We have demonstrated that tensile strain can significantly reduce the optical gap of monolayer $MoTe_2$ and partially suppress the intervalley exciton-phonon scattering resulting in narrower near-band excitonic transitions.

We have studied the anisotropic light-matter interaction in ultrathin ReS_2 via polarization-resolved optical spectroscopy. We have noted that the near-band-edge excitons shift significantly with decreasing thickness from the bulk to the monolayer, unlike those of Mo and W dichalcogenides. We have found that the excitons exhibit linearly polarized absorption and emission features. We have discovered that polarization-resolved Raman spectroscopy can detect the crystallographic orientation of ReS_2 and we have correlated the anisotropy of the excitons to the sample's crystallographic orientation. Thus, we have established ReS_2 as a new building block in the family of atomically thin semiconductors, stable down to monolayer thickness, with strongly anisotropic optical properties.

Both strain-tuned and polarization-resolved optical spectroscopy have proven to be valuable in understanding the band structures and fundamental optical properties of atomically thin transition metal dichalcogenides.

7.2. **Future Directions**

We would like to present some future directions based on the findings of this dissertation.

Raman modes of ultrathin $MoTe_2$ seem to get enhanced or suppressed by changes not only in the crystal symmetry but also in changes of the electronic structure with layer thickness. Therefore, excitation dependence study of the Raman spectra can discover more about the band structure, phonon dispersion and exciton-phonon coupling of $MoTe_2$ and how these transform with thickness.

We have suggested that tensile strain can reduce exciton-phonon scattering in monolayer $MoTe_2$. Therefore, strain-tuned transport studies can be performed to investigate the same effect and improve the electronic properties of $MoTe_2$ or similar material systems.

Higher tensile strain can be much more informative about the optoelectronic properties. A difficulty in this direction Is that one needs to achieve high strain without chemically affecting the material to clamp it better to the substrate. That way the sole effect of strain can be accurately observed and interpreted.

High tensile strain will strongly reduce the crystal symmetry, and polarization-resolved spectroscopy on strained ultrathin TMDCs can be interesting.

Strain studies at low temperatures can resolve other features such as trions and can examine the effects on them.

7.3. Final Remarks

I want to thank the readers of this dissertation. I hope that this work has been enlightening and inspiring to you.

Graduate school has been a very enjoyable experience and I have learned a lot about the universe outside and the universe within. I realized that there is only so much we can accomplish since more ideas and questions come to mind than a study realizes and answers. We begin to understand how little we know each passing day. The more we learn, the more we realize that there exists, and even more, to do.

"Exalted are You; we have no knowledge except what You have taught us. Indeed, it is You who is All-Knowing, All-Wise."

Bibliography

(1) Puotinen, D.; Newnham, R. E. The Crystal Structure of $MoTe_2$. *Acta Crystallogr.* **1961,** *14*, 691-2.

(2) Frindt, R. F. Optical Properties of Single Crystals of WSe_2 and $MoTe_2$. *J. Phys. Chem. Solids* **1963,** *24*, 1107-12.

(3) Grasso, V.; Saitta, G.; Mondio, G. Optical Constants of $MoTe_2$ from Reflectivity Measurements. *J. Phys. C: Solid St. Phys.* **1972,** *5*, 1101-8.

(4) Davey, B.; Evans, B. L. Optical Properties of $MoTe_2$ and WSe_2. *Phys. Status Solidi A* **1972,** *13*, 483-91.

(5) Sugai, S.; Ueda, T.; Murase, K. Raman-Scattering in MoS_2, $MoSe_2$, and α-$MoTe_2$ at High Pressures. *J. Phys.* **1981,** *42*, 320-2.

(6) Vellinga, M. B.; de Jonge, R.; Haas, C. Semiconductor to metal transition in $MoTe_2$. *J. Solid State Chem.* **1970,** *2*, 299-302.

(7) Champion, J. A. Some Properties of $(Mo,W)(Se,Te)_2$. *Br. J. Appl. Phys.* **1965,** *16*, 1035-7.

(8) Dawson, W. G.; Bullett, D. W. Electronic-Structure and Crystallography of $MoTe_2$ and WTe_2. *J. Phys. C: Solid St. Phys.* **1987,** *20*, 6159-74.

(9) Wieting, T. J.; Grisel, A.; Levy, F. Interlayer Bonding and Localized Charge in $MoSe_2$ and α-$MoTe_2$. *Physica B+C* **1980,** *99*, 337-42.

(10) Reshak, A. H.; Auluck, S. Band structure and optical response of 2H-MoX_2 compounds (X=S, Se, and Te). *Phys. Rev. B* **2005,** *71*.

(11) Boker, T.; Severin, R.; et al. Band structure of MoS_2, $MoSe_2$, and α-$MoTe_2$: Angle-resolved photoelectron spectroscopy and ab initio calculations. *Phys. Rev. B* **2001,** *64*.

(12) Hind, S. P.; Lee, P. M. KKR Calculations of the Energy Bands in $NbSe_2$, MoS_2 and α-$MoTe_2$. *J. Phys. C: Solid St. Phys.* **1980,** *13*, 349-57.

(13) Novoselov, K. S.; Jiang, D.; et al. Two-Dimensional Atomic Crystals. *Proc. Natl. Acad. Sci. U.S.A.* **2005,** *102*, 10451-3.

(14) Li, Y.; Chernikov, A.; et al. Measurement of the optical dielectric function of monolayer transition-metal dichalcogenides: MoS_2, $MoSe_2$, WS_2, and WSe_2. *Phys. Rev. B* **2014,** *90*, 205422.

(15) Chhowalla, M.; Shin, H. S.; et al. The chemistry of two-dimensional layered transition metal dichalcogenide nanosheets. *Nature Chem.* **2013,** *5*, 263-75.

(16) Gillen, R.; Maultzsch, J. Light-Matter Interactions in Two-Dimensional Transition Metal Dichalcogenides: Dominant Excitonic Transitions in Mono- and Few-Layer MoX_2 and Band Nesting. *IEEE J. Sel. Topics Quantum Electron.* **2017,** *23*.

(17) Carvalho, A.; Ribeiro, R. M.; Neto, A. H. C. Band nesting and the optical response of two-dimensional semiconducting transition metal dichalcogenides. *Phys. Rev. B* **2013,** *88*, 115205.

(18) Yun, W. S.; Han, S. W.; et al. Thickness and strain effects on electronic structures of transition metal dichalcogenides: 2H-MX_2 semiconductors (M = Mo, W; X = S, Se, Te). *Phys. Rev. B* **2012,** *85*, 033305.

(19) Duerloo, K. A. N.; Li, Y.; Reed, E. J. Structural phase transitions in two-dimensional Mo- and W-dichalcogenide monolayers. *Nat. Commun.* **2014,** *5*, 4214.

(20) Li, Y.; Duerloo, K. A. N.; et al. Structural semiconductor-to-semimetal phase transition in two-dimensional materials induced by electrostatic gating. *Nat. Commun.* **2016,** *7*, 10671.

(21) Kolobov, A. V.; Fons, P.; Tominaga, J. Electronic excitation-induced semiconductor-to-metal transition in monolayer $MoTe_2$. *Phys. Rev. B* **2016,** *94*.

(22) Rhodes, D.; Chenet, D. A.; et al. Engineering the Structural and Electronic Phases of $MoTe_2$ through W Substitution. *Nano Lett.* **2017,** *17*, 1616-22.

(23) Berry, J.; Zhou, S.; et al. Dynamic Phase Engineering of Bendable Transition Metal Dichalcogenide Monolayers. *Nano Lett.* **2017**.

(24) Ruppert, C.; Aslan, O. B.; Heinz, T. F. Optical Properties and Band Gap of Single- and Few-layer $MoTe_2$ Crystals. *Nano Lett.* **2014,** *14*, 6231-6.

(25) Froehlicher, G.; Lorchat, E.; Berciaud, S. Direct versus indirect band gap emission and exciton-exciton annihilation in atomically thin molybdenum ditelluride ($MoTe_2$). *Phys. Rev. B* **2016,** *94*, 085429.

(26) Lezama, I. G.; Arora, A.; et al. Indirect-to-Direct Band Gap Crossover in Few-Layer $MoTe_2$. *Nano Lett.* **2015,** *15*, 2336-42.

(27) Robert, C.; Picard, R.; et al. Excitonic properties of semiconducting monolayer and bilayer $MoTe_2$. *Phys. Rev. B* **2016,** *94*, 155425.

(28) Rhim, S. H.; Kim, Y. S.; Freeman, A. J. Strain-induced giant second-harmonic generation in monolayered 2H-MoX_2 (X = S, Se, Te). *Appl. Phys. Lett.* **2015,** *107*, 241908.

(29) Oliver, S. M.; Beams, R.; et al. Evolution of Raman spectra in $Mo_{1-x}W_xTe_2$ alloys. *arXiv preprint arXiv:1703.10985* **2017**.

(30) Xia, F. N.; Wang, H.; Jia, Y. C. Rediscovering black phosphorus as an anisotropic layered material for optoelectronics and electronics. *Nat. Commun.* **2014,** *5*, 4458.

(31) Qiao, J. S.; Kong, X. H.; et al. High-mobility transport anisotropy and linear dichroism in few-layer black phosphorus. *Nat. Commun.* **2014,** *5*, 4475.

(32) Tran, V.; Soklaski, R.; et al. Layer-controlled band gap and anisotropic excitons in few-layer black phosphorus. *Phys. Rev. B* **2014,** *89*, 235319.

(33) Liu, H.; Neal, A. T.; et al. Phosphorene: An Unexplored 2D Semiconductor with a High Hole Mobility. *ACS Nano* **2014,** *8*, 4033-41.

(34) Butler, S. Z.; Hollen, S. M.; et al. Progress, Challenges, and Opportunities in Two-Dimensional Materials Beyond Graphene. *ACS Nano* **2013,** *7*, 2898-926.

(35) Mak, K. F.; He, K.; et al. Control of valley polarization in monolayer MoS_2 by optical helicity. *Nat. Nanotech.* **2012,** *7*, 494-8.

(36) Zeng, H.; Dai, J.; et al. Valley polarization in MoS_2 monolayers by optical pumping. *Nat. Nanotech.* **2012,** *7*, 490-3.

(37) Cao, T.; Wang, G.; et al. Valley-selective circular dichroism of monolayer molybdenum disulphide. *Nat. Commun.* **2012,** *3*, 887.

(38) Xiao, D.; Liu, G. B.; et al. Coupled Spin and Valley Physics in Monolayers of MoS_2 and Other Group-VI Dichalcogenides. *Phys. Rev. Lett.* **2012,** *108*, 196802.

(39) Lin, D. Y.; Huang, T. P.; et al. Anisotropy of Photoluminescence in Layered Semiconductors ReS_2 and ReS_2:Au. *Solid State Phenom.* **2011,** *170*, 135-8.

(40) Ho, C. H.; Huang, Y. S.; et al. Absorption-edge anisotropy in ReS_2 and $ReSe_2$ layered semiconductors. *Phys. Rev. B* **1998,** *58*, 16130-5.

(41) Fang, C. M.; Wiegers, G. A.; et al. Electronic structures of ReS_2, $ReSe_2$ and TcS_2 in the real and the hypothetical undistorted structures. *J. Phys. Condens. Matter* **1997,** *9*, 4411-24.

(42) Ho, C. H.; Liao, P. C.; et al. Optical absorption of ReS_2 and $ReSe_2$ single crystals. *J. Appl. Phys.* **1997,** *81*, 6380.

(43) Friemelt, K.; Lux-Steiner, M. C.; Bucher, E. Optical properties of the layered transition-metal-dichalcogenide ReS_2: Anisotropy in the van der Waals plane. *J. Appl. Phys.* **1993,** *74*, 5266.

(44) Ho, C.-H. Dichroic Electro-Optical Behavior of Rhenium Sulfide Layered Crystal. *Cryst. Struct. Theory Appl.* **2013,** *02*, 65-9.

(45) Tongay, S.; Sahin, H.; et al. Monolayer behaviour in bulk ReS_2 due to electronic and vibrational decoupling. *Nat. Commun.* **2014,** *5*, 3252.

(46) Zhong, H. X.; Gao, S. Y.; et al. Quasiparticle band gaps, excitonic effects, and anisotropic optical properties of the monolayer distorted 1T diamond-chain structures ReS_2 and $ReSe_2$. *Phys. Rev. B* **2015,** *92*, 115438.

(47) Bellus, M. Z.; Li, M.; et al. Type-I van der Waals heterostructure formed by MoS_2 and ReS_2 monolayers. *Nanoscale Horiz.* **2017,** *2*, 31-6.

(48) Gutierrez-Lezama, I.; Reddy, B. A.; et al. Electroluminescence from indirect band gap semiconductor ReS_2. *2D Mater.* **2016,** *3*, 045016.

(49) Cui, Q.; Muniz, R. A.; et al. Strong and Anisotropic Third Harmonic Generation in Monolayer and Multilayer ReS_2. *arXiv preprint arXiv:1612.03228* **2016**.

(50) Li, Y. L.; Li, Y. G.; Tang, C. L. Strain engineering and photocatalytic application of single-layer ReS_2. *Int J Hydrogen Energ* **2017,** *42*, 161-7.

(51) Sim, S.; Lee, D.; et al. Selectively tunable optical Stark effect of anisotropic excitons in atomically thin ReS_2. *Nat. Commun.* **2016,** *7*.

(52) Mak, K. F.; Sfeir, M. Y.; et al. Measurement of the Optical Conductivity of Graphene. *Phys. Rev. Lett.* **2008,** *101*, 196405.

(53) Mcintyre, J. D.; Aspnes, D. E. Differential Reflection Spectroscopy of Very Thin Surface Films. *Surf. Sci.* **1971,** *24*, 417-34.

(54) Buckley, R. G.; Beaglehole, D. Absorptance of Thin-Films. *Appl. Opt.* **1977,** *16*, 2495-9.

(55) Pop, E. Energy dissipation and transport in nanoscale devices. *Nano Res.* **2010,** *3*, 147-69.

(56) Zhang, X.; Sun, D. Z.; et al. Measurement of Lateral and Interfacial Thermal Conductivity of Single- and Bilayer MoS_2 and $MoSe_2$ Using Refined Optothermal Raman Technique. *ACS Appl. Mater. Interfaces* **2015,** *7*, 25923-9.

(57) Cai, W.; Moore, A. L.; et al. Thermal transport in suspended and supported monolayer graphene grown by chemical vapor deposition. *Nano Lett.* **2010,** *10*, 1645-51.

(58) Zhang, W. J.; Huang, J. K.; et al. High-Gain Phototransistors Based on a CVD MoS_2 Monolayer. *Adv. Mater.* **2013,** *25*, 3456-61.

(59) Mak, K. F.; Lee, C.; et al. Atomically Thin MoS_2: A New Direct-Gap Semiconductor. *Phys. Rev. Lett.* **2010,** *105*, 136805.

(60) Splendiani, A.; Sun, L.; et al. Emerging photoluminescence in monolayer MoS_2. *Nano Lett.* **2010,** *10*, 1271-5.

(61) Zhao, W.; Ghorannevis, Z.; et al. Evolution of Electronic Structure in Atomically Thin Sheets of WS_2 and WSe_2. *ACS Nano* **2013,** *7*, 791-7.

(62) Xu, X.; Yao, W.; et al. Spin and pseudospins in layered transition metal dichalcogenides. *Nat. Phys.* **2014,** *10*, 343-50.

(63) Zhang, Y.; Chang, T. R.; et al. Direct observation of the transition from indirect to direct bandgap in atomically thin epitaxial $MoSe_2$. *Nat. Nanotech.* **2014,** *9*, 111-5.

(64) Tongay, S.; Zhou, J.; et al. Thermally driven crossover from indirect toward direct bandgap in 2D semiconductors: $MoSe_2$ versus MoS_2. *Nano Lett.* **2012,** *12*, 5576-80.

(65) Komsa, H.-P.; Krasheninnikov, A. V. Two-Dimensional Transition Metal Dichalcogenide Alloys: Stability and Electronic Properties. *J. Phys. Chem. Lett.* **2012,** *3*, 3652-6.

(66) Liu, H.; Antwi, K. K.; et al. Vapor-phase growth and characterization of $Mo_{(1-x)}W_{(x)}S_2$ (0 </= x </= 1) atomic layers on 2-inch sapphire substrates. *Nanoscale* **2014,** *6*, 624-9.

(67) Mann, J.; Ma, Q.; et al. 2-dimensional transition metal dichalcogenides with tunable direct band gaps: $MoS_{(2)((1)-x)}Se_{(2)x}$ monolayers. *Adv. Mater.* **2014,** *26*, 1399-404.

(68) Feng, Q.; Zhu, Y.; et al. Growth of large-area 2D $MoS_{(2)((1)-x)}Se_{(2)x}$ semiconductor alloys. *Adv. Mater.* **2014,** *26*, 2648-53, 13.

(69) He, K.; Poole, C.; et al. Experimental Demonstration of Continuous Electronic Structure Tuning via Strain in Atomically Thin MoS_2. *Nano Lett.* **2013,** *13*, 2931-6.

(70) Conley, H. J.; Wang, B.; et al. Bandgap Engineering of Strained Monolayer and Bilayer MoS_2. *Nano Lett.* **2013,** *13*, 3626-30.

(71) Hui, Y. Y.; Liu, X. F.; et al. Exceptional Tunability of Band Energy in a Compressively Strained Trilayer MoS_2 Sheet. *ACS Nano* **2013,** *7*, 7126-31.

(72) Lu, N.; Guo, H.; et al. MoS_2/MX_2 heterobilayers: bandgap engineering via tensile strain or external electrical field. *Nanoscale* **2014,** *6*, 2879-86.

(73) Komsa, H.-P.; Krasheninnikov, A. V. Electronic structures and optical properties of realistic transition metal dichalcogenide heterostructures from first principles. *Phys. Rev. B* **2013,** *88*, 085318.

(74) Grant, A. J.; Griffiths, T. M.; et al. Electrical Properties and Magnitude of Indirect Gap in Semiconducting Transition-Metal Dichalcogenide Layer Crystals. *J. Phys. C: Solid St. Phys.* **1975,** *8*, L17-L23.

(75) Conan, A.; Bonnet, A.; et al. Dependence of the Total Mobility in a One-Band Model Application to n-Type $MoTe_2$. *Phys. Status Solidi B* **1984,** *124*, 403-10.

(76) Yamamoto, M.; Wang, S. T.; et al. Strong Enhancement of Raman Scattering from a Bulk-Inactive Vibrational Mode in Few-Layer $MoTe_2$. *ACS Nano* **2014,** *8*, 3895-903.

(77) Zhang, W. X.; Huang, Z. S.; et al. Two-dimensional semiconductors with possible high room temperature mobility. *Nano Res.* **2014,** *7*, 1731-7.

(78) Lin, Y. F.; Xu, Y.; et al. Ambipolar $MoTe_2$ transistors and their applications in logic circuits. *Adv. Mater.* **2014,** *26*, 3263-9.

(79) Pradhan, N. R.; Rhodes, D.; et al. Field-Effect Transistors Based on Few-Layered α-$MoTe_2$. *ACS Nano* **2014,** *8*, 5911-20.

(80) Nemes-Incze, P.; Osváth, Z.; et al. Anomalies in thickness measurements of graphene and few layer graphite crystals by tapping mode atomic force microscopy. *Carbon* **2008,** *46*, 1435-42.

(81) Lee, C.; Yan, H.; et al. Anomalous Lattice Vibrations of Single- and Few-Layer MoS_2. *ACS Nano* **2010,** *4*, 2695-700.

(82) Ghosh, G. Dispersion-equation coefficients for the refractive index and birefringence of calcite and quartz crystals. *Opt. Commun.* **1999,** *163*, 95-102.

(83) Wilson, J. A.; Yoffe, A. D. The transition metal dichalcogenides discussion and interpretation of the observed optical, electrical and structural properties. *Adv. Phys.* **1969,** *18*, 193-335.

(84) Beal, A. R.; Liang, W. Y.; Knights, J. C. Transmission spectra of some transition metal dichalcogenides: II. Group VIA: trigonal prismatic coordination. *J. Phys. C: Solid State Phys.* **1972,** *5*, 3540.

(85) Jin, W. C.; Yeh, P. C.; et al. Direct Measurement of the Thickness-Dependent Electronic Band Structure of MoS_2 Using Angle-Resolved Photoemission Spectroscopy. *Phys. Rev. Lett.* **2013,** *111*, 106801.

(86) Bromley, R. A. M., R. B.; Yoffe, A. D The band structures of some transition metal dichalcogenides. III. Group VIA: trigonal prism materials. *J. Phys. C: Solid State Phys.* **1972,** *5*, 759.

(87) Qiu, D. Y.; da Jornada, F. H.; Louie, S. G. Optical Spectrum of MoS_2: Many-Body Effects and Diversity of Exciton States. *Phys. Rev. Lett.* **2013,** *111*, 216805.

(88) Zhu, Z. Y.; Cheng, Y. C.; Schwingenschlögl, U. Giant spin-orbit-induced spin splitting in two-dimensional transition-metal dichalcogenide semiconductors. *Phys. Rev. B* **2011,** *84*.

(89) Ramasubramaniam, A. Large excitonic effects in monolayers of molybdenum and tungsten dichalcogenides. *Phys. Rev. B* **2012,** *86*, 115409.

(90) Zeng, H. L.; Liu, G. B.; et al. Optical signature of symmetry variations and spin-valley coupling in atomically thin tungsten dichalcogenides. *Sci. Rep.* **2013,** *3*.

(91) Kumar, A.; Ahluwalia, P. K. Electronic structure of transition metal dichalcogenides monolayers 1H-MX_2 (M = Mo, W; X = S, Se, Te) from ab-initio theory: new direct band gap semiconductors. *Eur. Phys. J. B* **2012,** *85*, 186.

(92) Li, S. L.; Miyazaki, H.; et al. Quantitative Raman Spectrum and Reliable Thickness Identification for Atomic Layers on Insulating Substrates. *ACS Nano* **2012,** *6*, 7381-8.

(93) Mak, K. F.; He, K.; et al. Tightly bound trions in monolayer MoS_2. *Nat. Mater.* **2013,** *12*, 207-11.

(94) Newaz, A. K. M.; Prasai, D.; et al. Electrical control of optical properties of monolayer MoS_2. *Solid State Commun.* **2013,** *155*, 49-52.

(95) Luo, X.; Zhao, Y.; et al. Effects of lower symmetry and dimensionality on Raman spectra in two-dimensional WSe_2. *Phys. Rev. B* **2013,** *88*, 195313.

(96) Golasa, K.; Grzeszczyk, M.; et al. Multiphonon resonant Raman scattering in MoS_2. *Appl. Phys. Lett.* **2014,** *104*.

(97) Berkdemir, A.; Gutiérrez, H. R.; et al. Identification of individual and few layers of WS_2 using Raman Spectroscopy. *Sci. Rep.* **2013,** *3*.

(98) Terrones, H.; Corro, E. D.; et al. New First Order Raman-Active Modes in Few Layered Transition Metal Dichalcogenides. *Sci. Rep.* **2014,** *4*, 4215.

(99) Koirala, S.; Mouri, S.; et al. Homogeneous linewidth broadening and exciton dephasing mechanism in $MoTe_2$. *Phys. Rev. B* **2016,** *93*, 075411.

(100) Yang, J.; Lu, T. Y.; et al. Robust Excitons and Trions in Monolayer $MoTe_2$. *ACS Nano* **2015,** *9*, 6603-9.

(101) Duerloo, K. A. N.; Reed, E. J. Structural Phase Transitions by Design in Monolayer Alloys. *ACS Nano* **2016,** *10*, 289-97.

(102) Hosseini, M.; Elahi, M.; et al. Very large strain gauges based on single layer $MoSe_2$ and WSe_2 for sensing applications. *Appl. Phys. Lett.* **2015,** *107*, 253503.

(103) Villegas, C. E. P.; Rocha, A. R. Elucidating the Optical Properties of Novel Heterolayered Materials Based on $MoTe_2$-InN for Photovoltaic Applications. *J. Phys. Chem. C* **2015,** *119*, 11886-95.

(104) Song, S.; Keum, D. H.; et al. Room Temperature Semiconductor-Metal Transition of $MoTe_2$ Thin Films Engineered by Strain. *Nano Lett.* **2016,** *16*, 188-93.

(105) Cai, D. K.; Neyer, A.; et al. Optical absorption in transparent PDMS materials applied for multimode waveguides fabrication. *Opt. Mater.* **2008,** *30*, 1157-61.

(106) Liu, Z.; Amani, M.; et al. Strain and structure heterogeneity in MoS_2 atomic layers grown by chemical vapour deposition. *Nat. Commun.* **2014,** *5*, 5246.

(107) Jiang, T.; Huang, R.; Zhu, Y. Interfacial Sliding and Buckling of Monolayer Graphene on a Stretchable Substrate. *Adv. Funct. Mater.* **2014,** *24*, 396-402.

(108) Scheuschner, N.; Gillen, R.; et al. Interlayer resonant Raman modes in few-layer MoS_2. *Phys. Rev. B* **2015,** *91*, 235409.

(109) Guo, H. H.; Yang, T.; et al. Double resonance Raman modes in monolayer and few-layer $MoTe_2$. *Phys. Rev. B* **2015,** *91*, 205415.

(110) Song, Q. J.; Tan, Q. H.; et al. Physical origin of Davydov splitting and resonant Raman spectroscopy of Davydov components in multilayer $MoTe_2$. *Phys. Rev. B* **2016,** *93*, 115409.

(111) Gołasa, K.; Grzeszczyk, M.; et al. Resonant quenching of Raman scattering due to out-of-plane A_{1g}/A'_1 modes in few-layer $MoTe_2$. *arXiv preprint arXiv:1608.04087* **2016**.

(112) Grzeszczyk, M.; Golasa, K.; et al. Raman scattering of few-layers $MoTe_2$. *2D Mater.* **2016,** *3*, 025010.

(113) Qiao, X.-F.; Li, X.-L.; et al. Substrate-free layer-number identification of two-dimensional materials: A case of $Mo_{0.5}W_{0.5}S_2$ alloy. *Appl. Phys. Lett.* **2015,** *106*, 223102.

(114) Wei-Jhih, S.; Wei-Qian, W.; et al. $Mo_{1-x}W_xS_2$-based photodetector fabrication and photoconductive characteristics. *Jpn. J. Appl. Phys.* **2017,** *56*, 032201.

(115) Zhang, M.; Wu, J.; et al. Two-Dimensional Molybdenum Tungsten Diselenide Alloys: Photoluminescence, Raman Scattering, and Electrical Transport. *ACS Nano* **2014,** *8*, 7130-7.

(116) Chen, Y.; Dumcenco, D. O.; et al. Composition-dependent Raman modes of $Mo_{1-x}W_xS_2$ monolayer alloys. *Nanoscale* **2014,** *6*, 2833-9.

(117) Landau, L. D.; Lifshitz, E. M., *Mechanics*. 2nd ed.; Pergamon: Bristol, UK, 1969.

(118) Huang, L.-F.; Zeng, Z. Roles of Mass, Structure, and Bond Strength in the Phonon Properties and Lattice Anharmonicity of Single-Layer Mo and W Dichalcogenides. *J. Phys. Chem. C* **2015,** *119*, 18779-89.

(119) Froehlicher, G.; Lorchat, E.; et al. Unified Description of the Optical Phonon Modes in N-Layer $MoTe_2$. *Nano Lett.* **2015,** *15*, 6481-9.

(120) Soubelet, P.; Bruchhausen, A. E.; et al. Resonance effects in the Raman scattering of monolayer and few-layer $MoSe_2$. *Phys. Rev. B* **2016,** *93*, 155407.

(121) Cai, Z.; Qiu, W.; et al. A new fabrication method for all-PDMS waveguides. *Sens. Actuators. A Phys.* **2013,** *204*, 44-7.

(122) Liu, G. B.; Shan, W. Y.; et al. Three-band tight-binding model for monolayers of group-VIB transition metal dichalcogenides. *Phys. Rev. B* **2013,** *88*, 085433.

(123) Rigosi, A. F.; Hill, H. M.; et al. Electronic band gaps and exciton binding energies in monolayer $Mo_xW_{1-x}S_2$ transition metal dichalcogenide alloys probed by scanning tunneling and optical spectroscopy. *Phys. Rev. B* **2016,** *94*, 075440.

(124) Chernikov, A.; van der Zande, A. M.; et al. Electrical Tuning of Exciton Binding Energies in Monolayer WS_2. *Phys. Rev. Lett.* **2015,** *115*, 126802.

(125) Schmidt, R.; Niehues, I.; et al. Reversible uniaxial strain tuning in atomically thin WSe_2. *2D Mater.* **2016,** *3*, 021011.

(126) Chang, C. H.; Fan, X. F.; et al. Orbital analysis of electronic structure and phonon dispersion in MoS_2, $MoSe_2$, WS_2, and WSe_2 monolayers under strain. *Phys. Rev. B* **2013,** *88*, 195420.

(127) Shi, H. L.; Pan, H.; et al. Quasiparticle band structures and optical properties of strained monolayer MoS_2 and WS_2. *Phys. Rev. B* **2013,** *87*, 155304.

(128) Selig, M.; Berghauser, G.; et al. Excitonic linewidth and coherence lifetime in monolayer transition metal dichalcogenides. *Nat. Commun.* **2016,** *7*, 13279.

(129) Zhang, C. D.; Chen, Y. X.; et al. Probing Critical Point Energies of Transition Metal Dichalcogenides: Surprising Indirect Gap of Single Layer WSe_2. *Nano Lett.* **2015,** *15*, 6494-500.

(130) Ge, Y. F.; Wan, W. H.; et al. Effect of doping and strain modulations on electron transport in monolayer MoS_2. *Phys. Rev. B* **2014,** *90*, 035414.

(131) Takagi, S. I.; Hoyt, J. L.; et al. Comparative study of phonon-limited mobility of two-dimensional electrons in strained and unstrained Si metal-oxide-semiconductor field-effect transistors. *J. Appl. Phys.* **1996,** *80*, 1567-77.

(132) Mazure, C.; Cayrefourcq, I. Status of device mobility enhancement through strained silicon engineering. *2005 IEEE International SOI Conference, Proceedings* **2005**, 1-6.

(133) del Corro, E.; Terrones, H.; et al. Excited Excitonic States in 1L, 2L, 3L, and Bulk WSe_2 Observed by Resonant Raman Spectroscopy. *ACS Nano* **2014,** *8*, 9629-35.

(134) Ho, C. H.; Huang, C. E. Optical property of the near band-edge transitions in rhenium disulfide and diselenide. *J. Alloy. Compd.* **2004,** *383*, 74-9.

(135) van der Zande, A. M.; Kunstrnann, J.; et al. Tailoring the Electronic Structure in Bilayer Molybdenum Disulfide via Interlayer Twist. *Nano Lett.* **2014,** *14*, 3869-75.

(136) Lee, G. H.; Yu, Y. J.; et al. Flexible and Transparent MoS_2 Field-Effect Transistors on Hexagonal Boron Nitride-Graphene Heterostructures. *ACS Nano* **2013,** *7*, 7931-6.

(137) Wu, W. Z.; Wang, L.; et al. Piezoelectricity of single-atomic-layer MoS_2 for energy conversion and piezotronics. *Nature* **2014,** *514*, 470-4.

(138) Suzuki, R.; Sakano, M.; et al. Valley-dependent spin polarization in bulk MoS_2 with broken inversion symmetry. *Nat. Nanotech.* **2014,** *9*, 611-7.

(139) Ross, J. S.; Klement, P.; et al. Electrically tunable excitonic light-emitting diodes based on monolayer WSe_2 p-n junctions. *Nat. Nanotech.* **2014,** *9*, 268-72.

(140) Jones, A. M.; Yu, H. Y.; et al. Optical generation of excitonic valley coherence in monolayer WSe_2. *Nat. Nanotech.* **2013,** *8*, 634-8.

(141) Corbett, C. M.; McClellan, C.; et al. Field Effect Transistors with Current Saturation and Voltage Gain in Ultrathin ReS_2. *ACS Nano* **2015,** *9*, 363-70.

(142) Wolverson, D.; Crampin, S.; et al. Raman Spectra of Monolayer, Few-Layer, and Bulk $ReSe_2$: An Anisotropic Layered Semiconductor. *ACS Nano* **2014,** *8*, 11154-64.

(143) Momma, K.; Izumi, F. VESTA 3 for three-dimensional visualization of crystal, volumetric and morphology data. *J. Appl. Crystallogr.* **2011,** *44*, 1272-6.

(144) Lamfers, H. J.; Meetsma, A.; et al. The crystal structure of some rhenium and technetium dichalcogenides. *J. Alloy. Compd.* **1996,** *241*, 34-9.

(145) Wilderva, J. C.; Jellinek, F. Dichalcogenides of Technetium and Rhenium. *J. Less-Common Met.* **1971,** *24*, 73-81.

(146) Liang, C. H.; Chan, Y. H.; et al. Optical anisotropy of Au-doped ReS_2 crystals. *J. Alloy. Compd.* **2009,** *480*, 94-6.

(147) Chenet, D. A.; Aslan, O. B.; et al. In-Plane Anisotropy in Mono- and Few-Layer ReS_2 Probed by Raman Spectroscopy and Scanning Transmission Electron Microscopy. *Nano Lett.* **2015,** *15*, 5667-72.

(148) Wang, Y. Y.; Gao, R. X.; et al. Thickness identification of two-dimensional materials by optical imaging. *Nanotechnology* **2012,** *23*, 495713.

(149) Ho, C. H.; Huang, Y. S.; et al. In-plane anisotropy of the optical and electrical properties of layered ReS_2 crystals. *J. Phys. Condens. Matter* **1999,** *11*, 5367-75.

(150) Ho, C. H.; Yen, P. C.; et al. Polarized electrolyte-electroreflectance study of ReS_2 and $ReSe_2$ layered semiconductors. *J. Phys. Condens. Matter* **2001,** *13*, 8145-52.

(151) Marzik, J. V.; Kershaw, R.; et al. Photoelectronic Properties of ReS_2 and $ReSe_2$ Single-Crystals. *J. Solid State Chem.* **1984,** *51*, 170-5.

(152) Tonndorf, P.; Schmidt, R.; et al. Photoluminescence emission and Raman response of monolayer MoS_2, $MoSe_2$, and WSe_2. *Opt. Express* **2013,** *21*, 4908-16.

(153) Chernikov, A.; Berkelbach, T. C.; et al. Exciton Binding Energy and Nonhydrogenic Rydberg Series in Monolayer WS_2. *Phys. Rev. Lett.* **2014,** *113*, 076802.

(154) Dumcenco, D. O.; Huang, Y. S.; et al. Optical characterization of niobium-doped rhenium disulphide single crystals. *J. Appl. Phys.* **2007,** *102*, 083523.

(155) van der Zande, A. M.; Huang, P. Y.; et al. Grains and grain boundaries in highly crystalline monolayer molybdenum disulphide. *Nat. Mater.* **2013,** *12*, 554-61.

(156) Huang, J. K.; Pu, J.; et al. Large-Area Synthesis of Highly Crystalline WSe_2 Monolayers and Device Applications. *ACS Nano* **2014,** *8*, 923-30.

(157) Li, Y. L.; Rao, Y.; et al. Probing Symmetry Properties of Few-Layer MoS_2 and h-BN by Optical Second-Harmonic Generation. *Nano Lett.* **2013,** *13*, 3329-33.

(158) Huang, M. Y.; Yan, H. G.; et al. Probing Strain-Induced Electronic Structure Change in Graphene by Raman Spectroscopy. *Nano Lett.* **2010,** *10*, 4074-9.

(159) Wu, J. X.; Mao, N. N.; et al. Identifying the Crystalline Orientation of Black Phosphorus Using Angle-Resolved Polarized Raman Spectroscopy. *Angew. Chem. Int. Edit.* **2015,** *54*, 2366-9.

Appendix A. **Calculations for 2D Optics**

A.1. **Electric Field Enhancement on Interfaces**

Assuming normal incidence, non-absorbing media, and, an interface of air (or another medium) and a semi-infinite substrate, the electric field on the interface, $E_{interface}$, will be

$$E_{interface} = E_{incident} + E_{reflected} \tag{16}$$

Where $E_{incident}$ and $E_{reflected}$ are the incident and reflected electric fields, respectively as depicted in Figure A-1.

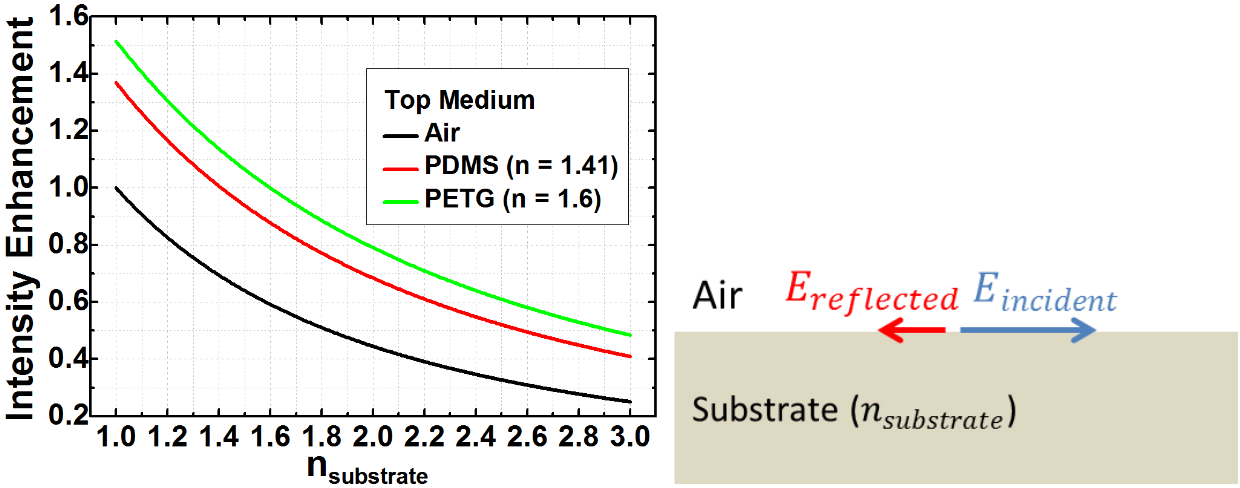

Figure A-1: Intensity enhancement as a function of the refractive index of the substrate at an interface with three top media: Air, PDMS, and PETG (left). A diagram of air and semi-infinite substrate interface (Right).

Then, $E_{interface} = E_{incident}(1 + r)$, where r is the reflection coefficient for the air to substrate interface and is given by $r = \frac{n_{air} - n_{substrate}}{n_{air} + n_{substrate}}$, n_{air} and $n_{substrate}$ being the refractive index of the top and the bottom medium, respectively. Therefore, we obtain the following factors:

$$Enhancement\ factor = \frac{E_{interface}}{E_i} = \frac{2n_{air}}{n_{air} + n_{substrate}}$$

$$Intensity\ enhancement\ factor = \left|\frac{2n_{air}}{n_{air} + n_{substrate}}\right|^2 \tag{17}$$

The same argument applies to the emission process: Imagine an infinitely small light emitter right on the interface. Looking from the top, we will receive some electric field directly from the emitter and some more reflected from the interface. Thus neglecting any effect of the emitter on the reflected field, we obtain the same enhancement for collection from interfaces. Figure A-1 plots the dependence of the intensity enhancement factor on the refractive index of the material as well as a diagram depicting the air-substrate interface. One can calculate the relationship between how much a 2D material absorbs on a substrate and air (free-standing; unsupported). We will not cover the case of multiple substrates such as SiO_2 on Si.

A.2. **Numerical Aperture & Solid Angle relation**

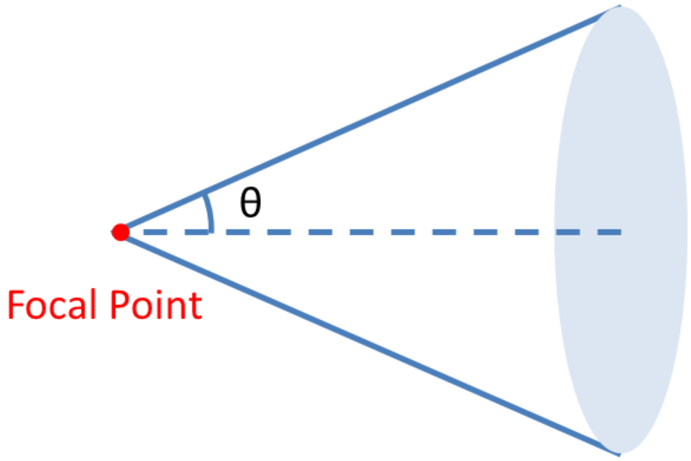

Figure A-2: A diagram of a converging lens.

We can express the solid angle collected by an objective from an object/light source at the focal point in terms of the numerical aperture as follows (assuming immersion in air):

$$Numerical\ Aperture, NA, = \ sin\theta.\ Solid\ Angle, \Omega, = 2\pi(1 - \cos\theta)$$

$$\Omega = 2\pi(1 - \sqrt{1 - NA^2}) \tag{18}$$

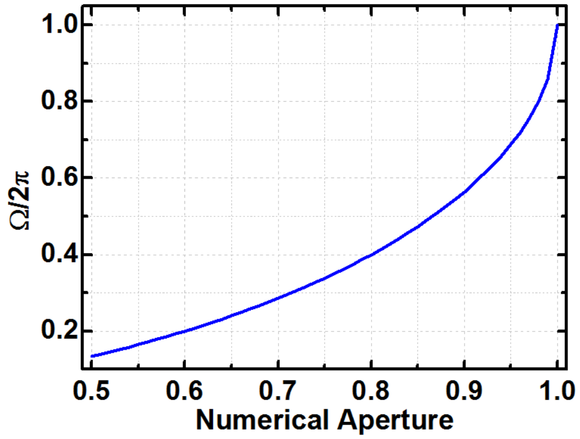

Figure A-3: Solid angle as a function of numerical aperture (as described in the chapter).

The numerical aperture is usually known for an objective, and the solid angle is relevant if one needs to know what fraction of light by an isotropic emitter can be collected.

A.3. Average Power & Fluence: Solving the Pulse Laser Problem

We can calculate the relation between the average power of a pulse laser one measures using a standard power meter and the fluence. First, let us relate the average power to fluence from the definitions of pulse energy and fluence.

$$Pulse\ Energy = Fluence\ \times Spot\ area = \frac{Average\ Power}{Repetition\ Rate} \tag{19}$$

If the average power is not known, it can be calculated as follows:

$$Average\ Power = 1\ \mu W \times \frac{Repetition\ Rate}{1MHz} \times \frac{Fluence}{1\ Joule/_{m^2}} \times \frac{Spot\ area}{1\ \mu m^2} \tag{20}$$

If the fluence is not known, it can be calculated as follows:

$$Fluence = \frac{1\ Joule}{m^2} \times \frac{1MHz}{Repetition\ Rate} \times \frac{Average\ Power}{1\ \mu W} \times \frac{1\ \mu m^2}{Spot\ area} \tag{21}$$

Example: Repetition rate = 80 MHz, spot area = 4 µm, absorption = %5

$$\text{Absorbed}\ Fluence = \frac{1\ Joule}{m^2} \times \frac{1MHz}{80\ MHz} \times \frac{Average\ Power}{1\ \mu W} \times \frac{1\ \mu m^2}{4\ \mu m^2} \times 5\%$$

$$\text{Absorbed}\ Fluence = \frac{1\ Joule}{m^2} \times \frac{Average\ Power}{6.4\ mW}$$

A.4. **Exciton Density Calculations for CW Laser Excitation**

If $n = n(t)$ is the number of excitons created with a CW laser excitation.[1] The rate equation for n (neglecting the higher order terms in n) is as follows:

$$\frac{dn}{dt} = G - \frac{n}{\tau} \tag{22}$$

Where G, the generation term, is the number of photons absorbed per unit area (volume for 3D systems), per unit time. The steady state concentration becomes $n_{ss} = G\tau$. Assuming one exciton is created per absorbed photon (internal quantum efficiency of 1),

$$\begin{aligned} G &= Absorption\ \times \frac{Number\ of\ incident\ photons\ per\ unit\ time}{Beam\ area} \\ &= Absorption \times \frac{Incident\ power}{Beam\ area \times Photon\ energy} \end{aligned} \tag{23}$$

$$Incident\ power = Number\ of\ incident\ photons\ per\ unit\ time \times Photon\ energy \tag{24}$$

We write the generation term as follows for quick calculations:

$$G = Absorption \times \frac{Incident\ power}{\mu W} \frac{\mu m^2}{Beam\ Area} \frac{eV}{Photon\ energy} \times 6.25 \times 10^{20} cm^{-2} \quad (25)$$

Where, $6.25 \times 10^{20} cm^{-2} = \frac{\mu W}{eV \times \mu m^2}$.

Example: $Absorption = 10\%, Power = 10\ \mu W, Area = 1\ \mu m^2, Photon\ energy = 2\ eV, \tau = 4\ ps$.[2] We find that $n_{ss} = 1.25 \times 10^9 cm^{-2}$

A.5. **Applying Strain to TMDCs**

When a flexible substrate is bent in a direction, there will be tensile strain along the same direction (ignoring the general case of strain induced in the other directions). In such a case, the tensile strain, ε, can be calculated as follows:

$$\varepsilon = \frac{\tau}{2R_{curvature}} = \frac{\tau}{D_{curvature}} = 1\% \times \frac{\tau/10\mu m}{D_{curvature}/mm}$$

Where τ is the thickness of the flexible substrate, and $R_{curvature}$ and $D_{curvature}$ are radius and diameter of curvature at the sample location along the strain direction, respectively.

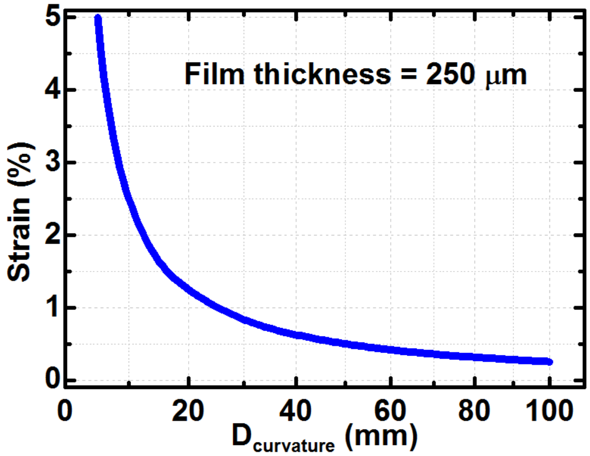

Figure A-4: Strain as a function of diameter of curvature (5 to 100 mm) on a 250 µm film.

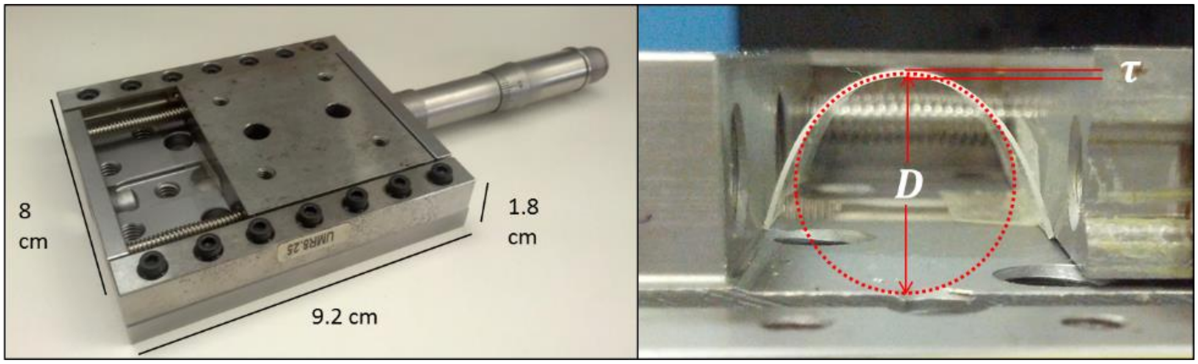

Figure A-5 Strain device and a flexible substrate bent to apply tensile strain to a sample on the top surface (Left and right, respectively).

The samples of interest should be as close to the center of the substrate so that an objective can go sufficiently down to focus on them. We also note that the strain applied to the flexible substrate may not be fully transferred to the flakes on it.[3] Having large flakes may help transfer the strain better.

A.5.1. Applying Large Biaxial Strain

One way of applying large strain to TMDCs is to create a pressure difference across suspended membranes to induce biaxial strains.

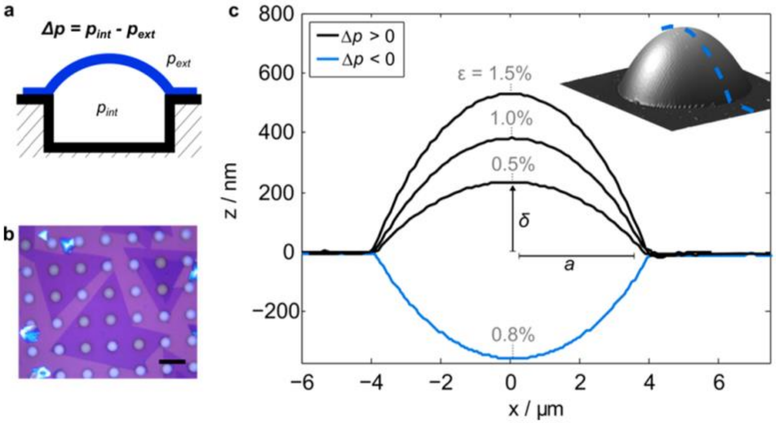

Figure A-6: Applying strain via pressure difference above and below 1L MoS_2 a) Device schematic. (b) A CVD grown sample of MoS_2 membranes suspended over cylindrical cavities (scale bar is 20 µm). (c) An AFM cross-section of a device at various pint, resulting in different biaxial strains at the center of the device.[4]

Appendix B. **Sample Preparation and Optical Alignment Procedure**

B.1. **Making PDMS (Polydimethylsiloxane)**

PDMS substrates used for fabrication and transfer of the materials mentioned in this dissertation have been prepared according to the following recipe:

1. We clean a recyclable plastic or glass cup with IPA and dry it by blowing nitrogen.

Base and curing agent of “Sylgard 184 Silicone Elastomer Kit” have been used. Base to curing agent ratio is 10:1 or 10.5:1 **by volume, not by weight**. Syringes help the accuracy. The stickiness of PDMS increases with the increasing proportion, but it gets less stiff which is harder to handle. Thus if one needs to transfer exfoliated samples from PDMS to other substrates the base: curing agent ratio should not be much higher than 10.5:1.

2. Next, we pour the ingredients with the ratio above into the clean cup.
3. We mix them with a mixer and then pour into a clean petri dish with a very flat base.
4. Place the petri dish in a desiccator to remove the air bubbles that should already be visible in PDMS.
5. Use a leveler or a smartphone with the right application to make sure the petri dish is very flat.

There are advantages of having the PDMS surface super-flat: It is much easier to look for few-layer materials under a microscope and to focus onto a specific flake while transferring.

6. Keep it in a desiccator for 48 hours. There is no need for baking the PDMS.

PDMS surface is sticky thus it is going to catch dust and other kinds of dirt from the air over time. In that case, nitrogen blowing can help. Keep it in a desiccator when not in use. Endgame solution is to use the bottom surface of the PDMS which will stay cleaner than the top surface.

B.2. **How to Exfoliate TMDCs?**

We have videotaped a few demonstrations on how to prepare a Scotch tape and use it to exfoliate, starting from a commercial bulk crystal.[5] There are many other online resources on this; we firmly recommend investing some time in that before attempting exfoliating.

B.2.1. Exfoliating onto PDMS

We use a tape called "blue tape" to exfoliate onto PMDS. A demonstration video is available online.[6] Figure B-1 shows a good blue tape which can give good ultrathin layers. A good blue tape is expected to have shiny, large, unbroken crystals. Normally, since the PDMS has a sticky surface, 1Ls+ can be obtained easily with little pressure. If PDMS is not able to cleave relatively high amount of shiny bulk flakes, some more pressure can be applied.

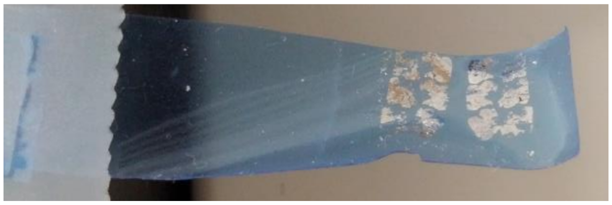

Figure B-1: Blue tape with some amount of TMDC crystal.

Blue tapes from Semiconductor Equipment Corp. with the part number "18133CR-7.50 Blue Low Tack Sq CR" have been used. Blue tape can be supported by Scotch tape as the blue tape is softer and can break the crystals on it.

B.2.2. Exfoliating onto Polycarbonate

Polycarbonate (PC) is a polymer, and we can use it as a flexible substrate for strain-optics experiments. One way of obtaining TMDCs is to transfer from PDMS onto flexible substrates as will be explained in Appendix B.4. Another way is to exfoliate directly onto the substrate. We first clean a piece of PC with ethanol and dry it with nitrogen. We then follow the same exfoliation method described for PDMS. If the blue tape does not give a good yield of ultrathin flakes, one can try Scotch tape (personal communication, Dr. Ali Dadgar and Prof. Abhay Pasupathy, April 21, 2017).

B.3. **Large Monolayers on PETG Substrates**

It is desirable to have large 1L+ crystals on PETG (Polyethylene terephthalate glycol-modified) substrates. Exfoliating large 2L and 3Ls of $MoTe_2$ on PDMS has been more often and easier than 1Ls. Therefore, we have used the gold assisted thermal release tape method to deposit large 1Ls onto PETG substrates directly.[7-8] A standard gold evaporator was employed to deposit 100 nm thick gold on a few blue and Scotch tapes.

Figure B-2: Various tapes of $MoTe_2$ crystals coated with a layer of 100 nm Au.

Such tapes are shown in Figure B-2. The tape on the far right was copied onto a thermal release tape to use on a substrate directly. PETG substrates became very soft and gathered much glue from the thermal release tape. Large 1Ls on PETG have been obtained. Reflection measurements have confirmed the position of the A excitons; however, no PL counts have been detected. We suspect that the softening of PETG (with heating) or the acid treatment caused this since $MoTe_2$ is relatively less stable compared to other group-VI TMDCs.

B.4. Transferring an ultrathin TMDC onto another substrate from PDMS and PPC/PDMS

PDMS loses its stickiness at around 40 °C. One can place the desired substrate on a hot plate. Then the PDMS with flakes can be slowly approached by micromanipulators and even monitored by objectives and cameras. Imaging is especially necessary if one needs to align the flakes on PDMS with others already placed on the target substrate. It is also okay to hold the PDMS by hand and make it touch the new surface. After about 30 seconds, the PDMS can be removed the same way it was made to contact the substrate. The few-layer flakes should have been transferred now.

Another common goal of transfers is to cover the flakes of interest with hBN to protect them. If hBN does not fully cover the flakes, the overlapping part should still be okay.

B.4.1. Hand-Transferring from PDMS onto PETG

We cut a 28 by 28 mm^2 piece of PETG. The PETG should have a protective film; otherwise, it will be full of scratches and dirt such that the surface may not accept the transfer. We clean some of the PETG substrates with acetone, isopropanol, and distilled water before transferring. One can clean multiple times until the PETG looks clean under a microscope.

We exfoliate the desired flake onto PDMS. Then, the standard transfer procedure is performed. Here are some more tips: We mark the locations of the flakes both on the slide and the PDMS with the help of the microscope light as shown in Figure B-3.

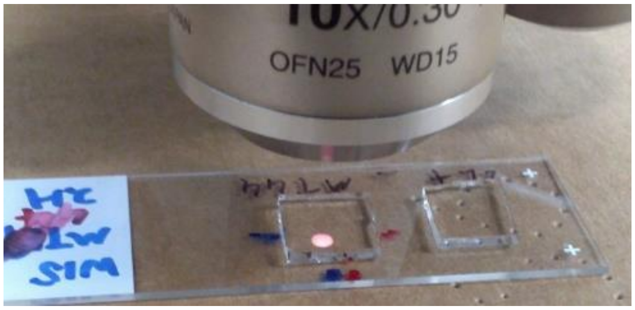

Figure B-3: Marking the slide and PDMS to locate the samples.

Then, we very slowly remove the PDMS by pushing a pair of tweezers between PDMS and the slide starting from the edge further from the flakes, as shown in Figure B-4. It needs to be slow, because any sudden movement may break the 1L+ flakes.

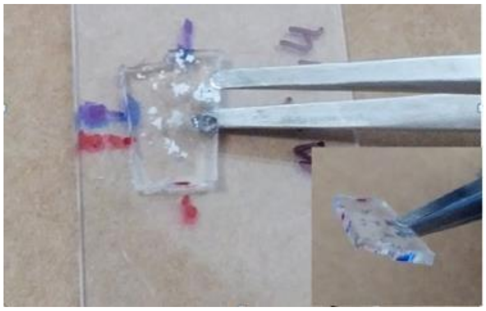

Figure B-4: Gently removing the PDMS from the slide. The bottom-right inset shows the marking on the PDMS after it has been lifted off.

Then we put the pre-cleaned PETG onto a hot plate at 40-45 °C. We slowly place the PDMS onto the PETG substrate by making sure that the markings indicate that the flakes will be in the middle after transferring as shown in Figure B-5. Keep the PETG still using a second pair of tweezers.

Figure B-5: Placing PDMS onto PETG on a hot plate.

We wait for 15-30 seconds. Then slowly remove the PDMS at an angle close to normal (by pulling upwards rather than folding the PDMS on top of itself and pulling backward) as shown in Figure B-6.

Figure B-6: Removing PDMS from PETG at normal incidence.

We have one warning for this method: We have noticed that not all but about a half to a third of the flakes transferred gets strained and the PL peak redshifts by a few meV to ~50 meV. This has been helpful because we can see the huge effect of strain on the spectral width of the 2L flakes. Nevertheless, one has to be very gentle when dealing with TMDCs on PDMS and flexible substrates. Heating and cooling the substrate might also help relax the strain that occurs after hand-transfers.

B.4.2. Transfer stage for transferring from PDMS onto PETG

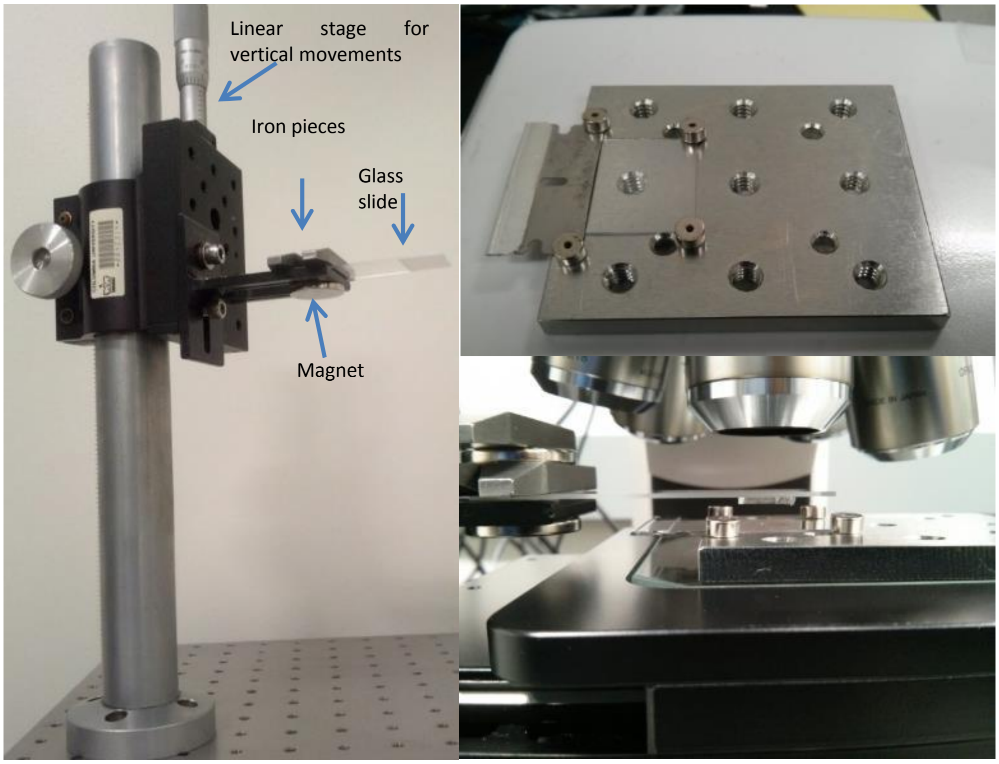

Figure B-7: Equipment used for transfers . Left: Transfer arm to slowly manipulate the contact between PDMS and the target substrate (PETG in this case). Top right: PETG piece fixed on an iron plate with magnets. Bottom right: Glass slide with PDMS faces the PETG substrate under a microscope objective.

As PDMS loses stickiness at an elevated temperature, less PDMS residue is expected to be left on the transferred flakes. Thus, we fix the PETG with magnets onto an iron bar of rectangular prism shape. We focus on the PETG surface close to the mid-point and then lower the stage to open some space to lower the PDMS. Then, we focus on the PDMS surface using the linear stage shown in Figure B-7 and find the flake of interest and lift the PDMS up back. Next, we remove the iron piece and heat it on a hot plate to about 45 °C. We bring the iron back under the microscope, focus back on the PETG and make sure that the local area is clean for the flake to be transferred. Next, we lower the transfer stage and bring the PDMS to focus. Then, we slowly raise the microscope stage, and the PETG will soon be focused as well as the flakes. PDMS should touch the surface, and the boundary between the areas of the PDMS that are in contact and not in contact will appear and propagate through the field of view. If it does not, despite lowering the slide sufficiently, one can use a stick or non-magnetic tweezers to press on the slide. After the boundary passes by the area of inspection, wait for about 30 seconds, and then the stage can be lowered slowly, looking for the boundary to go back. The flake should end up on the PETG surface.

B.4.3. Preparing PPC on PDMS

1. Place a clean PDMS on a clean microscope slide
2. Etch PDMS with oxygen plasma at a power of 50 W for 15 seconds.
3. Spin coat PPC onto PDMS at 2000 rpm, heat it at 80 °C for 5 minutes on a hot plate.
4. Transfer PPC/PDMS onto a clean slide
5. Cut down PDMS to a smaller size
6. Exfoliate some hBN onto SiO_2/Si
7. Pick up that hBN with PPC/PDMS at 40 °C
8. hBN/PPC/PDMS can pick up another few-layer at 40 °C.

B.4.4. Preparing PPC on SiO_2/Si

One can also directly exfoliate onto PPC/SiO2/Si with Scotch tape and then physically remove the PPC and place onto PDMS and transfer the PPC, with the flakes, onto the desired substrate at 80 °C. PPC needs to be cleaned afterward.

1. Place a SiO_2/Si chip on a spin coater, turn in the chuck vacuum to hold the chip.
2. 2 drops of PPC on the chip.
3. 5500 rpm for 60-75 seconds with an acceleration of 4000 rpm/s^2

4. Bake at 80 °C for 3 minutes.
5. Drill a hole on a clean Scotch tape and cover the PPC covered chip with it.
6. Exfoliate your desired material regularly.
7. The Scotch tape can remove the PPC from the chip and can be carried onto PDMS to transfer to the target substrate of choice.

B.4.5. Gently Handling Flexible Substrates

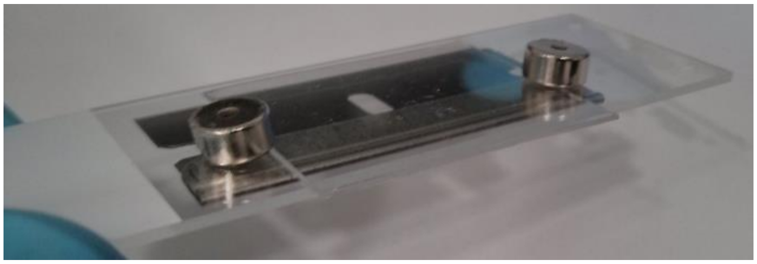

Figure B-8: PETG substrate fixed on a slide with magnets and a thin razor blade.

When a flake is placed on a flexible substrate, it is important to handle it gently (see the discussion towards the end of B.4.1). Our setup includes an inverted microscope, and we need to fix the substrates onto glass slides so that they will not fall. We have realized that if one uses tapes to fix them, then removing them from tapes may introduce strain or cracks on flakes. Therefore, we use the structure shown in Figure B-8. The flexible substrate is placed between a slide and a thin razor. Magnets placed on the other side of the slide fix the razor and the substrate.

B.5. **Optics in the Near-Infrared Spectral Range**

$MoTe_2$ has a band gap around 1 eV. Neither silicon detectors are efficient, nor can we humans see the light, energy of which is in the near-infrared range. Thus, an InGaAs detector is a solution, and some precaution needs to be taken on the excitation and collection path:

- An objective that has good transmission in the IR region and has invariant focus in a broad range is needed. The near infra-red (NIR) light is expected to be focused once the red light (closest color to the infra-red that we humans can see) is focused on the sample.
- A webcam can be used to see further into the NIR for both focusing and aligning. Older phones and webcams might work better as they may not be optimized in order not to capture any light humans cannot see for more realistic photography (above 700 nm).
- We have utilized a few Helium-Neon lasers (HeNe) which had multiple sharp lines around 1.1 eV. We have filtered them with a band pass filter.

B.6. **Aligning an Invisible Laser**

One might need to use a laser that is in the IR, but they will not be able to see it. How can we align it? Safety first: An invisible laser is more dangerous than a visible one, so wear appropriate goggles. The procedure is as follows:

1. Align the optical path using a visible laser and place 2-3 adjustable apertures (irises) on the optical path and make light spots perfectly symmetric around the small apertures.
2. Place a flip mirror in the appropriate position to be able to switch between the two lasers.
3. Two mirrors before the apertures are needed to guide the invisible laser into the optical path so that one does not have to change another mirror which would affect the alignment of the other light sources.

4. Invisible laser beam should be aligned with the centers of the apertures with the help of an alignment card or a camera. A power meter can also be used by maximizing the transmitted laser power after the apertures.
5. A camera (if it can see the laser wavelength) can be used to make sure the invisible light spot is at the desired point on the sample. Avoid looking at the (invisible) reflected laser by the sample.

B.7. **Obtaining Circularly Polarized Laser Light**

One can follow these steps to obtain circularly polarized light:

1. Linearly polarize the laser. Use a neutral charge density filter to adjust the laser power (not a second linear polarizer otherwise circular polarization will be lost).
2. A half-wave and a quarter-wave plate are needed because the optics (between the quarter wave plate and the sample) will introduce elliptical polarization.
3. Check that the power changes less than 10% (or less if needed) under the objective when a linear polarizer (right before or right after a non-birefringent objective) is rotated. Recursively minimize this power change using the wave plates.
4. With a Fresnel rhomb or a second quarter wave plate, check that the light reflected by the sample is also circularly polarized if needed.

Appendix C. **Tools and Software**

C.1. **Thin Film Optics Calculations**

If the research requires thin film optics calculations, there is a Python code by Steve Byrnes.[9] He also mentions other people's work that could be of interest.

C.2. **Useful Online Tools**

For an optics researcher, there are handy tools that save time such as a unit converter for energies.[10]

C.3. **Drawing the Crystal Structures of TMDCs**

We have used VESTA, which is free software, for some of the studies included (e.g., see Figure 1-2 and Figure 1-6).[11] Specific crystal structure data are available online.

C.4. **Handling Photos of Ultrathin TMDCs**

ImageJ is very useful and easy-to-use software for handling the photos of TMDCs. One can calculate the contrast (in a color channel of RGB) of flakes and estimate their thicknesses easily. One can calibrate a microscope (parameters such as exposure time and light intensity) on a sample with the flakes of known thicknesses on a specific substrate. Then, ImageJ can be used to compare the contrast of other flakes to the known ones. There are many other features one can explore too.

C.5. Extracting Data from Figures

Some academic publishers started requiring a "data availability statement" from the authors for publications. However, it is still not uncommon that there is data one would like to use for calculations, but it is only an image that exists rather than the proper data file. It could be a figure in a published paper or an efficiency curve in a datasheet. No worries, there are online tools available for this purpose.[12]

References for Appendices

(1) Pelant, I.; Valenta, J., Kinetic Description of Luminescence Processes. In *Luminescence Spectroscopy of Semiconductors*, Oxford University Press: 2012.

(2) Shi, H. Y.; Yan, R. S.; et al. Exciton Dynamics in Suspended Monolayer and Few-Layer MoS_2 2D Crystals. *ACS Nano* **2013,** *7*, 1072-80.

(3) Jiang, T.; Huang, R.; Zhu, Y. Interfacial Sliding and Buckling of Monolayer Graphene on a Stretchable Substrate. *Adv. Funct. Mater.* **2014,** *24*, 396-402.

(4) Lloyd, D.; Liu, X. H.; et al. Band Gap Engineering with Ultralarge Biaxial Strains in Suspended Monolayer MoS_2. *Nano Lett.* **2016,** *16*, 5836-41.

(5) How to Exfoliate Transition Metal Dichalcogenides. *https://youtu.be/RvNzphyOCWU* **2016**.

(6) How to Exfoliate Transition Metal Dichalcogenides onto PDMS. *https://youtu.be/0KzdU-yeQxk* **2016**.

(7) Desai, S. B.; Madhvapathy, S. R.; et al. Gold-Mediated Exfoliation of Ultralarge Optoelectronically-Perfect Monolayers. *Adv. Mater.* **2016,** *28*, 4053-8.

(8) Magda, G. Z.; Peto, J.; et al. Exfoliation of large-area transition metal chalcogenide single layers. *Sci. Rep.* **2015,** *5*.

(9) Byrnes, S. J. Multilayer optical calculations. *arXiv preprint arXiv:1603.02720v2* **2016**.

(10) Byrnes, S. Photon Conversion Calculator. *http://sjbyrnes.com/convert.html* **2016**.

(11) Momma, K.; Izumi, F. VESTA 3 for three-dimensional visualization of crystal, volumetric and morphology data. *J. Appl. Crystallogr.* **2011,** *44*, 1272-6.

(12) Rohatgi, A. WebPlotDigitizer. *http://arohatgi.info/WebPlotDigitizer/app/* **2015**.